Synthesis and characterization of $Li_2O/K_2O/CuS$ modified sodium-phosphate glasses

A

Thesis

Submitted in partial fulfilment of the

requirements for the award of degree of

DOCTOR OF PHILOSOPHY

By

Paramjyot Kumar Jha
(Regn. No.: 901112001)

Under the Guidance of

Dr. Kulvir Singh
(Professor)

Dr. O. P. Pandey
(Senior Professor)

School of Physics and Materials Science
Thapar University, Patiala-147004

(October-2016)

Dedicated To My

Loving Family

Declaration

I hereby certify that the work which is presented in thesis entitled "**Synthesis and characterization of $Li_2O/K_2O/CuS$ modified sodium-phosphate glasses**" in the partial fulfillment of the requirement for award of the degree of DOCTOR OF PHILOSOPHY in the School of Physics and Materials Science, Thapar University, Patiala is an authentic record of my own work carried out under the supervision of Dr. Kulvir Singh and Dr. O. P. Pandey. The matter embodied in this report has not been submitted in part or full to any other university or institute for the award of any degree.

Paramjyot Jha

(Paramjyot Kumar Jha)

This is to certify that the above statement made by the candidate is correct and true to the best of my knowledge.

Dr. Kulvir Singh

Professor and Associate Dean (Strategy)

School of Physics and Materials Science

Thapar University, Patiala-147004

Dr. O. P. Pandey

Senior Professor and Dean (R & SP)

School of Physics and Materials Science

Thapar University, Patiala-147004

Acknowledgements

This thesis has been kept on track and been seen through to completion with the support and encouragement of numerous people including my supervisors, colleagues, friends and various institutions. No matter how much enterprising and entrepreneurial one's thinking is, yet nobody can do everything without some help and guidance. It is inhumane if the concerned person's assistance goes without appreciation and thanks.

My first and foremost offering of thanks goes to the architects who shaped my dreams into reality, my guides, my both Guru Ji; **Dr. Kulvir Singh** and **Dr. O. P. Pandey** for their excellent guidance, constant encouragement, valuable suggestions, powerful blessings, extreme care and providing me with an excellent atmosphere for doing research and preparation of the thesis. I can see the good shape of my thesis because of their help and suggestions in formatting the entire thesis. Their faith in me has always made me more confident. Apart from the thesis, they improved my personality, communication skills and made me able to survive in any system. They always treated me like a son and took care in every good and bad activity. In my whole journey of Ph.D tenure, they always provided me financial assistance through either projects or teaching assistantship.

It is my privilege to thank **Prof. Prakash Gopalan,** Director, Thapar University, Patiala for providing me resources in the university and needful help during the various stages of my work.

I would like to express my whole-hearted thanks to the members of doctoral committee: **Dr. Susheel Mittal, Dr. B.N. Chudasama and Dr. S.D. Tiwari** for their constant encouragement, insightful comments and fruitful criticism during my progress report presentation. I am thankful to **Dr. Manoj Sharma,** Head, School of Physics and Materials Science for providing all kind of help and support whenever required. My special thanks to the SPMS faculty members (**Dr. K. K. Raina, Dr. N.K. Verma, Dr. Puneet Sharma, Ms. Loveleen Kaur Brar, Dr. B.C. Mohanty, Dr. Soumendu Jana and Dr. D.P. Singh**) who always provided me healthy environment and boosted my energy levels. I would like to thank **Mr. Indermani Mishra**, **Mr. Purshottam Singh**, **Mr. Jant Singh**, **Mr. Lal Ji** and **Mr. Pardeep Singla** for their kind help all-time and made this thesis possible and wonderful experience for me.

My sincere, warm, heartfelt and respectful thanks to **Dr. Gurbinder Kaur** (Research Scientist), SPMS, Thapar University, Patiala for providing me moral support and out of sight help. She always took care of my every small need and provided me more than I expected. She is great, kind and very supportive and I will be always willing to ask for her expertise in research in my whole life.

I am thankful to **Dr. Vishal Kumar and Dr. Akshay Kumar** (Assistant professor) SGGSWU, Fatehgarh Sahib for boosting me up all-time and encouraging me to finish the thesis work. I pay my special thanks to **Dr. Vishal Kumar** as my senior who always has faith in me and guided me well in my down time. He is very kind and generous person whenever I met with him I always gained so much positive energy.

My sincere and respectful thanks to **Dr. Jasmeet Garewal** who helped me in my beginning stage of research during M.Tech. project and made me capable to move forward in the research area.

I am highly obliged to **Mr. Sumit Bhardwaj (**Research Scholar, NIT Hamirpur) and **Mr. Samir Kumar** (Research Scholar, IIT Delhi) who always stood with me and provided me all kind of help in characterization even in crucial time. I am especially thankful to Sophisticated Analytical Instrument Laboratories (SAI Labs) senior operator **(Mr. Mukesh Agrawal and Mr. Ghanshyam Morya)** and clerical assistant **Ms. Heera** for helping me in performing characterizations (XRD and SEM). This thesis would not successfully complete, without the financial assistance provided by **DST, New Delhi** under sanction nos. (SR/S2/CMP-0010/2009 and SB/S2/CMP-080/2013). I am highly thankful to **all the research scholars** from School of Chemistry and Bio-chemistry and Bio-technology department for providing me all kind of help during the entire tenure.

In my daily work, I have been blessed with a friendly and cheerful group of fellow friends. Words are inadequate in expressing my sincere and whole-hearted thanks to my loving and caring friends **Mr. Gourav Singla, Ms. Mani Mahajan and Mr. Suresh Kumar.** They always stood by me during good or bad times. I enjoyed their company alot in my last five years and I thank almighty for blessing me with friends like them. It's my pleasure and privilege to extend my heartfelt thanks to all my seniors **Dr. Kamalpreet Kaur, Dr. Kapil Sood, Dr. Bhupinder Kaur** and **Dr. Ranvir Singh** for giving me valuable suggestions and encouragement. I am also thankful to all my loving friends **Dr. Mintu Tyagi , Dr. Samita Thakur, Dr. Chandni, Mr. S.K. Arya, Mr. Gaurav Sharma, Mr. Satwinder Singh, Ms. Pooja Singla, Mr. Parveen Jha,** and **Mr. Devender Kumar** for providing fun filled environment which enabled me to bypass the more persistent obstacles to thesis completion. I am thankful to all my loving and caring juniors **Aayush Gupta, Savidh Khan, Rameez Ahmad Mir** and **Piyush Sharma** for providing me fun filled and cheerful environment.

I am thankful to all faculties, staff members and research scholars of SPMS who never turned me down whenever I approached for any help.

I would like to special thanks **Ms. Megan Mahan Bricker** (Programming director), American Ceramics Society for providing me wonderful platform for the future. She always showed faith in me and increased my confidence level.

In above all, behind my success, it will be insufficient if I would not thank my first guru, friend, my big brother **Mr. Nand Kishor Jha** who showed me right path and always encouraged me for the higher study. He took care of my small needs like a father. My affectionate thanks to my mother **(Ms. Neelam Devi)** and Father **(Shri Niranjan Jha)** for their moral support and blessings throughout the life. In addition, I would like to thank and extend my deep gratitude to my loving and caring elder brother **(Mr. Braj Mohan Jha),** Sister in laws **(Ms. Nikki Jha and Ms. Pooja Jha)** for their constant encouragement, care and creation of a pleasant atmosphere for me.

Above all, I owe it all to Almighty God for granting me the wisdom, health and strength to undertake this research work and enabling me for its completion.

(Paramjyot Kumar Jha)

Index

Contents *Page No.*

List of figures

Contents *Page No.*

List of tables

Contents Page No.

List of Publications

1. **Paramjyot Kumar Jha**, O.P. Pandey, K. Singh, "Na_2S-P_2S_5 based super-ionic glasses for solid electrolytes" ***Trans. Indian Ceram. Soc.,*** 72 (1) (2013) 5-9.

2. **Paramjyot Kumar Jha**, O.P. Pandey, K. Singh, "Structural and thermal properties of Na_2S–P_2S_5 glass and glass ceramics" ***J. Non. Cryst. Solids***, 379 (2013) 89-94.

3. **Paramjyot Kumar Jha**, O.P. Pandey, K. Singh, Crystallization and glass transition kinetics of Na_2S-P_2S_5 based super-ionic glasses, ***Part. Sci. Tech.,*** 33 (2015)166-171.

4. **Paramjyot Kumar Jha**, O.P. Pandey, K. Singh, FT-IR spectral analysis and mechanical properties of sodium phosphate glass-ceramics, ***J. Mol. Struct.,*** 1083 (2015) 278-285.

5. **Paramjyot Kumar Jha**, O.P. Pandey, K. Singh, Structural and non-isothermal study of Li_2O modified sodium-phosphate glasses, ***J. Mol. Struct.,*** 1094 (2015) 174–182.

6. **Paramjyot Kumar Jha**, O.P. Pandey, K. Singh, Non-isothermal crystallization kinetics of K_2O modified sodium-phosphate glasses, ***J. Non-Cryst. Solids,*** 440 (2016) 76–84.

7. **Paramjyot Kumar Jha**, O.P. Pandey, K. Singh, Synthesis and characterization of CuS modified Na_2S-P_2S_5 glasses ***(Under preparation).***

8. **Paramjyot Kumar Jha**, O.P. Pandey, K. Singh, Optimization of high conducting $Na_3Zr_2Si_2PO_{12}$ phase by new phosphate salt for solid electrolyte, ***Silicon***, DOI 10.1007/s12633-015-9396-2 (2016) ***(Not the part of thesis work).***

9. **Paramjyot Kumar Jha,** Jasmeet Kaur Gill, Gourav Singla, K. Singh, O.P. Pandey, Structural, thermal, and electrical properties of $(100-x)ZrO_2(x)Bi_2O_3$ compound, ***Ionics***, 18 (2012) 759-767. ***(Not the part of thesis work)***.

10. Gourav Singla, **Paramjyot Kumar Jha,** Jasmeet Kaur Gill, K. Singh, Structural, thermal and electrical properties of Ti^{4+} substituted Bi_2O_3 solid system, ***Ceramics International,*** 38 (2012) 2065–2070. ***(Not the part of thesis work).***

National/International conferences attended

1. National Conference on Nanomaterials synthesis and applications, ***D.A.V College, Jalandhar***, *February 6-7, 2009* ***(Attended).***
2. **Paramjyot Kumar Jha,** K. Singh, O.P. Pandey, Study of solid solution limit in the ZrO_2-Bi_2O_3 system for achieving higher ionic conductivity, 22^{nd} Annual General Meeting of MRSI, ***Bhopal,*** *February 14-16, (2011)* ***(Poster presentation).***
3. **Paramjyot Kumar Jha,** K. Singh, O.P. Pandey, Influence of structural and electrical properties of NAISCON from new compounds, **International conference** on energy efficient materials: Manufacturing methods and Machineries for ceramic industries *[IC2E4MCI-11], Auditorium,* ***Shilpgram, Agra,*** *December 19-22, (2011)* **(*Poster presentation).***
4. **Paramjyot Kumar Jha,** O.P. Pandey, K. Singh, Structural variation in NAISCON from monoclinic to rhomohedral with non-stoichiometric composition, **National conference** on recent trends in Materials Science and Research *(RTMSR-2012),* ***NIT Srinagar, Srinagar,*** *September 3-5, (2012)* ***(Oral presentation).***
5. **Paramjyot Kumar Jha,** O.P. Pandey, K. Singh, Na_2S-P_2S_5 super ionic glasses for solid electrolytes, **National Symposium** on "Materials and Processing-2012 (MAP-2012), Functional Glass/Glass Ceramics, Advanced Ceramics and High Temperature Materials", ***BARC, Mumbai,*** *October 10-12, (2012)* ***(Poster presentation).***
6. **Paramjyot Kumar Jha,** O.P. Pandey, K. Singh, Dielectric spectroscopy studies of NASICON materials, **International conference** on recent trends in applied Physics and Materials Science (RAM-2013), ***Govt. College of engineering and technology, Bikaner,*** *February 1-2, (2013)* ***(Poster presentation).***
7. **Paramjyot Kumar Jha,** O.P. Pandey, K. Singh, Na_2S-P_2S5 glass-ceramic electrolytes for sodium batteries at room temperature, **4^{th} International Conference** on Advances in Energy Research (ICAER-2013), ***Indian Institute of Technology Bombay,*** *December 10-12, (2013)* ***(Oral presentation).***
8. **Paramjyot Kumar Jha,** O.P. Pandey, K. Singh, Structural and thermal studies of Na_2S-P_2S_5 based glass ceramics as solid electrolytes, **National Conference** on Innovative molecules for sustainable future, (NCIMSF-2013), ***Thapar University, Patiala,*** *October 24-26, (2013)* ***(Poster presentation).***

9. **Paramjyot Kumar Jha,** O.P. Pandey, K. Singh, FTIR spectroscopic study of Na_2S-P_2S_5 glass-ceramics for Na-ion batteries, First **International Conference** on Emerging Trends in Engineering & Applied Sciences (ICETEAS-13), ***Rajasthan college of Engineering for women, Jaipur,*** *December 27-28, 2013* ***(Oral presentation).***
10. **Paramjyot Kumar Jha,** O.P. Pandey, K. Singh, Crystallization and glass transition kinetics of Na_2S-P_2S_5 based super-ionic glasses, **International Conference** & Exhibition of Powder, Granule and Bulk Solids: Innovations and Applications, ***Thapar University, Patiala,*** *November 28-30, (2013)* ***(Poster presentation).***
11. **Paramjyot Kumar Jha,** O.P. Pandey, K. Singh, Na_2S-P_2S_5 based solid electrolytes for sodium-ion batteries at room temperature as a renewable source, **International conference** on Materials challenges in alternative & renewable energy (MCARE-2014) Hilton Clearwater Beach Resort, ***Clearwater, Florida, USA,*** *February 16-20, 2014* ***(Oral presentation).***
12. **Paramjyot Kumar Jha,** O.P. Pandey, K. Singh, Crystallization kinetics and mechanical properties of Na_2S-P_2S_5 based glasses/glass-ceramics solid electrolytes for sodium-ion batteries, Electronic Materials and Applications 2015 (EMA-2015), Double Tree by Hilton Orlando at Sea World***, Orlando, Florida, USA,*** *January 21-23, 2015* **(*Oral presentation).***
13. **Paramjyot Kumar Jha,** Ceramics Expo-2015 "*Workshop* on manufacturing tradeshow for ceramic/glass materials and technologies; organized my American Ceramics Society, ***Cleveland, Ohio, USA,*** April 26-30, 2015. ***(Attended).***
14. **Paramjyot Kumar Jha,** O.P. Pandey, K. Singh, Synthesis and characterization of Li_2O and K_2O modified sodium-phosphate glasses, Materials Science and Technology (MST-2015), Greater Convention Center, ***Columbus, Ohio USA,*** *October 4-9, 2015* ***(Oral Presentation).***
15. **Paramjyot Kumar Jha,** "76^{th} conference on glass problem" which includes short courses on glasses/glass-ceramics and glass Industries exposures, Greater Convention Center, ***Columbus, Ohio USA,*** *November 2-5, 2015* ***(Attended).***
16. **Paramjyot Kumar Jha,** O.P. Pandey, K. Singh, Structure and crystallization kinetics of fast ion-conducting glasses as solid electrolyte, Electroceramics XV, ***Limoges, France,*** *June 27-29, 2016* ***(Oral Presentation).***

ABSTRACT

Lots of research has been carried out to develop oxide/sulfide glasses as solid electrolytes for batteries applications. The ionic conductivity of the glasses is generally higher than that of the corresponding crystalline counter part because of their open structure. Sulfide based glasses show an increase in ionic conductivity more than three orders of magnitude as compared to the oxide glasses of the similar composition. However, sulfide based glasses are hygroscopic in nature. So, reaction with environmental moisture leads to generation of H_2S gas. Addition of oxides in the sulfide glasses can increase their chemical stability dramatically with marginal decrease in ionic conductivity. Mixed anions effect in either oxide or in sulfide based glasses, enhances the ionic conductivity and thermal stability simultaneously.

Based on the literature review, different series of glasses were synthesized and studied in detail. Moreover, for binary sodium-phosphate glass-ceramics, mechanical properties and their relationship with structural changes are discussed. The effect of modifiers (Li_2O/K_2O/CuS) on thermal stability and on crystallization kinetics in the sodium-phosphate glasses is also presented in this thesis. The entire work of the thesis is presented in **five chapters** as follows:

First chapter deals with the general introduction of the glasses and their synthesis by different routes. Different theories for glass formation and different class of fast ion-conducting glasses as solid electrolytes for batteries applications are also described. Mixed anions effect on stability and on overall conductivity is discussed in detail.

Second chapter is related to the literature review of sulfide and oxide glasses, their synthesis and properties. Synthesis and characterization of oxy-sulfide based glasses for better stability in air are discussed. Mixed modifiers effect on thermal stability and crystallization are also described in this chapter.

Increase in ionic conductivity because of sulfur ion is also discussed in this chapter. Based on some gaps in the study, the aims and objectives of the present research work have been planned.

Third chapter describes about the experimental procedure in the present work. Detailed procedure of synthesis of glasses/glass-ceramics and their characterizations is given in this chapter. Different characterization techniques such as X-ray diffraction (XRD), Differential thermal analyzer (DTA), Fourier transform infrared spectroscopy (FTIR), Raman spectroscopy, Dilatometric measurements, Scanning electron microscopy (SEM), Vickers micro-hardness and Impedance spectroscopy are also discussed.

Fourth chapter deals with the results and discussion part of the present work. This chapter is divided into five sections; the results of oxysulfide glasses are discussed in the first section. The H_2S generation and stability of $Na_2S–P_2S_5$ glasses after exposure to air at different time intervals are investigated. With the help of Raman spectroscopy and FTIR, structural changes in glasses are discussed detail. Two stable samples of the compositions $45Na_2S–55P_2S_5$ and $55Na_2S–45P_2S_5$ (mol %) are selected for further study. Crystallization kinetics of these glasses and their ionic conductivity to check their applicability for solid electrolyte are described in detail in this section.

Second section describes the effect of CuS on $55Na_2S–45P_2S_5$, particularly when exposed to air. Best composition $55Na_2S–45P_2S_5$ was selected from above study for further investigation. The addition of CuS increases the overall conductivity of the system and durability of glasses. CuS is varied from 5 to 10 mol% on the expense of Na_2S and investigated their structural, thermal and electrical properties.

The effect of Na_2O on structural and mechanical properties in the Na_2O-P_2O_5 glass-ceramic system is given in the third section. In the present study, longitudinal and shear velocities of the

prepared glass–ceramics are investigated using ultrasonic echo pulse system. These parameters are used to calculate the mechanical properties of the glass–ceramics. The structural changes in glass–ceramics have been observed with the help of FTIR spectroscopy. The obtained mechanical properties and their relationship with structural changes are also discussed in this section.

In the fourth section, the effect of mixed modifiers on crystallization and thermal stability has been described. Based on the results, the most stable glass having 15 mol% Li_2O has been selected for further study.

In the last section, effect on crystallization and thermal stability of the composition $55P_2O_5$-(45-x)Na_2O-xK_2O; ($5 \leq x \leq 25$) has been given. Stable samples having 10 and 20 mol% K_2O samples were selected for further conductivity study to check their suitability as solid electrolyte.

The conclusion and future scope of the present work is given in the fifth chapter. The present work shows that the sodium-phosphate glasses of compositions $45Na_2S$–$55P_2S_5$ and $55Na_2S$–$45P_2S_5$ are more stable in air. Addition of CuS in the $55Na_2S$–$45P_2S_5$ compositions increases the thermal stability and overall conductivity of the glasses, which may also be used as cathode materials in battery applications. The maximum hardness is observed for 55 mol% Na_2O glass–ceramic sample. The SEM study revealed that interlocked crystals dispersed in a glassy matrix and increases the density. In mixed modifier glasses, 15 mol % Li_2O, 10 and 20 mol % K_2O glasses shows higher thermodynamic and kinetic stability. These glasses can be used as solid electrolyte for battery application.

Chapter-1
(Introduction)

- **Introduction to glasses**
- **Different theories for glass formation**
- **Classification of fast ion-conducting glasses**

1.1. GLASSES

Glasses are structurally disordered and unstable solids that exhibit glass transition before crystallization **[1]**. Generally, glass shows properties of liquid above the glass transition temperature (T_g) and maintain liquid structure in rigid form below T_g. With the help of enthalpy *versus* temperature diagram (Fig.1.1), the formation of crystal, liquid and glass can be understood. It indicates that slow cooling of crystalline material leads to the formation of small nuclei and finally bulk crystallization as shown by abcd path in Fig. 1.1. On the other hand, for other categories of substances exposed to slow/fast cooling, nucleation is avoided and the melt acquires supercooled state, ultimately leading to rigid structure through abegf and abef path as shown in Fig. 1.1.

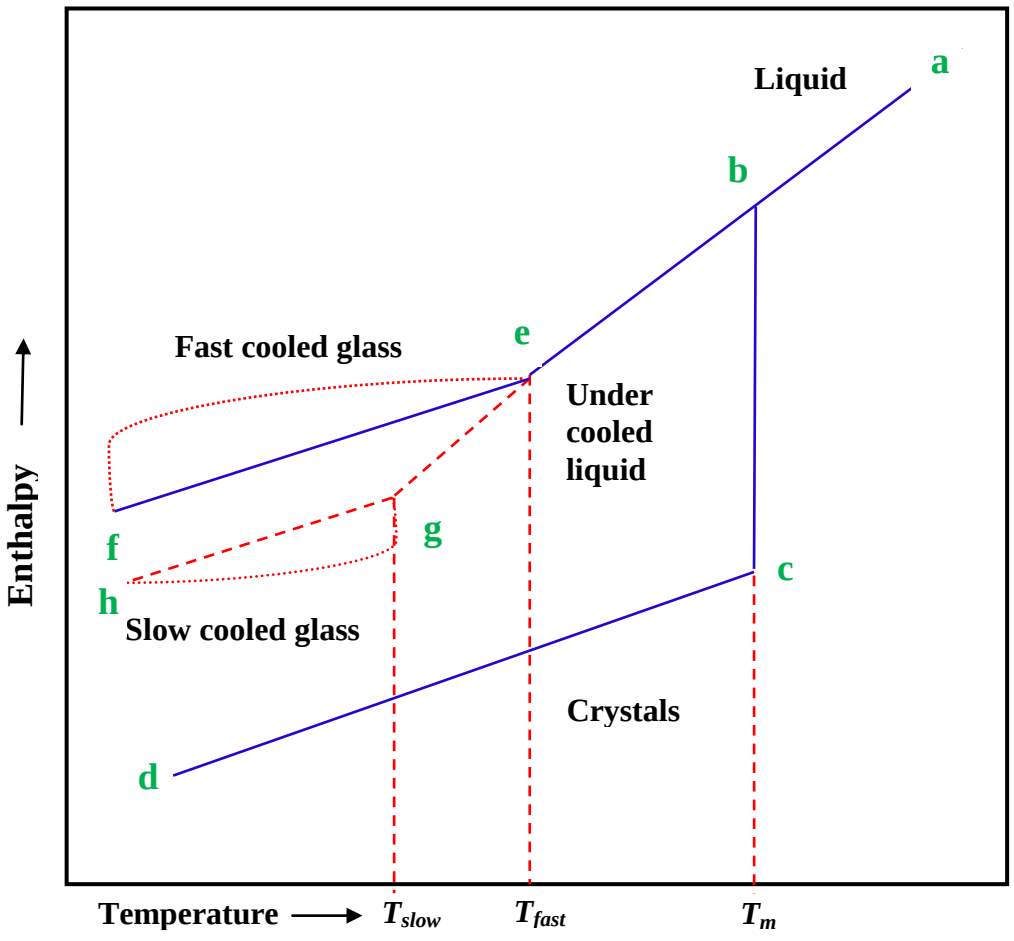

Fig. 1.1: Enthalpy *versus* temperature schematic diagram for liquid, glass and crystal **[2].**

1.2. GLASS COMPONENTS

Normally, glasses are either synthesized from high purity (≥ 99.99 %) chemicals or from a mixture of nearby pure minerals or agriculture waste **[3].** In any case, the role of different components to synthesize the glass is very important. The batch of materials can be divided into five categories **[2, 4-5].** The role of different components are listed in table 1.1 and explained as follows:

1.2.1. Glass formers

The substances which form glass network is normally called "Glass-network formers" or "Glass formers". In this case, cations form oxygen polyhedral triangles and tetrahedral structure. The oxides P_2O_5, SiO_2, B_2O_3, GeO_2 and sulfides P_2S_5, GeS_2, SiS_2 B_2S_3 are glass formers. Glass former oxides or sulfides are used to form glasses. The glass formers have bond strength in the range (60-80 kcal/mol), high field strength (1-2) and low co-ordination number (3<CN<4).

1.2.2. Glass Modifiers

Some oxides and sulfides such as Li_2O, Na_2O, Bi_2O_3, K_2O, Al_2O_3, PbO, V_2O_5, TeO_2, WO_3, MoO_3, and Li_2S, Na_2S, K_2S, La_2S_3 etc., do not form glasses by themselves. However, their ions occupy random places in the glass network and change or modify the structure of glass network by creating additional oxygen ions. These sulfides and oxides are responsible to disrupt the glass forming network which creates non-bridging oxygens (NBOs) and non-bridging sulfurs (NBSs) and consecutively increase the glass forming region. The NBOs and NBSs do not link with polyhedral units. These oxides and sulfides are called "Glass-network modifiers" or "Glass-modifiers". Glass modifier forms glasses when combine with appropriate amount of glass formers. The glass modifier usually have bond strength in the range (10-40 kcal/mol), low field strength (0.35) and (6<CN<8).

Table 1.1: Some glass formers, intermediates and network-modifiers with their properties **[2].**

Role of oxide	Valence electrons	M in MOx	Co-ordination number	Dissociation energy E_d per MOx (kcal)	Single bond strength (kcal/mol)
Glass former	3	B	3	356	119
	4	Ge	4	431	108
	5	P	4	442	111-88
	3	Al	4	402-317	101-79
	4	Zr	6	485	81
	5	Sb	4	339	85-68
	5	As	4	349	87-70
	5	V	4	449	112-90
	4	Si	4	424	106
Intermediate	2	Cd	2	119	60
	2	Be	4	250	63
	4	Zr	8	485	61
	3	Al	6	317-402	53-67
	4	Th	8	516	64
	4	Ti	6	435	73
	2	Pb	2	145	73
	2	Zn	2	144	72
Modifier	1	Cs	12	114	10
	1	Rb	10	115	12
	2	Hg	6	68	11
	1	K	9	15	13
	2	Cd	4	119	30
	1	Na	6	120	20
	2	Ca	8	257	32
	2	Sr	8	256	32
	2	Zn	4	144	36
	2	Ba	8	260	33
	2	Mg	6	222	37
	2	Pb	6	232	39
	1	Li	4	144	36
	4	Th	12	516	43
	3	In	6	259	43
	4	Sn	6	278	46
	3	Ga	6	267	45
	3	Y	8	399	50
	3	La	7	406	58

1.2.3. Glass Intermediates

Some oxides or sulfides can either work as network modifier or network former, which generally depends upon their chemical properties. Hence glass intermediates are also called as conditional glass formers or conditional glass modifiers. The field strength of these glass intermediates usually lies in the range (0.84-1.04), (4<CN<8) and bond strength in between (50-60 kcal/mol).

1.2.4. Colorants

In order to control the color of glasses, certain colorants are used. Generally, colorants are oxides of either of *4f* rare earths or the *3d* transition metals **[5].** Silver and gold are used to add color in the glasses by the formation of colloids. Manganese, iron and copper ions are also used to produce the color in glasses. Colorants are used in the small quantities.

1.2.5. Fining agents

While preparing the glasses, fining agents are used in the final batches. These fining agents remove bubbles from the melt. Potassium, antimony oxides, arsenic, sodium chloride, sodium nitrates, fluorides such as NaF, CaF_2, Na_3AlF_6 and different kind of sulfates are used as fining agents. These materials are generally used in very small amount (< 1 *wt*%).

1.3. DIFFERENT THEORIES FOR GLASS FORMATION

For glass formation, the first model (microcrystal approach) was proposed for silicate crystals. This model suggested that glasses are basically masses of very tiny microcrystals. These microcrystals can be used to explain the disordered structure by X-ray diffraction method. Lebedev and some other researchers proposed a crystallite model, which is different than the first model. According to them, microcrytsals are different (not very small) and have deformed structure. They proposed that in the glass, crystallites are connected with

amorphous regions. Some of the structural models, which explain the formation of glasses, are as follows **[3-5].**

1.3.1. Goldschmidt's theory (1926)

Goldschmidt have given a very simple theory for the glass formation. He proposed a formula in the form of R_mO_n when the ratio of cation radius (R) to anion radius (O) is in between 0.2 to 0.4. This range has a tendency to produce cations connected by four oxygen atoms in the form of tetrahedra. Goldschmidt assumed that during cooling of molten mass only tetrahedrally connected cations can form glasses. This statement was purely empirical. The reason for tetrahedrally connected cations which can only form glasses is not given. Later on, this phenomenon was explained by Zachariasen theory, which is explained in the next section.

1.3.2. Zachariasen theory (1932)

The most common model used for glass formation is based on Zachariasen rule. The rules for crystal chemistry and patterns for glasses are also recognized by Zachariasen. Glasses exhibit amorphous structure/high structural energies. Zachariasen gave some rules for the glass formation which is as follows:

(a) Oxygen atom can be linked with maximum two cations.

(b) The co-ordination number of cation should be small: 3 or 4.

(c) Polyhedral oxygen should share corners, not faces or edges.

(d) In the case of 3D networks, sharing of at least 3 corners is essential.

Commonly, for glass formation above all four rules should be satisfied. Corner-sharing rules with low coordination numbers indicate that glasses will have low density, open and polyhedral structures.

1.3.3. Dietzel theory (1942)

After Zachariasen, lots of researchers used the theory of crystal chemistry to describe the role of oxides for the glass formation. In 1942, Dietzel proposed a theory for estimation of cation-anion bond strength. According to the field strength, cations in oxide substances can be classified.

Dietzel used a coulombic interaction which is given below:

$$\text{Attractive force} = \frac{(Z_c e)(Z_a e)}{(r_c + r_a)^2} \qquad (1.1)$$

where Z_c and Z_a are the valency of cation and anion respectively. r_c and r_a are the atomic radius of cation and anion respectively. After keeping $a = (r_c + r_a)$ and $Z_a = -2$ (for oxides) in equation (1), Dietzel proposed a modified equation in the form of cations as follows:

$$\text{Field strength} = Z_c/a^2 \qquad (1.2)$$

High value of field strength designates high bond energy in between cation and oxygen. Generally, network formers exhibit field strength > 1.5, while network modifiers have field strength < 0.4. On the other hand, the value of field strength for intermediates lies in the range of (0.5-1.0). Some of the field strength of ions is listed in the table 1.2.

1.3.4. Sun theory (1947)

Sun believed in single bond strength (SBS) theory. For a molecule, the equation of dissociation energy (E_d) is as follows:

$$M_xO_z \longrightarrow xM + zO \qquad (1.3)$$

Here dissociation energy is dependent on the thermodynamic lattice energy. It is ~ E_d/CN (kcal) for a single bond. Sun observed that if SBS for oxides is high (> 80 kcal/bond) then it will act as network former. For glass modifier, the SBS should be < 60 kcal/bond and if SBS value come in the range of (60-80 kcal/bond) then it will work as intermediate. Sun theory can also be understood with the help of melt crystallization. While cooling of quenched mass if that mass exhibit high bond strength then it is not easy to break or change into ordered

lattice. Hence, high bond strengths mass show high viscosity and act as excellent glass formers. On the other hand, low bond strengths mass can easily break/change and finally can convert into preferred crystal.

Table 1.2: Field strength of some glass modifier, Intermediate and network former ions **[6].**

Element	Valence (*Z*)	Most common co-ordination number	Ionic radius (for CN =6) (Å)	Ionic distance for oxides (a) (Å)	Field strength	Function in glass structure
Li	1	6	0.78	2.10	0.23	
Na	1	6	0.98	2.30	0.19	
K	1	8	1.33	2.77	0.13	Network
Sr	2	8	1.27	2.69	0.28	modifier
Ba	2	8	1.48	2.86	0.24	$Z/a^2 \approx$
Fe	2	6	0.83	2.15	0.43	0.1-0.4
Mn	2	6	0.91	2.23	0.40	
Ca	2	8	1.06	2.48	0.33	
Zr	4	8	0.87	2.28	0.77	
Mg	2	6	0.78	2.10	0.45	
		4		1.96	0.53	
Mn	2	4	0.83	2.03	0.49	
Al	3	6	0.57	1.89	0.84	Intermediate
		4		1.77	0.96	$Z/a^2 \approx$
Fe	3	6	0.67	1.99	0.76	0.5-1.0
		4		1.88	0.85	
Be	2	4	0.34	1.53	0.86	
Ti	4	6	0.64	1.96	1.04	
B	3	3	0.20	1.36	1.63	Network
P	5	4	0.34	1.55	2.10	former
Si	4	4	0.39	1.60	1.57	$Z/a^2 \approx$
Ge	4	4	0.44	1.66	1.45	1.5-2.0

1.4. TYPES OF GLASSES

The ingredients for glass preparation play very important role in the classification and application of glasses. Broadly four types of glasses are reported based on their initial ingredients sources; oxides glasses, chalcogenide glasses, sulfide glasses and metallic glasses. Moreover, they are further categorized such as single, binary, ternary, quaternary system etc. **[7-10].** Present study is related to the sulfides and oxides glasses, so in the next section the details of these glasses are given.

1.4.1. Borosilicate glasses

Different glasswares, high-power electric bulbs and pharmaceutical containers of borosilicate glasses are extensively used. They exhibit high thermal shock resistance and good heat resistant. For borosilicate glasses, as main constituents, silicon oxide and boron oxide are used in the range of (70-80%) and (7-13%), respectively. They are usually used in cooking utensils (oven ware or microwave) and chemical industry. Oxides of aluminum, potassium and sodium are added to increase the chemical durability of borosilicate glasses.

1.4.2. Soda-lime glasses

Soda-lime based glasses are commercially less expensive. They posses good light transmission and extensively used in window glasses. Soda–lime based glasses are also used as jars and glass containers. The main ingredients SiO_2 (60-75%), lime (CaO) and Na_2O (25-40%) are used in soda-lime glasses. These glasses have a big drawback like poor resistance at high temperatures which changes the properties unexpectedly.

1.4.3. Lead glasses

Lead glasses are generally used for decoration because of their high brightness and high refractive index. Lead glasses are prepared by using the ingredients SiO_2 (54-65 %), Na_2O (13-15 %) and PbO (18-38 %). In the prepared glass, if lead content is > 65 % then it is used for radiation shielding because lead can easily absorb γ-rays.

In addition to these glasses, some other glasses are also available and have their different properties like electronic conductivity, ionic conductivity, optical absorption and memory devices. To get good ionic conductivity, in host glass, some salts like NaCl, NaF, NaI, KI, KF, AgI, LiI, LiCl, LiF as dopants are added to get mobile ion like Na^+, K^+, Ag^+, Li^+ etc. These ion-containing glasses are called *fast ion-conducting glasses* which are discussed in the next section.

1.5. CLASSIFICATION OF FAST ION-CONDUCTING GLASSES

The glasses which exhibit ionic conductivity in the range of 10^{-1} to 10^{-4} Scm^{-1} at 300 *K* are called fast ion-conducting glasses. These fast ion-conducting glasses are generally used as solid electrolytes in batteries and sensors applications **[11].** High energy density, longer life, less leakage problem and simple thin films fabrication are the advantages of solid electrolytes over the liquid electrolytes. For batteries applications, solid electrolytes must have the following properties**:**

(a) Availability of large number of ions for good ionic conductivity.

(b) Negligible electronic conductivity.

(c) Low activation energy for migration of ions.

(d) Compatible with cathode and anode materials.

(e) Optimum elastic modulus for charging and discharging process.

(f) Cost effective.

Above mentioned properties can be achieved particularly good ionic conductivity by small ionic radius containing glass modifiers. Alkali ion-conducting glasses can be a good candidate for solid electrolyte applications because of **[12]:**

(a) Absence of grain boundaries that lead to isotropic properties.

(b) Easy to tailor the properties with wide variety of composition.

In 1973, Kunze reported the high conductivity of solid electrolyte in the $AgIAg_2SeO_4$ glassy system and proposed the high ionic conduction mechanism **[13].** In subsequent years, high conductive glasses/glass-ceramics as solid electrolyte and their working temperature were discovered. Some of them are explained below in brief with their properties.

1.5.1. Ag^+ conducting glasses

Silver ion conducting glasses with various glass formers exhibit high ionic conductivity (σ_{dc}). Most of these glasses contain silver iodide (AgI) as dopant. σ_{dc} increases with increasing AgI content though the room temperature phase of AgI is not a good ionic conductor. At atmospheric pressure, AgI mainly exist in three crystal polymorphs **[14].** Below 420*K*, AgI exhibit a stable β-phase with wurtzite structure. In β-phase, iodide ions are arranged in hcp structure while silver ions occupy the sub-lattice of interstitial tetrahedral sites. However, different than β-phase a γ-phase (metastable) is also present below 420*K*. This meta-stable phase exhibits zinc blende structure with iodide ions that occupy a cubic close packing. This can be viewed as layered ABABAB packing rather than ABCABC. Above 420*K*, AgI undergoes to a high temperature crystalline α-phase. This phase shows stability up to their melting temperature (828K). In α-AgI phase, migration of Ag^+ gives exceptionally high ionic conductivity **[15].** Instead of iodide some other halide ions are also used to enhance the conductivity like Br^- and Cl^-. Despite the highest ionic conductivity, silver-based glasses have several disadvantages like expensive, low energy density, exhibit low decomposition potential and low gravimetric energy density than Li-ion.

1.5.2. Cu^+ conducting glasses

In many glass systems, Cu^+ acts as a fast ionic conductor **[16, 17].** Copper-ion conducting glasses are used for fabrication of solid state cells. Halide based superionic glasses (CuI-CsI-BaI, CuCl-CuI-RbCl-KCl, CuI, CuBr-KBr-CsBr-$BaBr_2$) were synthesized for solid state cells **[18-20].** From fast-ion conducting point of view, Cu^+ based glasses are very suitable for solid electrolyte, because they exhibit high ionic conductivity at room temperature. In addition to this, Cu^+ based glasses are also synthesized to increase the durability of the glasses. Technologically, phosphate glasses are important because they usually have lower transition temperature, higher thermal expansion coefficients and higher electrical conductivity than

silicate and borate glasses **[21, 22].** However, their poor chemical durability makes them unsuitable for many applications **[23, 24].** It is observed that addition of CuO in phosphate glasses increases their chemical durability dramatically **[25].** On the other hand, the major problem with these glasses occurs during preparation in open atmosphere. The oxidation of Cu^{1+} (cuprous) to Cu^{2+} (cupric) ion, results in enhancement of electronic conductivity. Hence, to prevent the oxidation from Cu^{1+} to Cu^{2+}, it is necessary to synthesize the glasses under inert atmosphere. Sidhu *et al.* **[26]** investigated the preparation condition and conduction behavior of some Cu^{1+} ion conducting glasses in detail. Later on, some other Cu^{1+} ion conducting glasses were also studied, which are listed in the literature review section.

1.5.3. Li^+ conducting glasses

Since lithium is light and highly electro-positive, lithium-based glasses possess high energy power density and find potential applications in solid state batteries. However, their ionic conductivity (σ_{dc}) is not as high as that of silver-based glasses. In lithium containing SiO_2 based glasses, the conductivity increases with increasing content of Li_2O. Doping of these glasses with lithium halides such as LiCl, LiBr, LiI typically enhances σ_{dc} by several orders of magnitude **[27, 28]**. Lithium-ion conducting sulfide glasses show an increase in σ_{dc} more than three orders of magnitude when compared to the oxide glasses for the similar composition **[29].** This is due to the large ionic radius of sulfur ions (1.84 Å) and higher polarisability than oxide ions (1.4 Å). SiS_2, P_2S_5, B_2S_3 and GeS_2 are the commonly used glass formers in Li_2S based glasses. When two glass formers such as P_2S_5 and P_2S_3, GeS_2 and P_2S_5, or SiS_2 and GeS_2 are incorporated in the same glass, σ_{dc} is increased **[30, 31].** However, sulfide based glasses can react easily with ambient environmental moisture and can generate H_2S gas **[32].** Therefore, the handling of sulfide based solid electrolytes must be done in an inert atmosphere. On the other hand, partial substitution of oxygen atoms instead of sulfur atoms in sulfide electrolytes can suppress the H_2S gas generation **[33, 25].** Recently, Hayashi

et al. **[34]** prepared a composite electrolyte via mechanical milling for 90 mol % of $75Li_2S{\cdot}21P_2S_5{\cdot}4P_2O_5$ glass and 10 mol % of ZnO. In this work, partial substitution of P_2S_5 by P_2O_5, along with addition of ZnO, decreases the rate of H_2S generation in air atmosphere. However, the overall conductivity decreases with the addition of P_2O_5. In order to improve the ionic conductivity of glassy electrolytes, a number of systems have been proposed. One effective way is to mix two different anion species, also called "mixed anion effect", it can be mixed glass formers effect (MGFE) or mixed glass modifiers effect (MGME) **[35-37].** Lee *et al.* **[38]** added SeO_2 (network former or modifier) into binary $Li_2O–B_2O_3$ glassy electrolyte and observed an increase in ionic conductivity from 1.2×10^{-8} to 8×10^{-7} Scm^{-1} at room temperature**.**

1.5.4. Na^+ conducting glasses

Since last one decade Na^+ based glasses as solid electrolytes are in great demand because of their use in the sensors, fuel cells and batteries applications **[39, 40].** In 1985, Herczog *et al.* **[41]** reported the work on sodium ion-conducting glasses for the sodium-sulfur battery at 300 ^oC. Sodium sulfur battery is one of the most promising candidates for energy storage, space and transport applications **[42-44].** The Na/S battery is mainly composed of molten sodium as the negative electrode and sulfur as the positive. These electrodes are separated by β-Al_2O_3 ceramics as electrolyte. This electrolyte allows migration of only positively charged Na-ions. β-Al_2O_3 have the general formula xM_2O-$11A1_2O_3$ (where M is an alkali metal cation and $1.0 \leq x \leq 1.6$). It is well-known phenomenon that the high conductivity is exhibited due to mobile alkali cations located in a layer (known as the conduction plane) between spinel-structured alumina blocks. β-Al_2O_3 electrolyte generally used in tubular form has nominal chemical formula written as $NaAl_{(5.33–11)}O_{17}$. A schematic diagram of Na/S battery is shown in Fig. 1.2 (a). With different sodium/aluminum content ratio, β or β'' type structure can be formed.

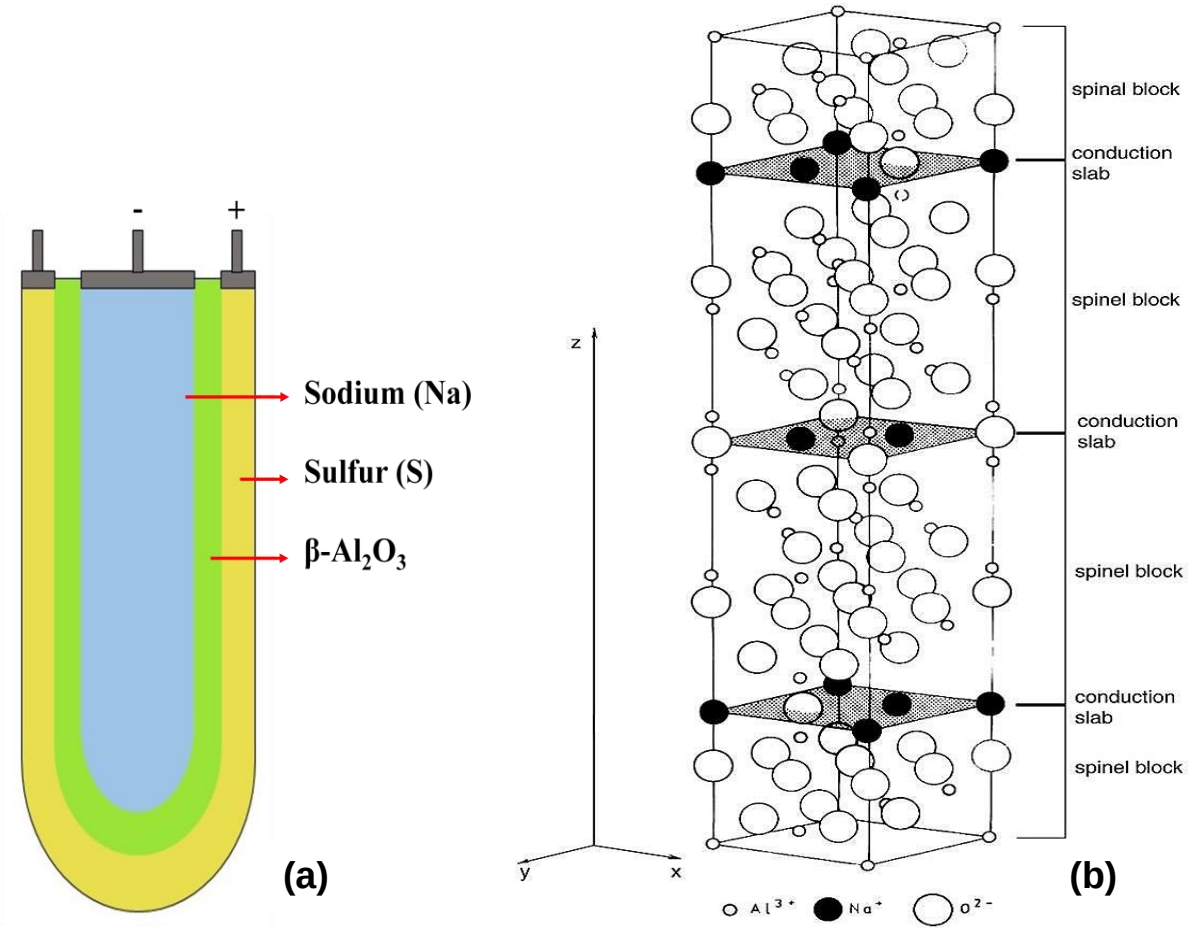

Fig. 1.2: Schematic diagram of **(a)** Na/S battery and **(b)** β''-Al_2O_3 structure **[46].**

Fig. 1.2 (b) shows the schematic structure of β''-Al_2O_3. It has tightly packed spinel block along-with loosely arranged conduction slab where the Na-ions could conduct rapidly **[45].** For each β-Al_2O_3 unit cell, two spinel structure blocks exist, while for β''-Al_2O_3 three spinel structure blocks are contained. Because of high sodium content in conduction plane, β''-Al_2O_3 shows high ionic conductivity than β-Al_2O_3. However, stabilization of β-Al_2O_3 phase is easy than β''-Al_2O_3. Typical conductivity of β-Al_2O_3 is 0.2 Scm^{-1} at 300 °C. For battery applications, β-Al_2O_3 works as solid electrolyte which is based on the electrochemical reaction between sodium and sulfur along with formation of sodium polysulfide and exhibits high power and energy density.

To replace this β-Al_2O_3 for better performance, new compounds $Na_{1+x}Zr_2Si_xP_{3-x}O_{12}$ ($0.4 \leq x \leq 2.8$) have been synthesized for Na/S batteries **[47].** For $x = 2$ composition, the $Na_3Zr_2Si_2PO_{12}$ phase shows comparable ionic conductivity (0.2 Scm^{-1}) of β-Al_2O_3 at 300 ºC. This phase $Na_3Zr_2Si_2PO_{12}$ is termed as NASICON. The fast sodium-ion transport in NASICON is related to the existence of three-dimensionally linked vacancies in a rigid structure of SiO_4 and PO_4 tetrahedra sharing corners with ZrO_6 octahedra. Fig. 1.3 shows the schematic diagram for NASICON structure.

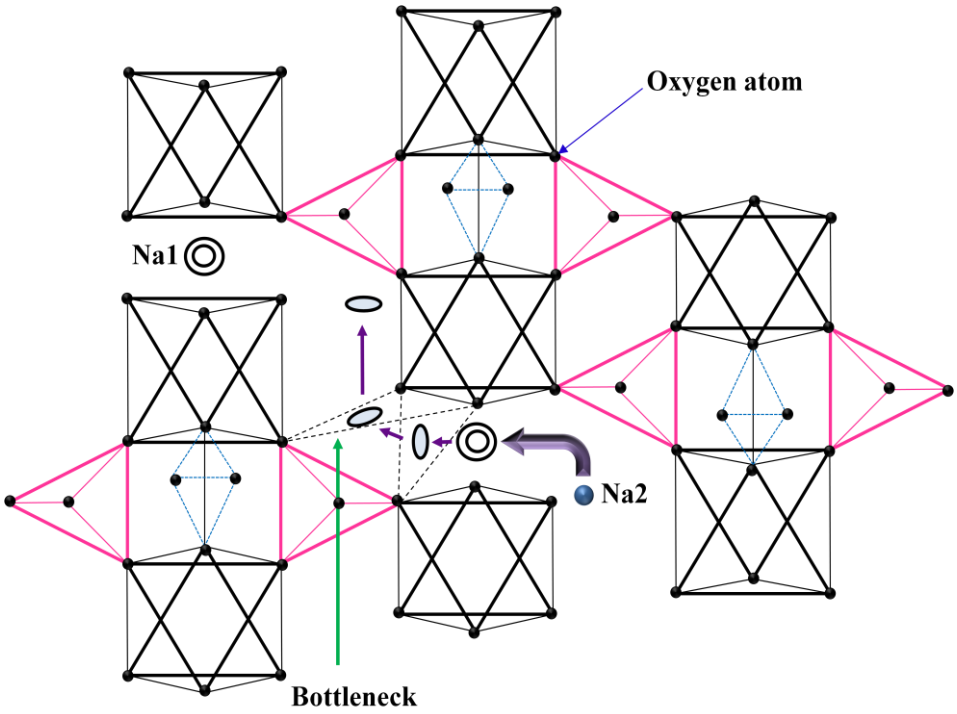

Fig. 1.3: Schematic diagram of NASICON structure.

This structure exhibits generally two types of Na sites (Na1 and Na2). The Na1 site is located between two octahedra along the c axis and other site Na2 is at midway of two Na1 sites along the axis **[48-51].** These two sodium sites are connected inside to channels through triangular bottlenecks of oxygen atoms. For the rhombohedral symmetry, the bottleneck formed between both sites is of atom of three oxygens, whose centres construct an isosceles triangle as shown in Fig. 1.3.

High ionic conductivity in this system depends upon movement of sodium ions, activation energy, size of bottleneck and lattice parameters whose value can be easily tailored by changing compositions **[52].**

Now in these days, glasses based solid electrolytes are being used for room temperature battery applications **[53-55].** It is already discussed in above section that in the glassy system, isotropic nature and absence of lattice ordering lead to high ionic conductivity. In general, sodium ion-conducting glasses can be divided into two classes: oxide and sulfide. For most of the oxide glassy electrolytes, the sodium-ion conductivity (10^{-6}-10^{-8} Scm^{-1}) at room temperature is too low to be used for high energy batteries **[56, 57].** While in the sulfide glasses, high sodium-ion conductivities of 10^{-4}-10^{-5} Scm^{-1} at room temperature can be achieved due to high polarizability of sulphur-ions for the $Na_2S–P_2S_5$ system **[58, 59].** Recently, Hibi *et al.* **[60]** prepared the glasses of (100-x) Na_3PS_4·xNaI ($0 \leq x(mol\%) \leq 33$) composition by a mechanochemical technique. They observed that with increasing content of NaI, ionic conductivity of glasses increases, and the highest conductivity of 1.4×10^{-5} Scm^{-1} is observed for the $71Na_3PS_4$·29NaI glass composition. However, Hayashi *et al.* **[61]** varied the time and temperature for Na_3PS_4 glasses to convert them into glass-ceramics. They reported the highest conductivity (4.6×10^{-4} Scm^{-1}) of Na_3PS_4 glass-ceramic, which was prepared after heat treatment of Na_3PS_4 glass at 270 °C for 1 h. This optimum Na_3PS_4 glass-ceramic shows ionic conductivity twice as high as the conductivity of the cubic Na_3PS_4 glass-ceramic.

In addition to ionic conductivity for solid electrolyte, elastic modulus is also very important factor to improve their overall efficiency. While charging and discharging of Na-ion batteries, it is observed that electrodes expand and contract. Consequently, the volume of active electrode material changes easily. This change results in breaking of electrode particles, which is the main cause of loss in capacity of batteries **[62].** Thus, a solid electrolyte should

have high ionic conductivity along-with moderate elastic modulus for improving the energy density and cycle performance of the Na-ion batteries. Nose *et al.* **[63]** reported the mechanical properties for $x$$Na_2S(100\text{-}x)P_2S_5$ (x = 50, 67, and 75) system. They used the ultrasonic pulse-echo technique to observe the longitudinal and shear velocities. With the help of these velocities, they calculated the value of Young's moduli (15–19 GPa), which is in desired range of sulfide solid electrolytes for Na-ion batteries.

In the present investigation, efforts have been made to synthesize sodium sulfide glasses in the presence of air and argon atmosphere to increase their stability with less H_2S generation. Moreover, for binary sodium-phosphate glass-ceramics, mechanical properties and their relationship with structural changes are discussed. The effect of modifiers (Li_2O/K_2O/CuS) on thermal stability and on crystallization kinetics in the sodium-phosphate glasses is also presented in detail.

REFERENCES:

[1] S.R. Elliott, Physics of Amorphous Materials, Longman, London (1984).

[2] W.D. Kingery, H.K. Bowen, D.R. Uhlmann, Introduction to Ceramics, 2nd ed., John Wiley and Sons, New York, (1976).

[3] S. Singh, G. Sharma, S. Thakur, K. Singh, Sci. Rep., **6,** (2016) 24617.

[4] P.W. Mcmillan, Glass-Ceramics, Academic Press, London, (1964).

[5] J.E. Shelby, Introduction to Glass Science and Technology, 2nd ed., The Royal Society of Chemistry, Cambridge, (2005).

[6] A. Dietzel, Sprechsaal, **62,** (1929) 506.

[7] L.S. Gallo, T.D.M. Mosca, B.H. Teider, I. Polyakova, A.C.M. Rodrigues, E.D. Zanotto, V.M. Fokin, J. Non-Cryst. Solids, **408,** (2015) 102.

[8] J.N. Ayuni, M.K. Halimah, Z.A. Talib, H.A.A Sidek, W.M Daud, A.W Zaidan, A.M. Khamirul, IOP Conf. Ser.: Mater. Sci. Eng. **17,** (2011) 012027.

[9] N. Elkhoshkhany, Rafik Abbas, R. El-Mallawany, A.J. Fraih, Ceram. Int., **40,** (2014) 14477.

[10] S.K. Arya, B. Kaur, G. Kaur, K. Singh, J. Therm. Anal. Cal., **120,** (2015) 1163.

[11] A. Pradel, M. Ribes, Mat. Sci. Eng., **B3,** (1989) 45.

[12] T. Minami, J. Non-Cryst. Solids, **73,** (1985) 273.

[13] D. Kunze, Fast Ion Transport in Solids, Ed. W.Vangoor, North Holland, Amsterdam, (1973). 405.

[14] L. Abbas, L. Bih, A. Nadiri, Y.E. Amraoui, D. Mezzane, B. Elouadi, J. Mol. Struct., **876,** (2008) 194.

[15] L. Bih, L. Abbas, S. Mohdachi, A. Nadiri, J. Mol. Struct., **891,** (2008) 173.

[16] N. Machida T. Minami, J. Am. Ceram. Soc., **71,** (1988) 784.

[17] T. Minami, Bull. Ins. Chem. Res., Kyoto Univ., **72,** (1994) 305.

[18] C. Liu, H.G.K. Sundar, C.A. Angell, Solid State Ionics, **18/19,** (1986) 442.

[19] K. Kadono, K. Mitani, H. Tanaka, Y. Kawamoto, K. Ohno, R. Kanno, Phys. Chem. Glasses, **32,** (1991) 207.

[20] O. Yamamoto, "Materials for Solid State Batteries", Eds. B.V.R. Chowdari, and S. Radhakrishna, World Scientific Publ. Co., Singapore pp. 263-273 (1986).

[21] H.A.A. Sidek, I.T. Collier, R.N. Hampton, G.A. Saunders, B. Bridge, Philos. Mag. B, **59,** (1989) 221.

[22] M. Szumera, I. Wacławska, Z. Olejniczak, J Therm. Anal. Calorim., **99,** (2010) 879.

[23] H. Yung, P.Y. Shih, H.S. Liu, T.S. Chin, J. Am. Ceram. Soc., **80,** (1997) 2213.

[24] M.R. Reidmeyer, M. Rajaram, D.E. Day, J. Non-Cryst. Solids, **85,** (1986) 186.

[25] T. Ohtomo, A. Hayashi, M. Tatsumisago, K. Kawamoto, J Mat. Sci, **48**, (2013) 4137.

[26] K.S. Sidhu, S.S. Sekhon, S.A. Hashmi, S. Chandra, J. Mater. Sci. Lett., **12,** (1993) 346.

[27] J. Swenson, R.L. McGreevy, L. Borjesson, J.D. Wicks, Solid State Ionics, **105,** (1998) 55.

[28] A. Hall, S. Adams, J. Swenson, J. Non-Cryst. Solids, **352,** (2006) 5164.

[29] M. Tatsumisago, S. Hama, A. Hayashi, H. Morimoto, T. Minami, Solid State Ionics, **15,** (2002) 635.

[30] H. Yamamoto, N. Machida, T. Shigematsu, Solid State Ionics, **175,** (2004) 707.

[31] K. Minami, A. Hayashi, S. Ujiie, M. Tatsumisago, J. Power Sources, **189,** (2009) 651.

[32] H. Muramatsu, A. Hayashi, T. Ohtomo, S. Hama, M. Tatsumisago, Solid State Ionics, **182,** (2011) 116.

[33] T. Ohtomo, A. Hayashi, M. Tatsumisago, K. Kawamoto, J. Non-Cryst. Solids, **364,** (2013) 57.

[34] A. Hayashi, H. Muramatsu, T. Ohtomo, S. Hama, M. Tatsumisago, J. Alloys Com. **591,** (2014) 247.

[35] R.B. Christensen, The mixed glass former effect in $0.35Na_2O+0.65[xB_2O_3+(1-x)P_2O_5]$ glasses, Ph.D dissertation, Iowa State University Ames, Iowa (2012).

[36] A. Chandra, A. Bhatt, A. Chandra, J. Mat. Sci. Technol., **29,** (2013) 193.

[37] V.K. Deshpande, Ionics, **10,** (2004) 20.

[38] C.H. Lee, K.H. Joo, J.H. Kim, S.G. Woo, H.J. Sohn, T. Kang, Solid State Ionics, **149,** (2002) 59.

[39] N. Tanibata, K. Noi, A. Hayashi, M. Tatsumisago, RSC Adv., **4,** (2014) 17120.

[40] C. Bischoff, K. Schuller, M. Haynes, S.W. Martin, J. Non-Cryst. Solids, **358,** (2012) 3216.

[41] A. Herczog, J. Electrochem. Soc.: Electrochem. Sci. Technol., **132,** (1985) 1539.

[42] N. Yabuuchi, M. Kajiyama, J. Iwatate, H. Nishikawa, S. Hitomi, R. Okuyama, R. Usui, Y. Yamada, S. Komaba, Nat. Mater., **11,** (2012) 512.

[43] S.M. Wolannyk, S.P. Vukson, Proc. 25th IECEC Conf., **3,** (1990) 122.

[44] K.B. Hueso, M. Armand, T. Rojo, Energy Environ. Sci., **6,** 2013, 734.

[45] D.H. Doughty, P.C. Butler, A.A. Akhil, N.H. Clark, J.D. Boyes, Electrochem. Soc. Interface, **19,** (2010) 49.

[46] P.T. Moseley, in: Sodium sulfur battery, eds. J.L. Sudworth and A.R. Tilley (Chapman and Hall, London, New York, p. 23, (1985).

[47] U.V. Alpen, M.F. Bell, W. Wichelhaus, Mat. Res. Bull., **14,** (1979) 1317.

[48] P. Yadav, M.C. Bhatnagar, Ceram. Int., **38,** (2012) 1731.

[49] J.P Boilot, G. Collin, P.h. Colomban, J. Solid State Chem., **73,** (1988) 160.

[50] H. Kohler, H. Schulz, Mat. Res. Bull., **20,** (1985) 1461.

[51] J.B. Goodenough, H.P.Y. Hong, J.A. Kafalas, Mat. Res. Bull., **11,** (1976) 203.

[52] A.M. Juarez, C. Pecharroman, J.E. Iglesias, J.M. Rojo, J. Phys. Chem. B, **102,** (1998) 372.

[53] A. Hayashi, R. Ohtsubo, T. Ohtomo, F. Mizuno, M. Tatsumisago, J. Power Sources, **183,** (2008) 422.

[54] A. Hayashi, S. Hama, T. Minami, M. Tatsumisago, Electrochem. Commun., **5,** (2003) 111.

[55] A. Yamauchi, A. Sakuda, A. Hayashi, M. Tatsumisago, J. Power Sources, **244,** (2013) 707.

[56] M. Ribes, B. Barrau, J.L. Souquet, J. Non-Cryst. Solids, **38/39,** (1980) 103.

[57] C. Lim, D.E. Day, J. Am. Ceram. Soc., **61,** (1978) 99.

[58] A. Hayashi, K. Noi, A. Sakuda, M. Tatsumisago, Nature Commun., **3,** (2012) 856.

[59] K. Noi, A. Hayashi, M. Tatsumisago, J. Power Sources, **269,** (2014) 260.

[60] Y. Hibi, N. Tanibata, A. Hayashi, M. Tatsumisago, Solid State Ionics, **270,** (2015) 6.

[61] A. Hayashi, K. Noi, N. Tanibata, M. Nagao, M. Tatsumisago, J. Power Sources, **258,** (2014) 420.

[62] M. Nagao, A. Hayashi, M. Tatsumisago, Electrochim. Acta, **56,** (2011) 6055.

[63] M. Nose, A. Kato, A. Sakuda, A. Hayashi, M. Tatsumisago, J. Mat. Chem. A, **3,** (2015) 22061.

Chapter-2

(Literature review)

- **Oxide glasses/glass-ceramics**
- **Sulfide glasses/ glass-ceramics**
- **Oxysulfide glasses/glass-ceramics**
- **Structural, thermal and mechanical properties of glasses/glass-ceramics**
- **Mixed ions effect on stability and conductivity**

The conductivity of glasses has been studied since 1884, when Warburg used dc electrical field and found Na^+ transportation **[1].** Since then lots of research has been done in oxide glasses containing alkali ions and confirmed the ionic conduction behavior **[2, 3].** They observed the electrical conductivity in the range of (10^{-9}-10^{-13} Scm^{-1}) at ambient temperature which was too low to use them as solid electrolyte for batteries applications. In subsequent years, different halide, oxide, sulfide and combined oxide and sulfide based glasses/glass-ceramics are synthesized to increase the ionic conductivity and check their suitability as solid electrolyte for batteries applications. Some of the examples of glass/glass-ceramic systems with their ionic conductivity at ambient temperature are listed in the table 2.1. In addition to ionic conductivity, elastic modulus of solid electrolyte is also very essential parameter to maintain/improve their overall efficiency. So, in this chapter, literature review regarding alkali ions effect on ionic conductivity and on stability of glasses as solid electrolytes for batteries applications is presented.

Table 2.1: Glass/glass-ceramic systems with their ionic conductivity at room temperature.

System	Conductivity (S cm^{-1})	Reference
$Ag_2S–GeS_2$	1.4×10^{-3}	[4]
$Ag_2S–As_2S_3$	1.0×10^{-4}	[4]
$Ag_2S–P_2S_5$	2.7×10^{-5}	[4]
$AgI–Ag_2O–B_2O_3$	8.5×10^{-3}	[5]
$AgPO_3–Ag_2SO_4$	5.0×10^{-6}	[6]
$AgI\text{-}Ag_2O\text{-}V_2O_5$	9.0×10^{-3}	[7]
$AgI\text{-}Ag_2O\text{-}MoO_3$	1.0×10^{-2}	[7]
$AgI\text{-}Ag_2O\text{-}PbO\text{-}B_2O_3$	9.0×10^{-3}	[8]
$Sb_2S_3\text{-}Ag_2S\text{-}AgI$	6.0×10^{-2}	[9]
$AgI\text{-}Ag_2O\text{-}SeO_2\text{-}V_2O_5$	2.4×10^{-2}	[10]
CuI-CuCl-RbCl	1.0×10^{-2}	[11]
$CuI\text{-}Cu_2O\text{-}P_2O_5$	1.0×10^{-2}	[12]
$CuI\text{-}Cu_2MoO_4\text{-}Cu_3PO_4$	1.0×10^{-2}	[13]
$CuI\text{-}Cu_2O\text{-}P_2O_5\text{-}B_2O_3$	1.0×10^{-3}	[14]
$CuO\text{-}Ag_2O\text{-}V_2O_5$	4.5×10^{-6}	[15]

$CuI-Cu_2O-MoO_3-WO_3$	3.0×10^{-4}	[16]
$CuI-Cu_2O-MoO_3$	1.0×10^{-2}	[17]
$CuI-Cu_2MoO_4$	1.0×10^{-3}	[18]
Li_2O-SiO_2	1.0×10^{-5}	[18]
$Li_2O-P_2O_5$	2.8×10^{-7}	[19]
Li_2S-GeS_2	4.0×10^{-5}	[20]
$Li_2S-P_2S_5$	1.0×10^{-4}	[21]
Li_2S-SiS_2	5.0×10^{-4}	[22]
$Li_2S-SiS_2-Li_4SiO_4$	2.0×10^{-3}	[23]
$Li_2S-SiS_2-Li_3PO_4$	2.0×10^{-3}	[24]
$Li_2S-P_2S_5-P_2O_5$	1.7×10^{-4}	[25]
$Li_2S-Li_2O-P_2S_5$	2.7×10^{-4}	[26]
$Li_2S-B_2S_3$	2.0×10^{-4}	[27]
$P_2S_5-B_2S_3-Li_2S$	1.4×10^{-1}	[28]
$LiI-Li_2S-B_2S_3$	1.7×10^{-3}	[29]
$LiI-LiPO_3$	1.0×10^{-6}	[30]
$Li_2S-LiI-P_2S_5$	1.0×10^{-3}	[31]
$Li_2S-GeS_2-Ga_2S_3$	1.0×10^{-5}	[32]
$LiI-Li_2S-GeS_2-Ga_2S_3$	1.0×10^{-3}	[32]
$LiI-Li_2S-GeS_2-La_2S_3$	1.0×10^{-4}	[32]
$LiI-Li_2S-SiS_2$	1.8×10^{-3}	[33]
$LiI-Li_2S-GeS_2$	1.2×10^{-4}	[34]
$Li_2O-P_2O_5-LiCl$	0.9×10^{-6}	[35]
$Li_2O-P_2O_5-LiBr$	2.7×10^{-6}	[35]
$Li_2S-P_2S_5-LiBr$	3.1×10^{-4}	[26]
$Na_2O-P_2O_5$	1.0×10^{-9}	[37]
Na_2O-SiO_2	2.0×10^{-7}	[38]
Na_2S-SiS_2	1.1×10^{-5}	[38]
Na_2O-GeO_2	2.3×10^{-8}	[39]
Na_2S-GeS_2	1.0×10^{-6}	[40]
$Na_2O-P_2O_5-CdCl_2$	1.9×10^{-7}	[41]
$Na_2O-P_2O_5-CoCl_2$	2.2×10^{-7}	[41]
$Na_2O-P_2O_5-AgCl$	1.4×10^{-3}	[41]
$Na_2S-P_2S_5$ (glass)	1.0×10^{-5}	[42]
$Na_2S-P_2S_5$ (glass-ceramic)	2.0×10^{-4}	[43]
$Na_2S-Na_2O-P_2O_5$	3.9×10^{-7}	[44]
$Na_3PS_4-Na_4SiS_4$ (glass-ceramic)	7.4×10^{-4}	[45]
$Na_2S-B_2S_3-P_2S_5$	7.7×10^{-3}	[46]

In 1971, Evstrop'ev *et al.* **[47]** were first to report the fast ion conduction (FIC) in phosphate glasses for the composition M_2O-MF-$Al(PO_3)_3$ (M = Na, Li, K and Cs). Maximum conductivity 10^{-2} Scm^{-1} was obtained for the glass $30Li_2O$-50LiF-$20Al(PO_3)_3$ composition at 300 °C. Malugani *et al.* **[30]** have studied the phosphate glasses $LiPO_3$-LiX (X = C1, Br, I) and reported that ionic conductivity increases with increasing halide content. In general, independent composition of LiI always increases the ionic conductivity.

Doreau *et al.* **[48]** investigated the range of glass forming region for Li_2O–P_2O_5–LiCl system and reported that ionic conductivity increases with LiCl content, while glass transition temperature (T_g) decreases with LiCl content. In addition to this, they studied the Raman spectroscopy for the same system and observed that with the addition of Li_2O content non-bridging oxygens (NBOs) increases, which reduces the chain lengths of P–O–P bridges. More structural investigation was done by Tatsumisago *et al.* **[49]** for the same system and observed that no P-Cl bonds are formed. However, LiCl get dissolve interstitially in the $LiPO_3$ glassy phase.

Tanaka *et al.* **[50]** prepared the glass compositions of LiCl–Li_2O–TeO_2 by melt-quench technique and investigated the ionic conductivity and structural changes with LiCl content. They concluded that NBOs leading to the formation of Te–Cl_{eq} bonds. Here *eq* represents the equatorial position of the trigonal bipyramid in the TeO_4 unit. They reported the ionic conductivity ~ 10^{-6} Scm^{-1} at ambient temperature which is comparable to the Na^+ and Li^+ ion conducting glasses. A comparative study was done for LiBr doped lithium tellurite glasses with LiCl doped glasses and reported that the thermal expansion values and ionic conductivity are lower for LiBr doped glasses. On the other hand, T_g is observed at higher temperature for LiBr than LiCl doped glasses. These phenomena can be understood with the help of formation of lesser amount of $(TeO_3)^{2-}$ trigonal pyramids and weak Te–O_{ax} bond (ax = axial position) in the

LiBr than in LiCl doped lithium tellurite glasses **[51].** In order to obtain high ionic conductivity many oxide glasses consisting different glass formers (P_2O_5, B_2O_3, V_2O_5, etc.) with metal oxide M_2O (M = Li, Na and K) containing different doping salt MX (X = Br, I, Cl and F) are investigated **[52-55].** In the beginning, conventional inorganic oxide glasses and later on sulfide or oxysulfide glasses were investigated. However, different types of glasses such as halides, oxides and sulfide glasses have their own advantages in different applications.

The structure and properties of oxide glasses have been investigated in detail for binary (Me_2O-X) systems; (Me = Li, K, Na, Cs, Ag, Rb); (X = P_2O_5, B_2O_3, SiO_2, GeO_2 etc.) **[37-39, 56-61]**. Moustafa *et al.* **[62]** studied the structural behavior for Na_2O-P_2O_5 system by FTIR spectroscopy and concluded that substitution of P_2O_5 by Na_2O creates NBOs. Increasing content of Na_2O leads to depolymerization of the phosphate ring type structures, consequently, compact glass matrix is observed. Brow *et al.* **[63]** investigated the short range order for the same sodium-phosphate system by Nuclear Magnetic Resonance (NMR). They observed the presence of Q^3-(3 bridging oxygen/tetrahedron) and Q^2-(2 bridging oxygen/tetrahedron) tetrahedral sites in the glasses for less than 50 mol% of P_2O_5, while for more than 50 mol% of P_2O_5, Q^1 and Q^2 tetrahedral units are observed.

Money *et al.* **[64]** prepared the glasses of Li_2O-P_2O_5 system by melt-quench technique and studied the crystallization kinetics at different heating rates. They reported that structure of metaphosphate glasses consist of long entangled chains of tetrahedral structural units, which is a main cause of high activation energy for internal structural relaxation. In addition to this, they concluded that ionic conductivity falls 4 order magnitudes in the $LiPO_3$ ceramic phase than in the same glassy phase. The same behavior is also found in the sodium-phosphate binary system [**65].** Glass *et al.* **[66]** synthesized $LiTaO_3$, $LiNbO_3$, $KTaO_3$ and $KNbO_3$ glasses by melt-quench technique with enhanced ionic conductivity compared to their crystalline counterpart.

In comparisons, lithium-phosphate glasses show high ionic conductivity than sodium-phosphate glasses at room temperature due to smaller size of Li^+ (0.76 Å) as compared to Na^+ (1.02 Å). To increase the ionic conductivity in the above binary systems, sulfate compound were incorporated and the resultant ternary systems (Me_2O-$MeSO_4$-P_2O_5); (Me = Na, Li); were investigated **[67, 68].** The ionic conductivity increases 10^3 times in these systems with decrease in activation energy at room temperature. Insertion of this sulfate compound increases the number of dissociated lithium and sodium ions (charge carriers) and decreases the dissociation energy for polar structural chemical units.

Rani *et al.* **[69]** prepared the glass composition $(25+x)Li_2O.(65-x)P_2O_5.10Bi_2O_3$ ($0 \leq x \leq 25$ mol%) by melt-quench technique and studied the structural changes and optical band gap in lithium-bismuth phosphate glasses. In the optical spectra, no sharp edges were observed which confirmed the amorphous nature of the glasses. Formation of NBOs and P-O-Bi bonds plays very important role in variation in the optical band gap, optical absorption edge and Urbach energy. With increase in Li_2O content, optical band gap decreases and the values reaches in the semiconductors range. Moreover, addition of Li_2O in the glass matrix disrupted the long chains of phosphate groups and lowers the T_g.

Sanghi *et al.* **[70]** investigated the impedance spectroscopy for the same system in the temperature range (150-300 °C) and in the frequency range (20Hz-1MHz). The ionic conductivity in these glasses follows the Arrhenius law and observed that it increases with increase in Li_2O content. However, the value of conductivity exponent (n) decreases which means local conduction space is decreasing and simultaneously the restriction for Li^+ ion movement is increasing. This discrepancy in ‘‘n’’ has been associated with the presence of 10 mol% of Bi_2O_3. It is well reported that addition of Bi_2O_3 leads to de-polymerization in sodium

metaphosphate chains and formation in Bi–O–P bonds. This change in structural units restricted the Li^+ ions movement and decreases the value of ''*n*'' **[71].**

Thombre *et al.* **[72]** investigated the physical parameters like density, molar volume, ionic concentration, polaron radius, oxygen packing density etc. for the sodium-borophospahte glasses. They observed that with increase of P_2O_5 content by replacing B_2O_3, ionic concentration and oxygen packing density decreases; whereas inter-ionic distance, molar volume and polaron radius increases.

Carta *et al.* **[73]** studied the relationship between structure and thermal stability for $40(P_2O_5)$-$x(B_2O_3)$-$(60-x)(Na_2O)$; ($10 \leq x \leq 30$ mol%) system. Raman, FTIR and NMR spectroscopy were used for phosphate structural changes. Analysis of the data indicated that with increasing B_2O_3 content on the expense of Na_2O, the glass network shows cross-linking between borate and phosphate units by formation of P–O–B bonds. Addition of B_2O_3 in the sodium-phosphate glasses increases the bond strength and thermal stability of the system.

Qiu *et al.* **[74]** examined the structure and thermal stability of aged sodium borophosphate glasses by NMR spectroscopy, high-energy X-ray diffraction and DTA. Similar to the fresh samples, both P-O-B and P-O-P bonds were found in these glasses. NMR spectroscopy confirmed that the cross-linking between phosphate and borate units increases with B_2O_3 content. Interestingly upon aging, the glasses were found to hydrolyze and cause the network to degrade. DTA and XRD results show that the glasses with increasing boron oxide content have a higher tendency towards crystallization when exposed to moisture.

In order to improve the chemical durability and thermal stability Shih *et al.* **[75]** added the CuO in sodium-phosphate glasses. The short range structures in this ternary compound were investigated by FTIR and X-ray photoelectron spectroscopy. In the meta-phosphate and ultra-phosphate glasses, the P-O-Cu bonds are formed by replacing $P\text{-}O^-Na^+$ bonds as Na_2O is

replaced by CuO. However, in the polyphosphate glasses, P-O-Cu bonds are formed by replacing the both $P\text{-}O^{-}Na^{+}$ and P-O-P bonds. The formation of P-O-Cu bonds in sodium-phosphate glasses increases the cross-link density. Hence chemical durability and T_g increases simultaneously in these glasses.

Mirzayi *et al.* **[76]** prepared the $45(P_2O_5)$-x(CuO)-$(55-x)(Li_2O)$; ($10 \leq x \leq 30$ mol%) glass compositions and studied their thermal stability and structural properties. IR study showed the presence of pyrophosphate and metaphosphate structures. It is observed that with increase of CuO content in lithium-phosphate glasses, the big skeleton of metaphosphate chains are broken into short pyrophosphate groups. In addition to this, decrease in band gap with increase in thermal stability is observed with CuO content.

Aqdim *et al.* **[77]** prepared the glass composition Li_2O-Fe_2O_3-P_2O_5 by melt-quench technique and investigated the structural properties and thermal stability. The prepared glasses for all compositions showed good chemical resistance with Fe_2O_3 content. The improved chemical resistance in these glasses was attributed due to replacement of hydrated Li-O-P and P-O-P bonds by corrosion-resistant Fe-O-P bonds. With an increase of Fe_2O_3 content, the number of Fe-O-P bonds increased and became stronger. The IR spectra designates that these glasses contain a large number of Fe-O-P bonds and dominated by $(PO_3)_3^{3-}$ and $P_2O_7^{4-}3$ dimer units. The structural changes because of Fe_2O_3 content increased the tendency towards crystallization and increased the chemical durability.

In addition to this, mixed anions effects on structural properties, electrical conductivity, and thermal stability in the oxide glasses have been investigated in detail to check their suitability for certain applications.

Fang *et al.* **[78]** examined the effect of mixed K_2O and Na_2O on the stability and conductivity in the iron-phosphate glasses. They prepared the two series of glass compositions xK_2O-(20-x)Na_2O-$32Fe_2O_3$-$48P_2O_5$ and xK_2O-(20-x)Na_2O-$20Fe_2O_3$-$60P_2O_5$; ($0 \leq x \leq 20$) by melt-quench technique. For these glasses, no usual mixed alkali effect, like a maximum or minimum in the properties was observed. However, they observed the mixed electrical conductivity (ionic due to alkali ions + electronic due to iron electron hopping) in the range of ~ 10^{-5} Scm^{-1} at ambient temperature. Moreover, they have also concluded that the fraction of electronic conductivity was higher than the ionic conductivity.

Faivre *et al.* **[79]** investigated the mixed alkali ions (Li, Na) effect on the glass transition, electrical conductivity and elastic modulus in the aluminophosphate glasses. It is well reported by Brow *et al.* **[80]** that with increase of Al_2O_3 content in phosphate glass an increase in the T_g occurs. However, in the present case a decrease in the magnitude of glass transition is observed with increases in Al_2O_3 because of mixed alkali ions effect. The dc conductivity is not affected by the addition of Al_2O_3 content in single alkali glasses, while in the mixed alkali phosphate glasses the addition of Al_2O_3 content shows non-linear behavior in dc conductivity. On the other hand, as alumina content increases almost linear increase in the elastic modulus is observed. This phenomenon can be understood on the basis of strong bonds formation. Al_2O_3 increases the covalency in the P–O bonds and form the aluminophosphate bonds, which increases the overall strength of the glass structure, consecutively elastic modulus increases.

Abbas *et al.* **[81]** studied the properties of Na_2O and Li_2O modified molybdenum phosphate glasses. The prepared glasses were characterized by various techniques; X-ray diffraction, differential thermal analysis and impedance spectroscopy. T_g and ionic conductivity shows a minimum when the ratio of Na/(Na+Li) is = 0.5. Contrary to this, the density values shows linear behavior with Na/(Na+Li) ratio. The ionic conductivity for the ratio of Na/(Na+Li) = 0.5

is observed about 3 orders lower than that of the individual Na and Li analogue glasses. This behavior could be attributed due to the two types of alkali ions (Li and Na) which are randomly mixed and have different conduction pathways. This implies that Na ions tend to restrict the pathways for the Li ions and vice versa. The same mixed alkali effect is also reported in the literature and explanation has been elaborated in the detail on the basis of different conduction pathways and structural changes **[82-84].**

Milankovic *et al.* **[85]** investigated the electrical conductivity of mixed alkali (Li, Na, K), iron-phosphate glasses at room temperature. The electrical conductivity varied slightly with alkali content in the iron-phosphate glasses. They observed that the ionic conductivity of iron-phosphate glasses without alkali ions was 5-10 times higher than that of 20 mol% of potassium or sodium containing iron-phosphate glasses. In conclusion, they reported that electrical conductivity in these glasses is dominated by electron hopping and mobility of potassium and sodium ions is too low to contribute the overall electrical conductivity.

Samee *et al.* **[86]** prepared the mixed alkali (Li, Na, K) borate glasses and studied their optical and physical properties. T_g, density, Urbach energy and band gap energy of the prepared glasses shows non-linearly with compositional parameter and show signs of mixed alkali effect. On the basis of optical basicity and other parameter calculation they concluded that these glasses are normal ionic oxides.

According to Deshpande *et al.* **[87]** an increase in ionic conductivity can be obtained by using mixed glass formers in the alkali oxide glasses. They prepared the glass compositions of Li_2S-SiS_2-GeS_2 and have shown an increase in the ionic conductivity upto two orders of the magnitude. Here SiS_2, GeS_2, Bi_2O_3 and B_2O_3 act as glass formers. This phenomenon was termed as mixed glass former effect (MGFE).

Tsuchiya *et al.* **[88]** prepared the glass compositions $40R_2O$-xB_2O_3-$(60-x)P_2O_5$ and $30R_2O$-xB_2O_3-$(70-x)P_2O_5$; (R = Li or Na) by melt-quench technique and reported an increase in T_g, Vickers hardness, density and ionic conductivity. The ionic conductivity observed in the mixed glass formers glasses was two orders higher than either of the binary (B_2O_3-P_2O_5) glasses. Tsuchiya proposed that this increase in the above properties were related to the formation of strong mixed network between the phosphorus and boron. This phenomenon was further supported by Anantha *et al.* **[89]** for $50Na_2O+50[(1-x)P_2O_5+xB_2O_3]$ glass compositions. T_g value increases with increase of B_2O_3 content in the sodium-phosphate glasses due to cross-linking in the network. FTIR study confirmed that when P_2O_5 is replaced by B_2O_3, new strong bonds are formed which increases the thermal stability. The compositional effect on ionic conductivity was studied by impedance spectroscopy and confirmed that charge transport in the glasses was mainly due to hopping of sodium ions in the lattice.

Zielniok *et al.* **[90]** established the relationship between physical and structural properties for the $0.4Na_2O$-$0.6[xB_2O_3$-$(1-x)P_2O_5]$ glasses by using NMR and Raman spectroscopy. They concluded that two network formers, phosphorus oxide and boron oxide results in the formation of P-O-B linkages. Compared to binary borophosphate and sodium-phosphate glasses, the network polymerization in the ternary system is increased significantly.

Pradel *et al.* **[91]** studied the structural and physical properties of glass compositions $0.3Li_2S+0.7[(1-x)SiS_2+xGeS_2]$ using small angle x-ray scattering (SAXS) and Raman spectroscopy. They proposed the phase separation mechanism in the region ($0.5 \leq x \leq 0.64$). SAXS analysis confirmed the presence of clusters or aggregates of 50 Å in size. Moreover, Raman spectra showed the bands for GeS_2 and Li_2SiS_3 phases and found high ionic conductivity which is almost close to the individual Li_2SiS_3 phase. The electrical conductivity for the glass $0.4Li_2O+0.6[(1-x)Si_2O_4+xB_2O_3]$ system was studied by Maia *et al.* **[92].**

However, they reported a decrease in the electrical conductivity with mixed glass formers. Kluvanek *et al.* **[93]** investigated the ionic conductivity for $0.4Li_2O+0.6[xB_2O_3+(1-x)2SiO_2]$ glasses and surprisingly effect of mixed glass formers was not observed in these glasses. In addition to this, more investigation were also done in detail to understand the effect of mixed glass formers on structure and electrical conductivity in alkali containing glasses **[94-98].**

From the above study, it can be concluded that several possibilities have been attempted to increase the ionic conductivity in oxide glasses as solid electrolyte for batteries applications. In addition to this, to improve the ionic conductivity in glasses, oxides are replaced by sulfides to check their possible use for batteries applications. Sulfide based glasses show ~10^3 times higher ionic conductivity than for the same compositions of oxide based glasses. High ionic conductivity in sulfide based glasses is observed due to high polarizabilities of sulfide ions **[20, 99].**

Ribes *et al.* **[40]** prepared the glasses for Na_2S-XS_2; (X = Ge, Si), Li_2S-GeS_2 and Na_2S-P_2S_5 systems by melt-quench technique. With the help of electromotive force measurements, the ionic transport number obtained was equal to 1. They reported the ionic conductivity ~ 4×10^{-5} S cm^{-1} for glass composition $0.5Li_2S$-$0.5GeS_2$ at room temperature. They concluded that for the same composition, replacement of oxygen atom by a sulfur atom increases the ionic conductivity from 10^{-7} to 10^{-5} Scm^{-1} at room temperature.

Minami *et al.* **[100]** synthesized the Li_2S–P_2S_5 based glasses by melt-quench technique and heated them above their crystallization temperature to convert them into glass-ceramics and investigated their ionic conductivity at room temperature. They demonstrated that local structure of the glasses depends on the melting temperature of the compositions. The increase in melting temperature (750-900 °C) led to form $P_2S_6^{4-}$ ions, which facilitate to crystallize low ionic conducting $Li_4P_2S_6$ phase. Raman analysis confirmed the presence of $P_2S_6^{4-}$ ions in these

glasses. However, meta-stable super-ionic $Li_7P_3S_{11}$ phase can be obtained by controlled heat treatment of the glasses at 750 °C. This super-ionic glass-ceramic ($Li_7P_3S_{11}$ phase) showed high ionic conductivity ~ 2.1×10^{-3} Scm^{-1} at room temperature.

Tatsumisago *et al.* **[101]** prepared the glass compositions xLi_2S-$(100-x)P_2S_5$; (x = 60, 70, 75, 80, and 87.5) by mechanochemical method. High ion-conducting glass-ceramic (Li_7PS_6, Li_3PS_4) phases were obtained after heat treatment of as prepared glasses above their crystallization temperature. Ionic conductivity (σ) measured at room temperature was found to be composition dependent. The value of ionic conductivity at room temperature (σ_{25}) increases as x increases and shows a maximum value for the composition range ($75 \leq x \leq 80$). However, further increase in x decreases the σ_{25}. Activation energy (E_a) calculations also support this result. The simultaneous behavior; decrease of E_a and increase of σ_{25} with increasing Li_2S up to 75 mol% can be understand with either high mobility of Li^+ ions or increase of carrier concentration. The decrease in ionic conductivity with further x indicates that glasses are having low-conducting Li_2S crystals. The σ_{25} of the prepared glass-ceramics having Li_3PS_4 and Li_7PS_6 crystalline phases were 1×10^{-7} Scm^{-1} and 8×10^{-5} Scm^{-1}, respectively.

Extensive work has been done by many researchers to synthesize Li_2S-P_2S_5 based high ion-conducting glasses and glass-ceramics as solid electrolyte for batteries applications **[102-108].**

However, considering the large demand of lithium-ion batteries, researchers are focusing on another set of Na_2S based rechargeable batteries to utilize the abundant availability of sodium sources to make it cost effective than Li^+ batteries. The replacement of Li_2S by Na_2S in P_2S_5 glasses may have some other benefits also. Firstly, the Na_2S is easily available and cost effective material than Li_2S. Secondly, the ionic radius of P^{5+} (0.17 Å; C.N. 4) glass former and Na^+ (1.02 Å; C.N. 6) glass modifier has higher ionic radii deference than P^{5+} (0.17 Å; C.N. 4) and Li^+ (0.76 Å; C.N. 6). Higher difference in ionic radii leads to reduction in the T_g and T_c of

these glasses. Since their T_c are lower than Li_2S-P_2S_5 glasses so Na_2S containing glasses can be easily converted into glass ceramics, which have better mechanical properties than their glass counterpart.

Berbano *et al.* **[109]** prepared the glass compositions $x$$Na_2S$-(1-$x$)$P_2S_5$; ($x$ = 0.25, 0.33, 0.50, 0.67, 0.70, 0.75) by melt-quench and mechanochemical technique and investigated their structural properties using FTIR and Raman spectroscopy. The mechanically milled and melt-quenched samples with the compositions $0.50 \leq x \leq 0.67$ exhibited the similar Raman and FTIR spectra. This phenomenon indicated that very similar short range order structures are present in the glasses obtained from the different methods. It was observed that chemical reaction between Na_2S and P_2S_5 in the Na_2S-P_2S_5 system showed similar behavior to that of the Li_2S-P_2S_5.

Bischoff *et al.* **[110]** prepared the glass compositions $y$$Na_2S$+(1−$y$)$PS_{5/2}$ by melt-quench technique and investigated their structural properties using FTIR and Raman spectroscopy. For the composition, y = 0.33, 0.5 and 0.6 they named as meta-thiophosphate, pyrothiophosphate and orthothiophosphate structure. For y = 0.33, they observed $NaPS_3$ phase which consists mainly chains of corner shared P^2 and (NaS)$PSS_{2/2}$ units. Moreover, they found a small signature of edge-shared tetrahedral, which form dimers of $Na_2P_2S_6$ composition. However for y = 0.5, two P^1 and $(NaS)_2PSS_{1/2}$ units were corner shared to form $Na_4P_2S_7$ dimers and confirmed their high structural stability. For y = 0.6, Na_3PS_4 phase formed because of non-bridging sulfur which were terminated by Na^+ ions.

Noi *et al.* **[42]** prepared the glass compositions $x$$Na_2S$+(100-$x$)$P_2S_5$ (x = 67, 70, 75 and 80 mol%) by mechanochemical method and examined their local structure changes, electrical conductivity and thermal behavior. Raman and NMR spectroscopic studies confirmed the presence of thiophosphate units in all compositions. The room temperature ionic conductivity increases with an increase of Na_2S content and achieved a maximum value 1×10^{-5} Scm^{-1} at x =

80. In addition to this, they prepared the glass-ceramics by heating the glasses above their crystallization temperatures. The relationship between crystalline phase and ionic conductivity was investigated for the prepared glass-ceramics. For x = 70 and 75, glass-ceramics showed maximum ionic conductivities than those of other glasses. High ionic conductivity in these glass-ceramics attributed due to the precipitation of Na_3PS_4 phase having cubic crystal structure. Especially, for x = 75 glass-ceramic, highest conductivity ~ 2×10^{-4} S cm^{-1} and lowest activation energy ~ 27 kJ mol^{-1} was observed at ambient temperature.

To improve the ionic conductivity and physical properties of the binary sulfide glassy solid electrolytes, mixed glass formers effect (MGFE) on structure and thermal stability are checked in detail. Some of the MGFE for sodium and lithium sulfide based glasses are discussed as follows:

Bischoff *et al.* **[111]** studied the MGFE on densities and T_g in the glass $0.5Na_2S+0.5[xGeS_2+(1-x)PS_{5/2}]$ system. All ternary compositions showed depression in the T_g relative to the theoretical linear interpolation behavior. The maximum deviation was observed at x = 0.3 from theoretical linear behavior. The T_g of the x = 0 sodium thiophosphate glass is significantly lower than that of the x = 1 sodium thiogermanate glass. This phenomenon happened because sodium thiogermanate glass exhibits two bridging sulfurs and sodium thiophosphate glass contains one bridging-sulfur per network former (Ge). However, a decrease in T_g arises because of reduction in the network connectivity. The densities of the above compositions do not deviate considerably from linear interpolation behavior except for x = 0.2 glass. The electrical conductivity and structural changes were also investigated for the same compositions by Bischoff *et al.* **[112].** A nonlinear composition-dependent change in the ionic conductivity is observed when one glass former ($PS_{5/2}$) is replaced by another glass former (GeS_2) at constant Na_2S concentrations. Due to MGFE, structural changes in the glasses were studied by FTIR,

Raman and NMR spectroscopy. In all compositions, phosphorus groups are connected with a large number of Na^+, while germanium groups are associated with less number of Na^+. In addition to this, they developed a structural model based on short range order (SRO) structures and concluded the fractions of all non-bridging sulfur (NBS) and bridging sulfur (BS) structures in the glass that can be used to study the glass transition. This model can also used to calculate the fractions of all SRO groups which contain charge compensating Na^+.

Kowada *et al.* **[113]** investigated the electronic states using DV-Xα cluster method in the Li_2S-SiS_2-P_2S_5 and Li_2S-SiS_2-Al_2S_3 glass systems. In these glasses, differential total bond overlap population (DBOP) showed positive correlations with activation energies and negative correlations with ionic conductivities which were in well agreement with experimental measurements. They concluded that a smaller change in the DBOP causes fast-ion movement in the lithium sulfide glasses. More MGFE on structure and ionic conductivity in the sodium and lithium-sulfide based glasses are investigated in detail using different modifiers **[114-116].**

It is observed from above study that sulfide based glasses are better ion conductors than oxide glasses of similar compositions. However, sulfide based glasses shows poor stability in water and air. The sulfide glass electrolytes can easily react with ambient moisture and generate H_2S gas **[117].** Therefore, handling of sulfide solid electrolytes must be done in an inert atmosphere. However, partial substitution of oxygen atoms for sulfur atoms in sulfide electrolytes can be effective in suppressing H_2S gas generation **[118, 119].** Recently, Hayashi *et al.* **[120]** reported a composite electrolyte with 90 mol% of $75Li_2S{\cdot}21P_2S_5{\cdot}4P_2O_5$ glass and 10 mol% ZnO via mechanical milling. In this work, partial substitution of P_2O_5 for P_2S_5, as well as the addition of ZnO, decreased the rate of H_2S generation when exposed to air.

Minami *et al.* **[121]** prepared the oxysulfide glass compositions $70Li_2S.(30\text{-}x)P_2S_5.xP_2O_5$; ($0 \leq x \leq 10$ mol%) by melt-quench method and converted them into glass-ceramics after heating them

above their crystallization temperatures and studied their structural and electrical properties. By substituting P_2O_5 for P_2S_5 in the glass-ceramics showed signature of oxysulfide units that was confirmed by NMR. The prepared glass-ceramic with 3 mol% of P_2O_5 provided highest ionic conductivity i.e. 3×10^{-3} Scm^{-1} and lowest activation energy (16 $kJmol^{-1}$) at room temperature. It was concluded that the substitution of P_2S_5 by P_2O_5 in the $Li_2S–P_2S_5$ based glass–ceramics can increase ionic conductivity efficiently.

In addition to ionic conductivity for solid electrolyte, elastic modulus is also very important factor to improve their overall efficiency. While charging and discharging of Na-ion batteries, it is observed that electrodes expand and contract. Consequently, the volume of active electrode material changes easily. The change in volume leads to crack in electrode particles, which is the main cause of loss in capacity of batteries **[122].** Thus, a high ionic conductivity and good fractural strength are required to achieve better performance of solid electrolytes. The solid electrolyte should have moderate elastic modulus for improving the energy density and cycle performance of the Na-ion batteries.

Sakuda *et al.* **[123]** prepared the $x$$Na_2S$-(1-$x$)$P_2S_5$ and $x$$Li_2S$-(1-$x$)$P_2S_5$; ($30 \leq x \leq 80$) glasses by mechanochemical method and investigated their Young's modulus. The shear and longitudinal wave velocities were evaluated at room temperature using ultrasonic pulse transmission technique and these velocities were further used for calculation of Young's modulus. The Young's modulus increases with increasing Na_2S and Li_2S content. The Young's modulus of the as prepared glasses were observed in the range of (18–25 GPa) and concluded that it is an appropriate range as solid electrolyte for batteries applications. On the other hand, Nose *et al.* **[124]** prepared the $x$$Na_2S$-(1-$x$)$P_2S_5$; ($50 \leq x \leq 75$) glass system. They have also evaluated Young's modulus which was in the range of (15–19 GPa).

Recently Kato *et al.* **[125]** evaluated the Young's modulus for $70Li_2S$-$(30-x)P_2S_5$-xP_2O_5; (x = 0, 3 and 10 mol%) oxysulfide glass system. They also used ultrasonic pulse echo method to calculate the Young's modulus. They observed that Young's moduli increases with replacement of P_2S_5 by P_2O_5. They reported the Young's modulus in range of (22-27 GPa) for the prepared glasses. The highest Young's modulus 27 GPa was observed for the 10 mol% P_2O_5 containing glass.

2.1. GAPS IN THE STUDY

Based on the literature, it is concluded that addition of the oxides in the sodium-sulfide based glasses to suppress the H_2S generation and to increase the stability has not been studied in detail and systematically. As discussed above that addition of CuO in the sulfide glasses can increase the electrical conductivity and chemical stability dramatically. Additionally, the work on addition of CuO/CuS in the sodium-sulfide based glasses has not been studied extensively. The structural, thermal and electrical properties for the binary Na_2O-P_2O_5 system are investigated in detail. However, glass-ceramics of Na_2O-P_2O_5 system is not examined in detail. It is also observed from the above study that mixed glass formers in either oxide or in sulfide based glasses, enhances the ionic conductivity and thermal stability. However, limited work on mixed glass modifiers effect (MGME) on thermal stability and crystallization kinetics in the sodium-phosphate glasses has been carried out. Based on the above gaps, the objectives of the present study are as follows:

2.2. OBJECTIVES

1. To synthesize sodium-phosphate glasses modified with (Li_2O/K_2O/CuS).
2. To characterize the glasses by X-ray diffraction, FTIR, SEM, DTA/TG and Dilatometery for their physical, structural and thermal properties.
3. To investigate the glasses/glass-ceramics for their ionic conductivity.

REFERENCES:

[1] E. Warburg, "Sodium ion migration through glasses," Wiedmann Ann. Phys. **21,** (1884) 622.

[2] G.W. Morey," Properties of glass. Reinhold, New York (1954).

[3] A.E. Owen, "Progress in Ceramic Science, Pergamon press, **3,** (1963) 78.

[4] E. Robinel, B. Carette, M. Ribes, J. Non-Cryst. Solids, **57,** (1983) 49.

[5] T. Minami, J. Non-Cryst. Solids, **56,** (1983) 15.

[6] J.P. Malugani, R. Mercier, B. Fahys, G. Rober, J. Solid State Chem. **45,** (1982) 309.

[7] A. Dalvi, K. Shahi, J. Non-Cryst. Solids, **341,** (2004) 124.

[8] K.M. Shaju, S. Chandrd, Solid State Ionics, **86/88,** (1996) 453.

[9] J.M. Reau, B. Tanguy, J.J. Videau, J. Portier, P. Hagenmuller, Solid State Ionics, **28/30,** (1988) 792.

[10] G. Govindaraj, N. Baskaran, Mat. Sci. Eng. B, **25,** (1994) 135.

[11] C. Liu, H.G.K. Sundar, C.A. Angell, Solid State Ionics, **18/19,** (1986) 442.

[12] C. Liu, H.G.K. Sundar, Solid State Ionics, **13,** (1984) 105.

[13] N. Machida, Y. Shinkuma, T. Minami, J. Ceram. Soc. Japan, **97,** (1989) 1104.

[14] L.G. Yuan, 6^{th} Int. conf. on Solid State Ionics, Garmisch, Partenkirchen, Germany (1987).

[15] V.G. Chandrasekhar, S.A. Suthanthiraraj, Bull. Electrochem., **9,** (1993) 316.

[16] K.S. Sidhu, S. Singh, S.S. Sekon, Phys. Chem. Glasses, **32,** (1991) 1.

[17] N. Machida, Y. Matsuda, T. Shigematsu, T. Minami, Solid State Ionics, **73,** (1994) 63.

[18] A. Chandra, A. Bhatt, A. Chandra, J. Mater. Sci. Technol., **29,** (2013) 193-208.

[19] B.V.R. Chowdari, K. Radhakrishnan, J. Non-Cryst. Solids, **108,** (1989) 323.

[20] J.L. Souquet, E. Robinel, B. Barrau, M. Ribes, Solid State Ionics, **3/4,** (1981) 317.

[21] R. Mercier, J.P. Malugani, B. Fahys, G. Robert, Solid State Ionics, **5,** (1981) 663.

[22] A. Pradel, M. Ribes, Solid State Ionics, **18/19,** (1986) 351.

[23] K. Hirai, M. Tatsumisago, T. Minami, Solid State Ionics, **78,** (1995) 269.

[24] N. Aotani, K. Iwamoto, K. Takada, S. Kondo, Solid State Ionics, **68,** (1994) 35.

[25] F. Mizuno, T. Ohtomo, A. Hayashi, K. Tadanaga, T. Minami, M. Tatsumisago, J. Ceram. Soc. Japan, **112,** (2004) S709.

[26] Y. Yoneda, N. Machida, T. Shigematsu, Proc. 15th Symposium on the Ceramic Society of Japan, (2002) 220.

[27] A. Leavasseur, R. Olazcuaga, M. Kbala, M. Zahi, P. Hagenmuller, C.R. Acad. Sci. Paris, **293,** (1981) 563.

[28] Z. Zhang, J.H. Kennedy, Solid State Ionics, **38,** (1990) 217.

[29] H. Wada, M. Menetrier, A. Levasseur, P. Hagenmuller, Mater. Res. Bull., **18,** (1983) 189.

[30] J.P. Malugani, G. Robert, Mater. Res. Bull., **14,** (1979) 1075.

[31] J.P. Malugani, G. Robert, Solid State Ionics, **1,** (1980) 519.

[32] J.E. Saienga, Optimization of fast ionic conducting glasses for lithium batteries, Ph.D dissertation, Iowa State University Ames, Iowa (2005).

[33] J. Kennedy, Y. Yang, J. Solid State Chem., **69,** (1987) 252.

[34] A. Carette, E. Robinel, M. Ribes, Glass Tech., **24,** (1983) 157.

[35] T.D. Tho, Ion conduction mechanisms in fast ion conducting oxide glasses for rechargeable batteries, Ph.D dissertation, Department of Materials Science & Engineering, National University of Singapore (2011).

[36] S. Ujiie, A. Hayashi, M. Tatsumisago, Mater Renew Sustain Energy, **3,** (2014) 18.

[37] C. Lim, D.E. Day, J. Am. Ceram. Soc., **61,** (1978) 99.

[38] A.R. Kulkarni, H.S. Maiti, A. Paul, Bull. Mat. Sci., **6,** (1984) 201.

[39] J.P. Malugani, G. Robert, R. Merier, Mat. Res. Bull., **15,** (1980) 715.

[40] M. Ribes, B. Barrau, J.L. Souquet, J. Non-Cryst. Solids, **38/39, (**1980) 271.

[41] S.S. Das, V. Srivastava, P. Singh, Indian J. Eng. Mat. Sci., **13,** (2006) 455.

[42] K. Noi, A. Hayashi, M. Tatsumisago, J. Power Sources, **269,** (2014) 260.

[43] A. Hayashi, K. Noi, A. Sakuda, M. Tatsumisago, Nature Commun., **3,** (2012) 856.

[44] Y.K. Startsev, A.A. Pronkin, I.A. Sokolov, I.V. Murin, Glass Phys. Chem., **37,** (2011) 263.

[45] N. Tanibata, K. Noi, A. Hayashi, M. Tatsumisago, RSC Adv., **4,** (2014) 17120.

[46] D. Larink, H. Eckert, S.W. Martin, J. Phys. Chem. C, **116, (**2012) 22698.

[47] K.K. Evstrop'ev, G.T. Petrovskii, W.D. Chalilev, C.R. Trav. Congr. Int. Verre, 9th (1971) 485.

[48] M. Doreau, A.A.E. Anouar, G. Robert, Mater. Res. Bull., **15,** (1980) 285.

[49] M. Tatsumisago, Y. Kowada, T. Minami, Phys. Chem. Glasses, **29,** (1988) 63.

[50] K. Tanaka, T. Yoko, H. Yamada, K. Kamiya, J. Non-Cryst. Solids, **103,** (1988) 250.

[51] K. Tanaka, T. Yoko, K. Kamiya, H. Yamada, S. Sakka, J. Non-Cryst. Solids, **135,** (1991) 211.

[52] D. Kunze, Fast Ion Transport in Solids, in: W. Van Gool (Ed.), North Holland, Amsterdam, (1973) 495.

[53] J.E. Shelby, R.L. Ortolana, Phys. Chem. Glasses, **31,** (1990) 25.

[54] F.A. Fusco, H.L. Tuller, D.P. Button, Mater. Sci. Eng. B, **13,** (1992) 157.

[55] T. Minami, Materials for Solid State Batteries, in: B.V.R. Chowdari, S. Radhakrishna (Eds.), World Scientific, Singapore, (1986) 169.

[56] M. Ribes, B. Barrau, J.L. Souquet, J. Non-Cryst. Solids, **38/39,** (1980) 103.

[57] G. Band, J.P. Besse, J. Am. Ceram. Soc., **64,** (1981) 242.

[58] H. AlRihabi, J.L. Souquet, Acad. Sci., Ser. C, **288,** (1979) 549.

[59] D. Ravaine, J. Non-Cryst. Solids, **38/39,** (1980) 353.

[60] R.F. Bartolomew, J. Non-Cryst. Solids, **12,** (1973) 321.

[61] H. Namikawa, J. Non-Cryst. Solids, **18,** (1975) 173.

[62] Y.M. Moustafa, K.E. Egili, J. Non-Cryst. Solids, **240,** (1998) 144.

[63] R.K. Brow, R.J. Kirkpatrick, G.L. Turner, J. Non-Cryst. Solids, **116,** (1990) 39.

[64] B.K. Money, K. Hariharan, J. Phys.: Condens. Matter, **21,** (2009) 115102 (10pp)

[65] A. Purwanto, T. Kamiyama, A. Hoshikawa, S. Harjo, E. Kartini, M.F. Collins, T. Sakuma, J. Neutron Res., **13,** (2005) 169.

[66] A.M. Glass, K. Nassau, T.J. Negran, J. Appl. Phys., **49,** (1978) 4808.

[67] I.A. Sokolov, I.V. Murin, V.E. Kriyt, A.A. Pronkin, Glass Phys. Chem., **37,** (2011) 351.

[68] M. Ganguli, M.H. Bhat, K.J. Rao, Solid State Ionics, **122,** (1999) 23.

[69] S. Rani, S. Sanghi, A. Agarwal, V.P. Seth, Spectrochim. Acta Part A, **74,** (2009) 673.

[70] S. Sanghi, S. Rani, A. Agarwal, V.P. Seth, Physica B, **404,** (2009) 1969.

[71] L. Montagne, G. Palavit, G. Mairesse, Phys. Chem. Glasses, **37,** (1996) 206.

[72] M.D. Thombre, Indian J. Appl. Res., **4,** (2014), 469.

[73] D. Carta, D. Qiu, P. Guerry, I. Ahmed, E.A.A. Neel, J.C. Knowles, M.E. Smith, R.J. Newport, J. Non-Cryst. Solids, **354,** (2008) 3671.

[74] D. Qiua, P. Guerry, I. Ahmed, D.M. Pickup, D. Carta, J.C. Knowles, M.E. Smith, R.J. Newport, Mater. Chem. Phys., **111,** (2008) 455.

[75] P.Y. Shih, S.W. Yung, T.S. Chin, J. Non-Cryst. Solids, **244,** (1999) 211.

[76] M. Mirzayi, M.H. Hekmatshoar, Ionics, **15,** (2009) 121.

[77] S. Aqdim, M. Ouchetto, Adv. Mater. Phys. Chem., **3,** (2013) 332.

[78] X. Fang, C.S. Ray, G.K. Marasinghe, D.E. Day, J. Non-Cryst. Solids, **263/264,** (2000) 293.

[79] A. Faivre, D. Viviani, J. Phalippou, Solid State Ionics, **176,** (2005) 325.

[80] R.K. Brow, J. Am. Ceram. Soc., **76,** (1993) 913.

[81] L. Abbas, L. Bih, A. Nadiri, Y.E. Amraoui, D. Mezzane, B. Elouadi, J. Mol. Struct., **876,** (2008) 194.

[82] G.N. Greaves, Philos. Mag. B, **60,** (1989) 793

[83] A. Bunde, M.D. Ingram, P. Maass, K.L. Ngai, J. Phys. A, **24,** (1991) 2881.

[84] P. Maass, A. Bunde, M.D. Ingram, Phys. Rev. Lett., **68,** (1992) 3064.

[85] A.M. Milankovic, B. Santic, D.E. Day, C.S. Ray, J. Non-Cryst. Solids, **283,** (2001) 119.

[86] M.A. Samee, S.K. Ahmmad, S.M.D. Taqiullah, A. Edukondalu , S. Bale, S. Rahman, Int. J. Modern Phys.: Conference series, **22,** (2013) 261.

[87] V.K. Deshpande, A. Pradel, M. Ribes, Mat. Res. Bull., **23,** (1988) 379.

[88] T. Tsuchiya, T. Moriya, J. Non-Cryst. Solids, **38/39,** (1980) 323.

[89] P.S. Anantha, K. Hariharan, Mater. Chem. Phys., **89,** (2005) 428.

[90] D. Zielniok, C. Cramer, H. Eckert, Chem. Mater., **19,** (2007) 3162.

[91] A. Pradel, C. Rau, D. Bittencourt, P. Armand, E. Philippot, M. Ribes, Chem. Mater., **10,** (1998) 2162.

[92] L.F. Maia, A.C.M. Rodrigues, Solid State Ionics, **168,** (2004) 87.

[93] P. Kluvanek, R. Klement, M. Karacon, J. Non-Cryst. Solids, **353,** (2007) 2004.

[94] R. Christensen, G. Olson, S.W. Martin, J. Phys. Chem. B, **117,** (2013) 2169.

[95] R. Christensen, G. Olson, S.W. Martin, J. Phys. Chem. B, **117,** (2013) 16577.

[96] R. Christensen, J. Byer, G. Olson, S.W. Martin, J. Non-Cryst. Solids, **358,** (2012) 826.

[97] R. Christensen, J. Byer, G. Olson, S.W. Martin, J. Non-Cryst Solids, **358,** (2012) 583.

[98] D.L. Messurier, V. Petkov, S.W. Martin, Y. Kim, Y. Ren, J. Non-Cryst. Solids, **355,** (2009) 430.

[99] B. Barrau, M. Ribes, M. Maurin, J. Non-Cryst. Solids, **37,** (1980) 1.

[100] K. Minami, F. Mizuno, A. Hayashi, M. Tatsumisago, Solid State Ionics, **178,** (2007) 837.

[101] M. Tatsumisago, S. Hama, A. Hayashi, H. Morimoto, T. Minami, Solid State Ionics, **154/155,** (2002) 635.

[102] M. Tatsumisago, A. Hayashi, Solid State Ionics, **225,** (2012) 342.

[103] F. Mizuno, A. Hayashi, K. Tadanaga, M. Tatsumisago, Solid State Ionics, **225,** (2006) 2721.

[104] A. Hayashi, T. Ohtomo, F. Mizuno, K. Tadanaga, M. Tatsumisago, Electrochimica Acta, **50,** (2004) 893.

[105] F. Mizuno, A. Hayashi, K. Tadanaga, M. Tatsumisago, Adv. Mater., **17,** (2005) 918.

[106] M. Tatsumisago, A. Hayashi, J. Non-Cryst. Solids, **354,** (2008) 1411.

[107] M. Tatsumisago, A. Hayashi, Functional Materials Letters, **1,** (2008) 31.

[108] A. Hayashi, K. Minami, M. Tatsumisago, J. Non-Cryst. Solids, **355,** (2009) 1919.

[109] S.S. Berbano, I. Seo, C.M. Bischoff, K.E. Schuller, S.W. Martin, J. Non-Cryst. Solids, **358,** (2012) 93.

[110] C. Bischoff, K. Schuller, M. Haynes, S.W. Martin, J. Non-Cryst. Solids, **358,** (2012) 3216.

[111] C. Bischoff, K. Schuller, S.W. Martin, J. Phys. Chem. B, **118,** (2014) 3710.

[112] C. Bischoff, K. Schuller, N. Dunlap, S.W. Martin, J. Phys. Chem. B, **118,** (2014) 1943.

[113] Y. Kowada, M. Tatsumisago, T. Minami, H. Adachi, J. Non-Cryst. Solids, **354,** (2008) 360.

[114] S.W. Martin, C. Bischoff, K. Schuller, J. Phys. Chem. B, **119,** (2015) 15738.

[115] K. Minami, A. Hayashi, S. Ujiie, M. Tatsumisago, J. Power Sources, **189,** (2009) 651.

[116] K. Minami, A. Hayashi, S. Ujiie, M. Tatsumisago, Solid State Ionics, **192,** (2011) 122.

[117] H. Muramatsu, A. Hayashi, T. Ohtomo, S. Hama, M. Tatsumisago, Solid State Ionics, **182,** (2011) 116.

[118] T. Ohtomo, A. Hayashi, M. Tatsumisago, K. Kawamoto, J. Non-Cryst. Solids, **364,** (2013) 57.

[119] T. Ohtomo, A. Hayashi, M. Tatsumisago, K. Kawamoto, J Mat. Sci, **48**, (2013) 4137.

[120] A. Hayashi, H. Muramatsu, T. Ohtomo, S. Hama, M. Tatsumisago, J. Alloy. Compd., **591,** (2014) 247.

[121] K. Minami, F. Mizuno, A. Hayashi, M. Tatsumisago, J. Non-Cryst. Solids, **354,** (2008) 370.

[122] M. Nagao, A. Hayashi, M. Tatsumisago, Electrochim. Acta, **56,** (2011) 6055.

[123] A. Sakuda, A. Hayashi, M. Tatsumisago, Sci. Rep., **3,** (2013) 2261.

[124] M. Nose, A. Kato, A. Sakuda, A. Hayashi, M. Tatsumisago, J. Mater. Chem. A, **3,** (2015) 22061.

[125] A. Kato, M. Nagao, A. Sakuda, A. Hayashi, M. Tatsumisago, J. Ceram. Soc. Japan, **122,** (2014) 552.

Chapter-3
(Experimental procedure)

- **Sample preparations**
- **Structural techniques (XRD, FTIR, Raman and SEM)**
- **Thermal techniques (DTA and Dilatometer)**
- **Mechanical and electrical techniques (Vickers micro-hardness, Elastic constant measurements and Impedance analyzer)**

Chapter-3 Experimental procedure

3.1. Raw materials

In the present study, the glasses were synthesized using raw chemicals, sodium sulfide nonahydrate $Na_2S.9H_2O$ (Sigma Aldrich, 99.9%), phosphorus pentasulfide P_2S_5 (Sigma Aldrich, 99%), sodium carbonate Na_2CO_3 (Sigma Aldrich, 99.99%), phosphorus pentaoxide P_2O_5 (Sigma Aldrich, 99.99%), lithium carbonate Li_2CO_3 (Sigma Aldrich, 99%), potassium carbonate K_2CO_3 (Sigma Aldrich, 99%), benzene C_6H_6 (Sigma Aldrich, ≥ 99.9%) and copper sulfide CuS (Sigma Aldrich, 99.99%). All chemicals were used as such without any further purification.

3.2. Sample preparation

Glass samples were prepared via conventional melt-quench technique. Each batch was prepared by taking required amount of chemicals as per their stoichiometry ratio. Appropriate amounts of chemicals were ground using agate mortar and pestle in benzene medium. Broadly sodium-phosphate sulfide and sodium-phosphate oxide glasses are chosen for the present study. All the samples with their label and composition are given in the table 3.1.

For sulfide series, mixtures of powders were transferred to graphite crucible and melted at 700 °C under flowing argon atmosphere at a heating rate of 5° min^{-1}. On the other hand, for oxide series, mixtures of powders were melted at 1000 °C in graphite crucible at a heating rate of 5° min^{-1} in air. After holding the molten masses at their respective temperatures for 20 min, it was splat-quench by copper plates. Thereafter, sodium oxide glass series were ground in agate mortar for 30 min and cold pressed after applying 12 $kNcm^{-2}$ pressures for 2 min to get pellets of diameter 15 mm and thickness 2 mm. The as prepared pellets were heat treated at 50 °C above their first crystallization temperatures (evaluated from DTA) at the heating rate of 2º min^{-1} in silicon carbide tubular furnace.

Table 3.1: Sample label with their initial glass compositions in mol%.

Sulfide series			
Sample label	**P_2S_5**	**Na_2S**	**CuS**
N1	65	35	---
N2	60	40	---
N3	55	45	---
N4	50	50	---
N5	45	55	---
N6	40	60	---
NC5	45	50	5
NC10	45	45	10

Oxide series				
Sample label	**P_2O_5**	**Na_2O**	**Li_2O**	**K_2O**
NP1	60	40	---	---
NP2	55	45	---	---
NP3	50	50	---	---
NP4	45	55	---	---
NL5	55	40	5	---
NL10	55	35	10	---
NL15	55	30	15	---
NL20	55	25	20	---
NL25	55	20	25	---
NK5	55	40	---	5
NK10	55	35	---	10
NK15	55	30	---	15
NK20	55	25	---	20
NK25	55	20	---	25

To ensure that the glasses get converted into glass-ceramics, all the pellets were held for 4h at their heat treatment temperature followed by room temperature furnace cooling. The obtained glass-ceramics of 40, 45, 50 and 55 mol% Na_2O are labeled as NP1, NP2, NP3 and NP4, respectively.

3.3. CHARACTERIZATION TECHNIQUES

The as quenched and heat treated samples were characterized by various techniques to check their phase stability, thermal stability, structural changes and electrical conductivity. The details of these techniques are as follows:

3.3.1. Density measurement

Archimedes principle was used to measure the density of the quenched samples using microbalance having least count (0.01 mg). Xylene was used as an immersion liquid at room temperature. The well known equation, used for density calculation, is given below:

$$\rho_{Sample} = \frac{w_a}{w_a - w_x}\rho_x \qquad (3.1)$$

where ρ_{Sample} stand for density of sample, w_a is the weight of sample in air, w_x is the weight of sample in xylene and ρ_x is the standard density of xylene (ρ= 0.863 gcm^{-3}). The tabulated density values are the average of at least four independently measured values. Moreover, the molar volume of the synthesized samples was also calculated with the help of following equation:

$$V_M = \frac{M}{\rho} \qquad (3.2)$$

where V_M is the molar volume, ρ is the density and M is the molar mass of the sample.

3.3.2. X-ray diffraction (XRD)

X-ray diffraction is a non-destructive technique and being used for detailed quantitative and qualitative information about the amorphous and crystalline structure of all the materials. XRD is also used to identify the crystallite size, inter-atomic distances, lattice strain and lattice parameters of a crystalline solid. X-rays are produced by bombarding a target material (Mo, Cu Co, Cr) with a beam of high energetic electrons emitted from hot tungsten filament. The incident beam ejects the K-shell electrons from the metal target and in result the resultant vacancy is filled by the electrons jumping from higher energy shell to the lower (inner) shell. During this process, the emission of X-ray photon also called as characteristic energy occurs depending on the target material. These X-rays were used to analyze the prepared samples. The experiment was performed to confirm the structural nature of the samples. The amorphous nature of the synthesized samples was confirmed by X-ray diffraction (PANalytical X'Pert PRO) using CuKα radiation of wavelength 1.541 Å with Ni-filter at room temperature. During measurement, voltage, current and scan speed were selected as 40 kV, 45 mA and 0.013° min^{-1}, respectively. Continuous XRD patterns were recorded from 10 to 80º for all the samples. Moreover, the calculation of volume fraction and indexing of crystalline peaks were done with the help of X-Pert High Score Plus software.

3.3.3. Differential thermal analysis (DTA)

DTA is a thermo analytical technique which measures the temperature difference between the sample and the inert reference sample as a function of time during heating or cooling in known environment **[1].** Changes in the samples can be either endothermic or exothermic. Thus, a DTA curve provides the information about glass transition, crystallization and melting temperature of the samples as well as the phase transitions in the crystalline samples. To know about these information, DTA was done using Perkin Elmer (Model: Diamond Pyris) equipment. The DTA equipment was calibrated for temperature as explained by Krishnan et al. **[2],** where the accuracy of temperature measurement was ±1 ºC. High purity (99.9 %) alumina powder was used as an inert reference material. The experiments were performed under Argon atmosphere with flow rate of 180 ml min^{-1} for all the samples. For crystallization kinetics study, all the experiments were performed at different heating rates in different temperature range using 8 mg (± 3 μg) of glass powder in a Pt crucible.

3.3.4. Dilatometeric measurement

Thermal dilatometric analysis (TDA) generally termed as "dilatometry", which measures the volume changes in the materials (glasses, ceramics, composites, metals and others) as a function of time/temperature. This measurement gives the information about changes in length (shrinkage/expansion) of the solid materials with respect to temperature. The dilatometer is used to determine softening temperature, glass transition temperature, thermal expansion coefficient (TEC), phase transition, Curie point and stress relaxation **[3].**

If a temperature changes from T_0 to T, it causes expansion in the sample of initial length (L_0) then α_l can be calculated as follows:

$$\alpha_l = \frac{1}{L_0}\left(\frac{\Delta L}{\Delta T}\right) \quad (3.3)$$

where, α_l stands for coefficient of linear thermal expansion, $\Delta l/\Delta T$ stands for change in length with respect to temperature. TEC depends upon the attractive and repulsive forces between the atoms. With increase in temperature, the energy of the system increases and the atoms vibrate about their mean position. The repulsive forces between the atoms increase more rapidly than attractive ones. Thus, at a particular energy (i.e. temperature) the atoms can move far apart more rapidly than they are pushed together. Strongly bonded atoms expand at lower rates with temperature than weak bonded materials. To estimate the softening temperature, glass transition temperature and thermal expansion coefficient (TEC) of all glasses, dilatometer measurements was done using NETZSCH (model DIL 402C, Germany) dilatometer. Smooth and polished surfaces samples were used for the measurement. For sulfide series, the temperature was selected in the range (room temperature to 260 ºC), while for oxide series, temperature range was from room temperature to 450 ºC. During all experiments the heating rate was 5º min^{-1}.

3.3.5. Fourier transform infrared spectroscopy (FTIR)

Infrared spectroscopy is a most common techniques used to characterize inorganic and organic materials. It is a study of the interactions between matter and electromagnetic field in the IR region. The molecules of the samples excite in the infra-red region after absorbing IR radiation. This absorption creates a molecular finger print of the sample. Thus, in the FTIR spectra the peaks appear, which correspond to frequency of a vibration of sample molecules. To observe infrared absorptions for a molecule, it must have an electric dipole moment of the molecule and must change during the vibration **[4].** FTIR spectra were collected at room temperature using Agilent (Model No. Carry-600) FTIR spectrometer and spectral resolution was ±1 cm^{-1}. Mid-IR spectra were recorded using KBr beam splitter in the range of (2000–400) cm^{-1}. Two milligrams of each glass sample were ground with 100 mg of KBr into a fine powder and pressed after applying 14 $kNcm^{-2}$ pressures for 5 min to get pellets for IR study.

3.3.6. Raman spectroscopy

It is a spectroscopic technique used to observe the rotational, vibrational and other low-frequency modes in the samples **[5].** However, Raman spectroscopy is generally used to observe vibrational modes, which gives the information about the symmetry of molecules and chemical bonds. Raman scattering is based on an inelastic scattering of the monochromatic light, because during interaction, energy transfers in between sample molecules and phonon. Raman bands shifts either of lower energy or higher energy that depends upon vibrational state of the molecule. The difference in the energy provides the information about the phonon modes in the samples. The changes in phosphate structural units in all glasses were examined by Raman spectroscopy. The data were collected using Renishaw in Via Raman spectrometer. For data collection 514.5 nm line of Ar^+ laser alongwith 20 mW power was used. The calibration was done with the help of silicon as a reference at 520 cm^{-1} within ±1 cm^{-1}. For Raman spectra, the powder sample was loaded in a plastic sample holder and surface was made smooth by compressing the powder. At different locations, all spectra were taken to check the homogeneity in the glasses.

3.3.7. Gas chromatography

It is a general type of chromatography used for analyzing the compounds which can be vaporized without decomposition. For a comparative study, determination of H_2S generation from sulfide samples was carried out by gas chromatography (NUCON-5765). This chromatograph is equipped with thermal conductivity detector (TCD) and 13A molecular sieve (size: 2m × 6.35mm) steel column. During experimentation the oven temperature was 60 ºC while the temperature of injector and detector was 70 ºC and 120 ºC, respectively. Moreover, N_2 (99.999 %) was used as a carrier gas flushed at a rate of 30 ml min^{-1}. The amount of H_2S gas generated from 400 mg of powder sample was measured. For it, weighted quantity of glass

powder (400 mg) was taken into 20 ml capacity quartz tube. The sample containing tube was exposed to the air for 10 min and then tube was closed and sealed with Teflon tape. From it, 1 ml of gas was taken out at different time intervals (10, 20 and 30 min) for gas chromatography. The data so obtained in gas chromatography study was converted to real value with the help of calibrated value. During measurement, the temperature and relative humidity were 16 ºC and 30 %, respectively.

3.3.8. Scanning electron microscopy (SEM)

SEM is an important tool to study the microstructural and morphological features of the samples. From scanning electron microscope, high magnification (~10^6 X) can be obtained consequently; larger area can be focused at one time. By using high-energy beam of electrons, generated by lanthanum hexaboride (LaB_6) or tungsten (W) filament, information about the surface topography, morphology and compositions of the samples are obtained. During SEM measurements, different types of signals are produced which includes back scattered electrons (BSE), secondary electrons (SE), cathodeluminescence, auger electrons (AE) and characteristic X-rays. To detect these signals, different detectors are located in the machine at different places. The microstructure of the fractured surfaces of glass-ceramic sample was observed under SEM (JEOL, JSM-6510LV). Before observation, all the glass ceramic samples were gold sputtered by sputter coating unit (JEOL-JFC 1600, Auto Fine Coater).

3.3.9. Vickers micro-hardness

The micro-hardness of the glass-ceramic was measured using Vickers indenter (square-based pyramidal diamond) micro-hardness tester (Mitutoyo, Model No. MVK-H0) with a 136º angle between opposite faces of the indenter. The glass-ceramic surfaces were dry ground using 400 grit SiC emery paper, to obtain smooth and parallel surfaces. A load of 0.9 N was applied to prepared samples for 10 seconds. A minimum of 10 indentations was performed on each

sample. The measurements were carried out under normal atmospheric conditions. The Vickers hardness was (H_v) calculated from the standard Vickers formula **[6]:**

$$H_v = 0.1854 \frac{p}{d^2} \quad (3.4)$$

where, p is the indentation load in *kgf* and d is the diagonal length of the Vickers indentation in mm.

3.3.10. Elastic constant measurements

The shear and longitudinal wave velocity measurements were done using ultrasonic pulse transmission technique. The disk-shaped glass ceramic samples with 15 mm diameter and 2 mm thickness were well polished to have parallel and smooth surfaces. Pulses generated by the pulse oscillator were subjected to the transmitting transducer, which converts them into acoustic pulses. These acoustic pulses propagating through the test sample were converted into electrical signals by the receiving transducer. The amplified output signal from the sample was then viewed on an oscilloscope. The ultrasonic pulses generated having 1*MHz* PZT (lead zirconate titanate) transducers from samples were detected by X and Y cut for longitudinal and shear waves, respectively. Before experimentation, the sample was well bonded with transducer using Nonaq stopcock grease as an acoustic medium. For ultrasonic wave velocities, a transducer correction was also done. The transmit time of the ultra sound was measured using a 100 *MHz* digital storage oscilloscope (Tektronix model: 2221) up to an accuracy of 1 μs.

The elastic constants were calculated with the help of longitudinal velocity and shear velocity using following equations **[7]**

Longitudinal modulus*:* $L = \rho V_l^2$ (3.5)

Shear modulus: $G = \rho V_s^2$ (3.6)

Bulk modulus: $K = \rho(V_L^2 - \frac{4}{3}V_s^2)$ (3.7)

$$\text{Young's modulus: } E = \frac{\rho V_S^2 (3V_L^2 - 4V_S^2)}{V_L^2 - V_S^2} \quad (3.8)$$

$$\text{Poisson's ratio: } V = \frac{(V_L^2 - 2V_S^2)}{2(V_L^2 - V_S^2)} \quad (3.9)$$

where, ρ correspond to density, V_L to longitudinal velocity and V_S to shear velocity of the sample.

3.3.11. Electrical conductivity

Impedance spectroscopy is a powerful technique for characterizing the electrical properties of the materials and their interfaces with electronically conducting electrodes. The impedance spectroscopy measurement is based on impedance (Z) and admittance (Y) over a range of temperatures and frequencies and analyzing them in complex impedance plane.

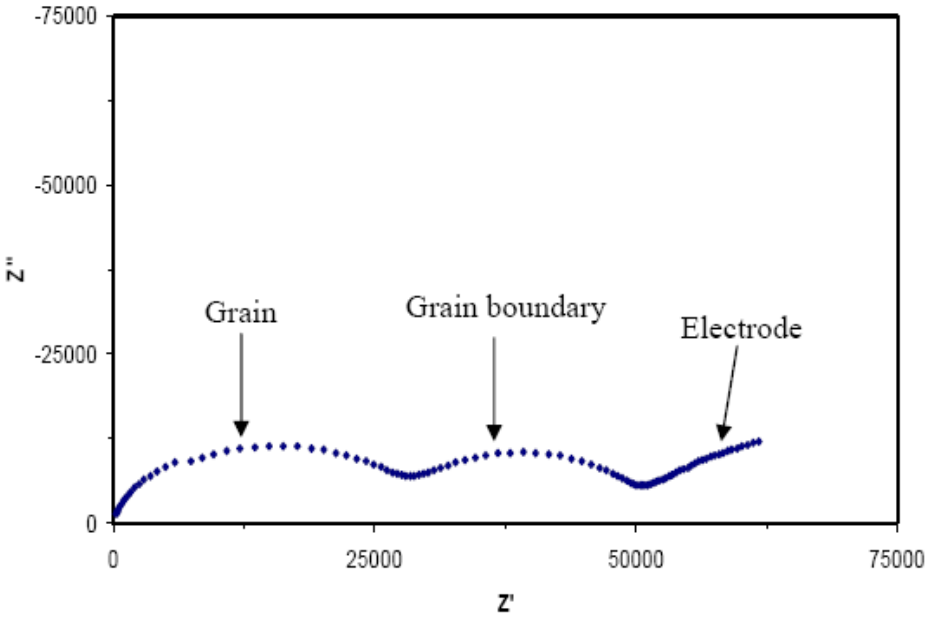

Fig. 3.1: Typical Nyquist plot for a polycrystalline ceramic sample.

Plotting of function Z in the complex plane over a range of frequencies at different temperatures is known as Nyquist plot as shown in Fig. 3.1.

In general Z is written as follows:

$$Z = Z' + Z'' \quad (3.10)$$

where Z' is the real part and Z'' is the imaginary part of Z.

Once the Nyquist plots are produced, valuable information can be extracted from the individual semicircles by using an equivalent circuit model shown in Fig. 3.2. The information extracted consists of the grain, grain boundary and electrode resistance.

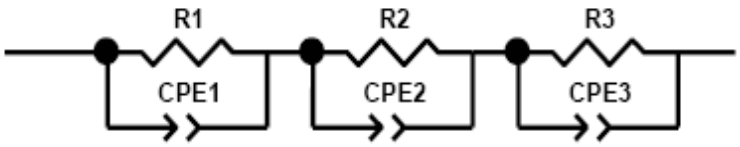

Fig. 3.2: Equivalent circuit used to describe semicircles in Impedance spectroscopy.

After the extraction of sample resistance (grain, grain boundary and electrode) from the Nyquist plot, the conductivity of the sample at a given temperature is calculated using the following equation**:**

$$\sigma = \frac{l}{RA} \tag{3.11}$$

where σ represents the electrical conductivity, l is the thickness and A is the cross-sectional area of the sample. Electrical conductivity measurement was carried out on polished and gold sputtered glass samples using impedance analyzer (Solartron Instruments, SI 1260). The measurement was done at room temperature with variable frequency range of 10 to 1*MHz*.

REFERENCES:

[1] H.K.D.H. Bhadeshia, "Thermal analyses techniques. Differential thermal analysis". University of Cambridge, Material Science and Metallurgy, (2002).

[2] R.V. Krishnan, K. Nagarajan, Thermochim. Acta, **440,** (2006) 141.

[3] G. Kaur, Investigation on interfacial interaction of glass sealants with electrolytes and interconnect for solid oxide fuel cells, Ph.D dissertation, Thapar Univeristy, Patiala, Punjab, August (2012).

[4] B.C. Smith, Fundamentals of Fourier Transform Infrared Spectroscopy Edt. 2, CRC Press, USA (2003).

[5] D.J. Gardiner, P.R. Graves, Practical Raman spectroscopy. Springer-Verlag Berlin Heidelberg, ISBN 978-0-387-50254-0 (1989).

[6] M.V. Siljegovic, S.R. Lukic Petrovic, F. Skuban, M. Avramov, L. Sidanin, Materials and Manufacturing Processes, **28,** (2013) 96.

[7] G. Sharma, K. Singh, Manupriya, H.S. Klare, V. Rajendran, A.V.G. Devi, S. B. Narang, Phys. Status Solidi A, **202,** (2005) 2720.

Chapter-4
(Results and discussion)

4.1 $x\mathrm{Na_2S} + (100-x)\mathrm{P_2S_5}$; $(35 \leq x \leq 60)$

4.2 $45\mathrm{P_2S_5}$-$(55-x)\mathrm{Na_2S}$-$x\mathrm{CuS}$; $(x = 5, 10)$

4.3 $x\mathrm{Na_2O}$+$(100-x)\mathrm{P_2O_5}$; $(40 \leq x \leq 55)$

4.4 $55\mathrm{P_2O_5}$-$(45-x)\mathrm{Na_2O}$-$x\mathrm{Li_2O}$; $(5 \leq x \leq 25)$

4.5 $55\mathrm{P_2O_5}$-$(45-x)\mathrm{Na_2O}$-$x\mathrm{K_2O}$; $(5 \leq x \leq 25)$

4.1. $xNa_2S + (100-x)P_2S_5$; $(35 \leq x \leq 60)$

4.1.1. XRD analysis

XRD patterns of xNa_2S-$(100-x)P_2S_5$; $(35 \leq x \leq 60)$ melt-quenched samples are shown in Fig. 4.1.1. The XRD patterns show two broad halos for N1, N2, N3, N4 and N5 samples. The maxima of halos are observed around ~ 15º and 30º. On the other hand, N6 sample exhibit some sharp XRD peaks.

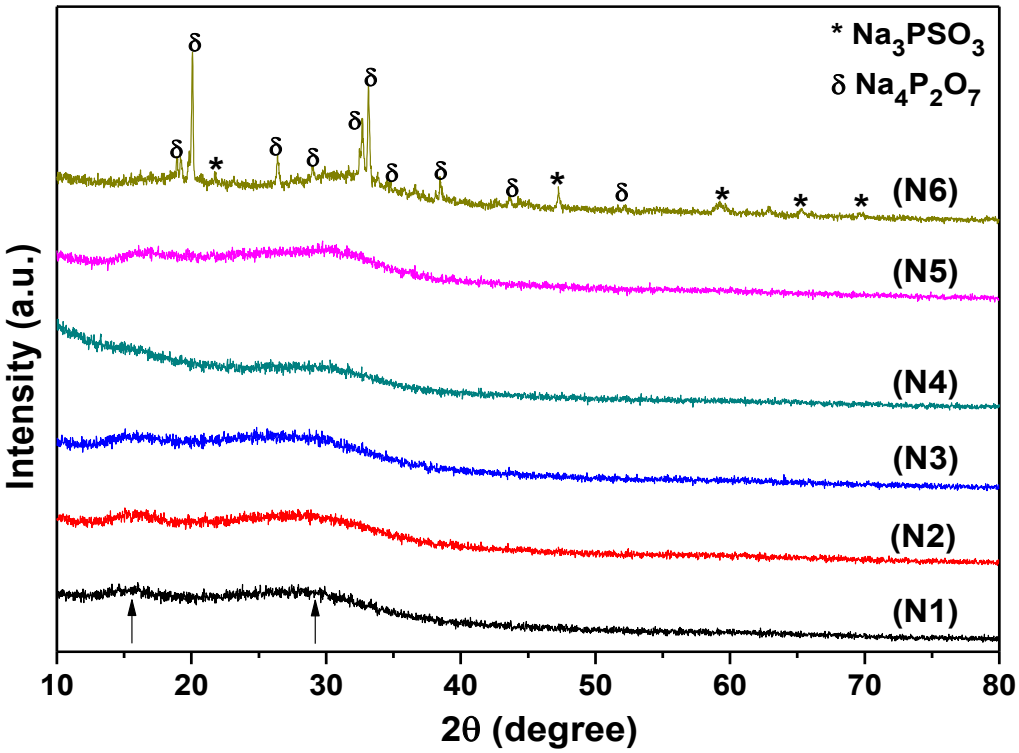

Fig. 4.1.1: XRD patterns of glasses and glass-ceramic.

The presence of two halos in Fig. 4.1.1 indicates phase separated amorphous nature of these samples. In general, it is a common phenomenon when two glass modifiers are used in initial composition. However, in the present system, a single modifier Na_2S was used. It may be possible that some amount of Na_2S has transformed to Na_2O during grinding and melting of compounds while preparing the glass. Moreover, these broad halos also correspond to their crystalline counterparts. On the other hand, crystalline phases are formed in N6 sample. These are indexed with Na_3PSO_3 (ICDD No. 00-018-1259) and $Na_4P_2O_7$ (ICDD No. 00-010-0187)

phases. The volume fractions of $Na_4P_2O_7$ and Na_3PSO_3 phases are 83 % and 17 %, respectively. The $Na_4P_2O_7$ phase is analogues to $Li_4P_2O_7$ phase which has been reported earlier for the $70Li_2S.(30\text{-}x)P_2S_5.xP_2O_5$ system. This $Na_4P_2O_7$ phase is also analogous to $Na_4P_2S_7$ phase which forms when Na_2S and Na_3PS_4 react with each other **[1].** $Li_4P_2O_7$ phase exhibits low conductivity and high activation energy **[2].** On the other hand, Villain *et al.* **[3]** reported that $Na_4P_2O_7$ phase is stable up-to 390 ºC after that it undergoes various structural transformations. $Na_4P_2O_7$ phase might have arisen due to oxygen pick up during melting and quenching of the present samples. Since samples are melted in commercial argon which may have some oxygen as an impurtity. The formation of $Na_4P_2O_7$ phase can be explained as follows:

$$2NaPO_3 + Na_2O \longrightarrow Na_4P_2O_7 \qquad (4.1)$$

Moreover, the crystalline phase $Na_4P_2O_7$ has more stability than $Na_4P_2S_7$. The chemical stability of glasses can be related to the field strength of constituent's cations. The phase ($Na_4P_2O_7$) containing oxygen in the present glass-ceramic enhances the chemical stability of sample since the field strength of Na_2O (0.20) is higher than Na_2S (0.15).

4.1.2. Thermal analysis

Dilatometric curves of N1, N2. N3, N4, N5 and N6 samples are shown in Fig. 4.1.2. The obtained softening temperature and coefficient of thermal expansion (CTE) are given in table 4.1.1. The N3 and N5 samples exhibit linear behavior between room temperature (RT) to 250 ºC. To find a small deviation in the dilatometric curve, the derivatives of the data has also been taken and shown in Figs. (4.1.3-4.1.7). These curves shows two peaks ~ (102-120 ºC) and ~ (168-180 ºC) for the as prepared glass samples. There is no signature of water evaporation is observed in the sample N3 and N5 as shown in Fig. 4.1.4 and 4.1.6, respectively.

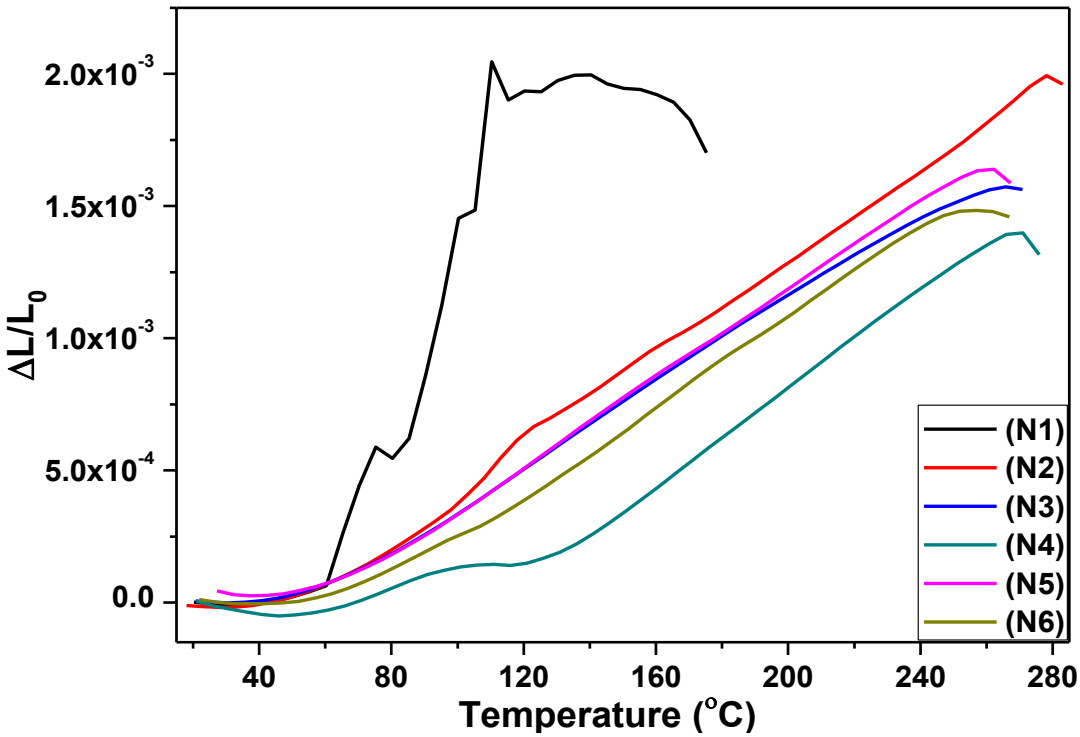

Fig. 4.1.2: Thermal expansion curves for glasses and glass-ceramic.

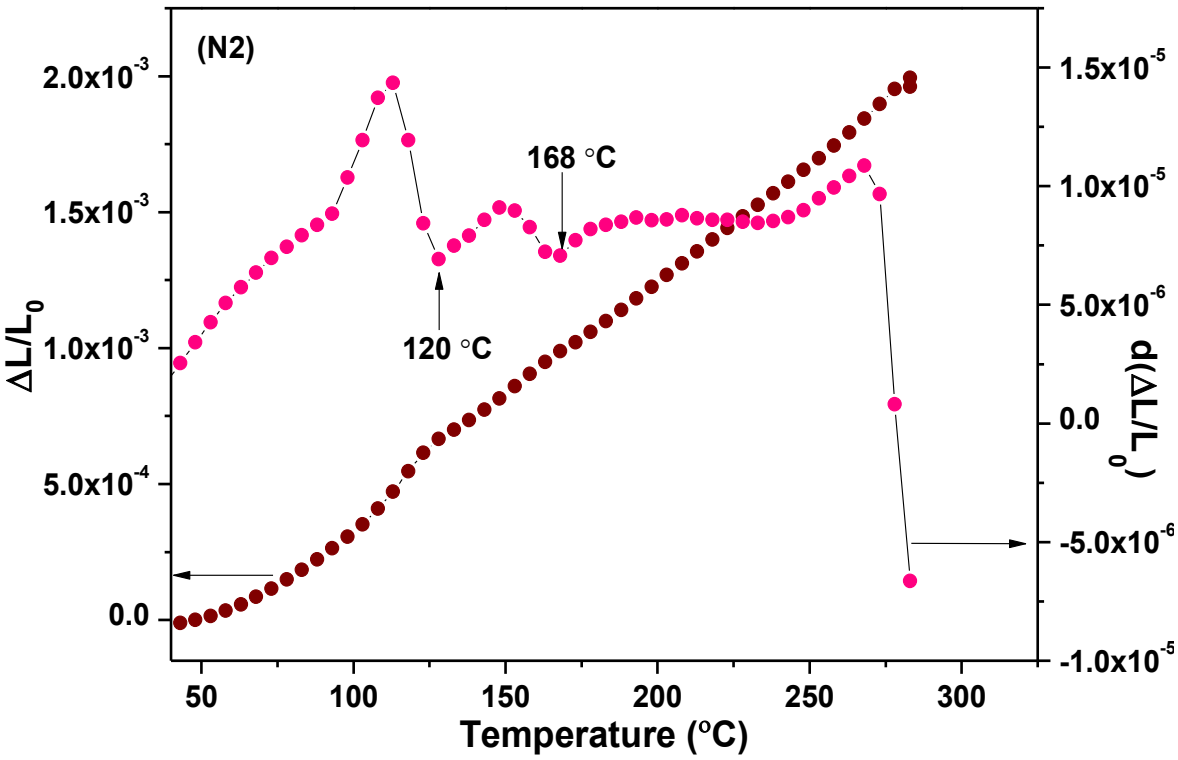

Fig. 4.1.3: Expansivity and derivative curve for 40 mol % Na_2S glass sample.

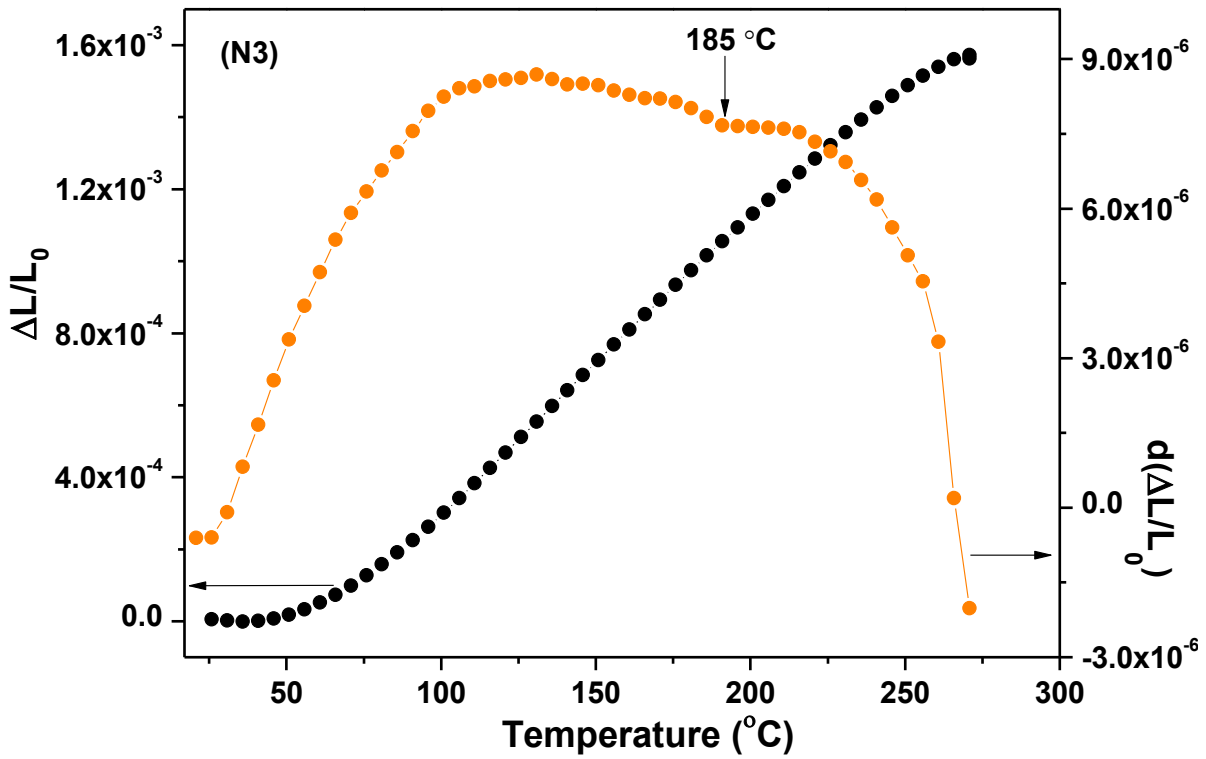

Fig. 4.1.4: Expansivity and derivative curve for 45 mol % Na_2S glass sample.

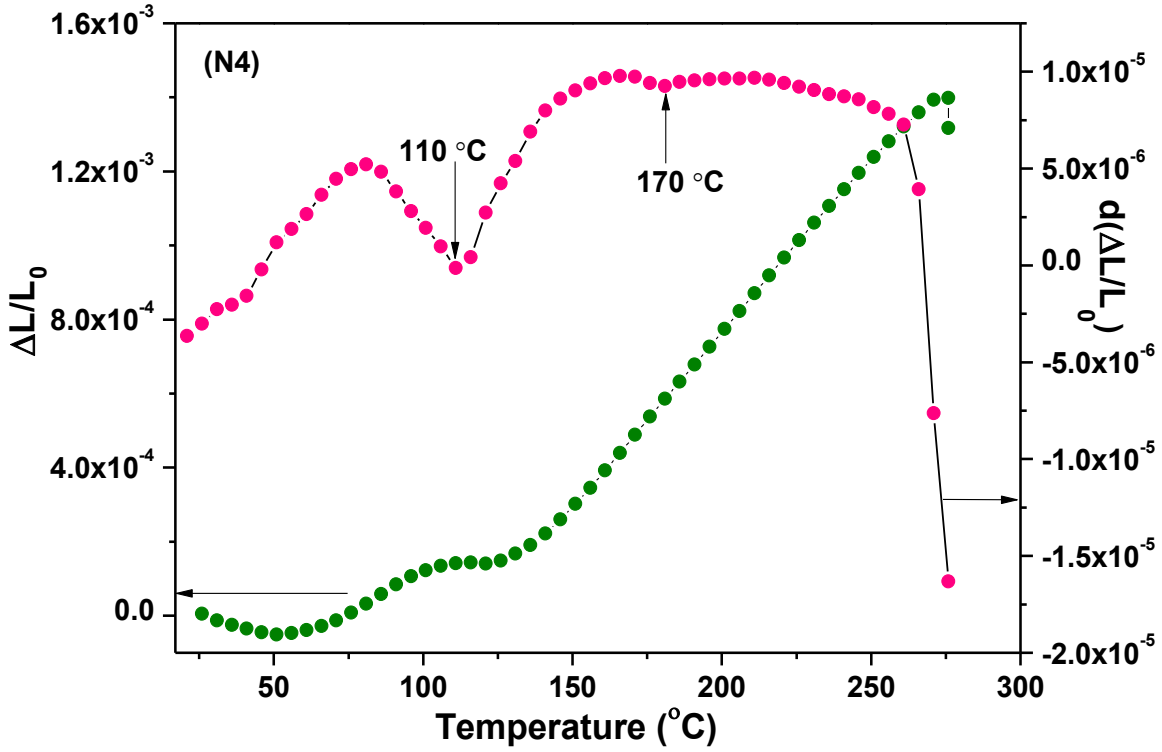

Fig. 4.1.5: Expansivity and derivative curve for 50 mol % Na_2S glass sample.

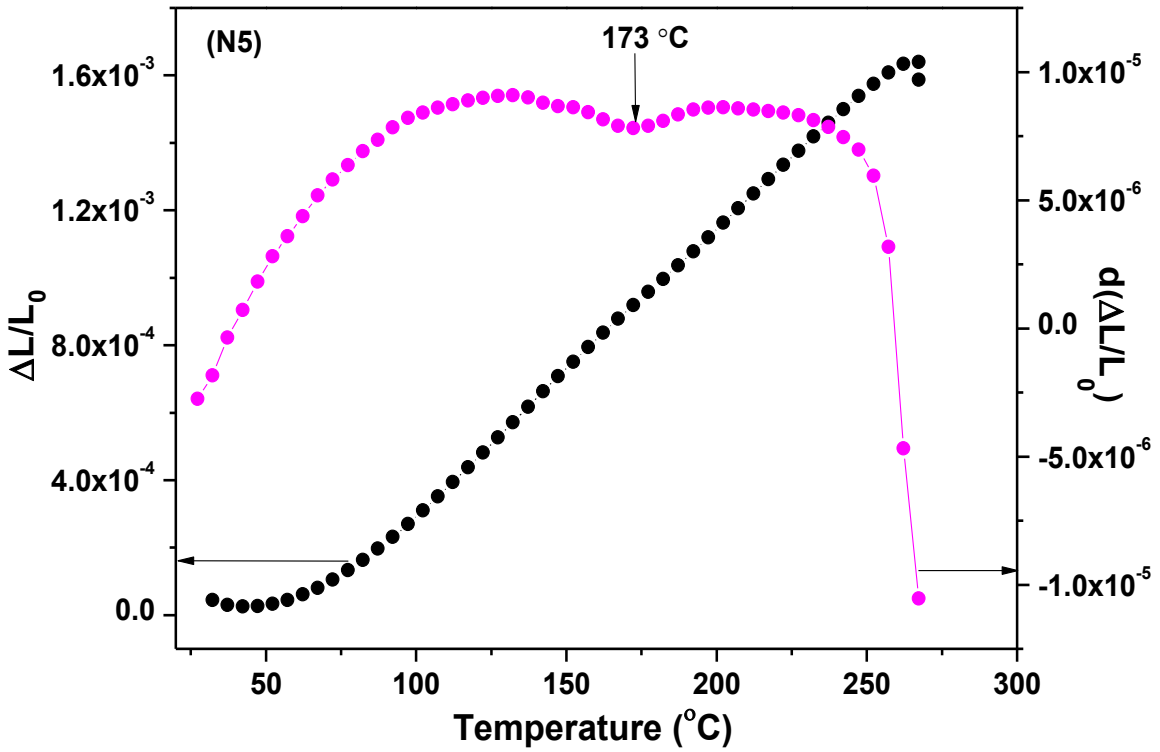

Fig. 4.1.6: Expansivity and derivative curve for 55 mol % Na_2S glass sample.

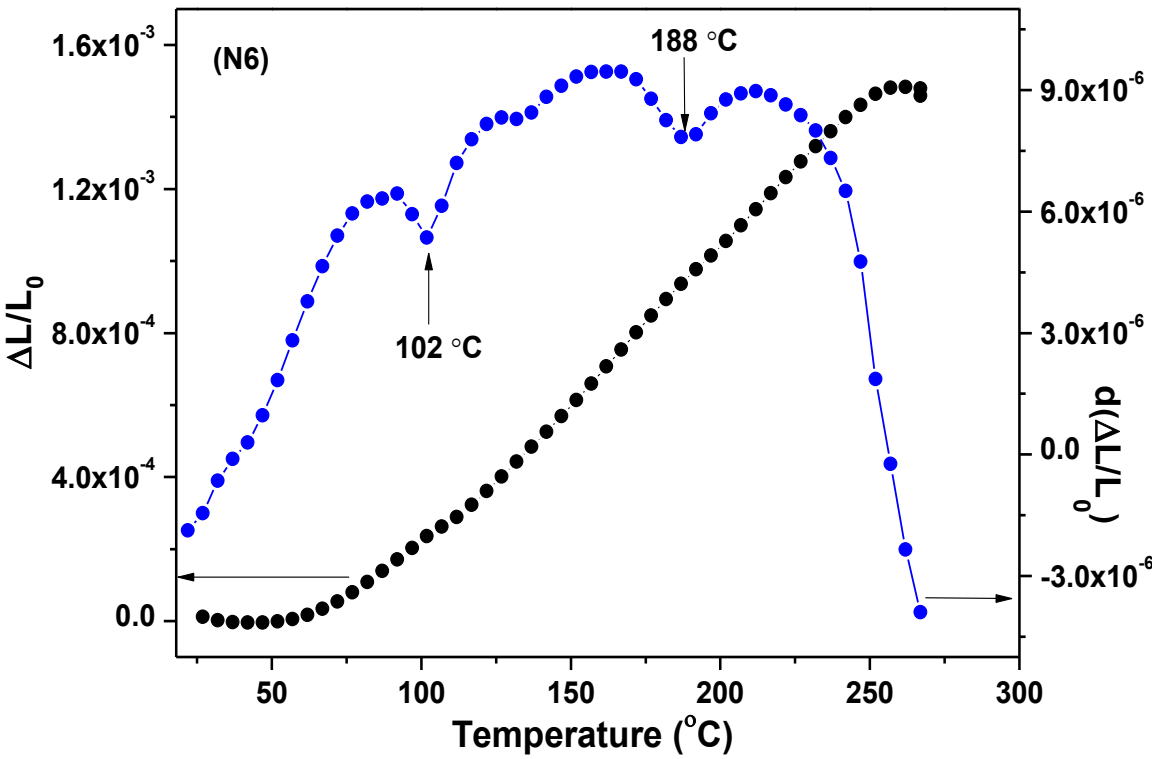

Fig. 4.1.7: Expansivity and derivative curve for 60 mol % Na_2S glass-ceramic sample.

The CTE of the materials is related to the bond nature and bond strength which leads to the asymmetric nature of energy potential well **[4].** The peaks observed at ~ 100 ºC and ~ 180 ºC in Figs. 4.1.3, 4.1.5 and 4.1.7 correspond to the water evaporation and T_g, respectively **[5].** The summarized results related to T_g and T_s are also given in table 4.1.1. The CTE values for N3 and N5 glass samples are found in the range (6.7–6.9) × 10^{-6} °C^{-1} from 25–250 ºC. Song *et al.* **[6]** also reported the CTE in the range (6.6–6.9) ×10^{-6} ºC^{-1} which is almost comparable to the β and α-alumina in the temperature range 25–300 ºC. Here also the CTE values observed for N3 and N5 glasses falls in the range as reported earlier for values for α and β-alumina solid electrolytes.

Table 4.1.1: Glass transition temperature, softening temperature, thermal expansion coefficient and H_2S generation at different time exposure for all glasses and glass-ceramic.

Sample label	T_g (ºC)	T_s (ºC)	CTE (/ºC) × 10^{-6}		H_2S generation (ppm) 10 min	20 min	30 min
N1	120	174	13.7	(25-170 ºC)	130	184	106
N2	168	275	7.7	(25-250 ºC)	107	110	104
N3	185	260	6.9	…….	101	88	97
N4	170	262	5.6	…….	127	104	103
N5	173	250	6.6	…….	106	102	99
N6	188	268	6.5	…….	116	106	102

4.1.3. FTIR bands and analysis

FTIR spectra of N1, N2, N3, N4, N5 and N6 glasses and glass-ceramic are shown in Fig. 4.1.8 and 4.1.9, respectively. The FTIR spectrum of the studied glasses and glass-ceramics is mainly composed of twelve bands. They have main characteristics of the phosphorus-oxygen, phosphorus-sulfur and hydrogen–oxygen networks. For 35 to 45 mol% Na_2S glass samples, a shift in frequency from higher to the lower region (3453 ⟶ 3436 cm^{-1}) is observed. On the other hand, for 45 to 50 mol% Na_2S glass samples, a shift in frequency from lower to the higher region (3436 ⟶ 3442 cm^{-1}) is observed. No signature of the band ~ 720 cm^{-1} are found in the N1, N2 and N3 glass samples, whereas small peak are observed for N4, N5 and N6 glass samples.

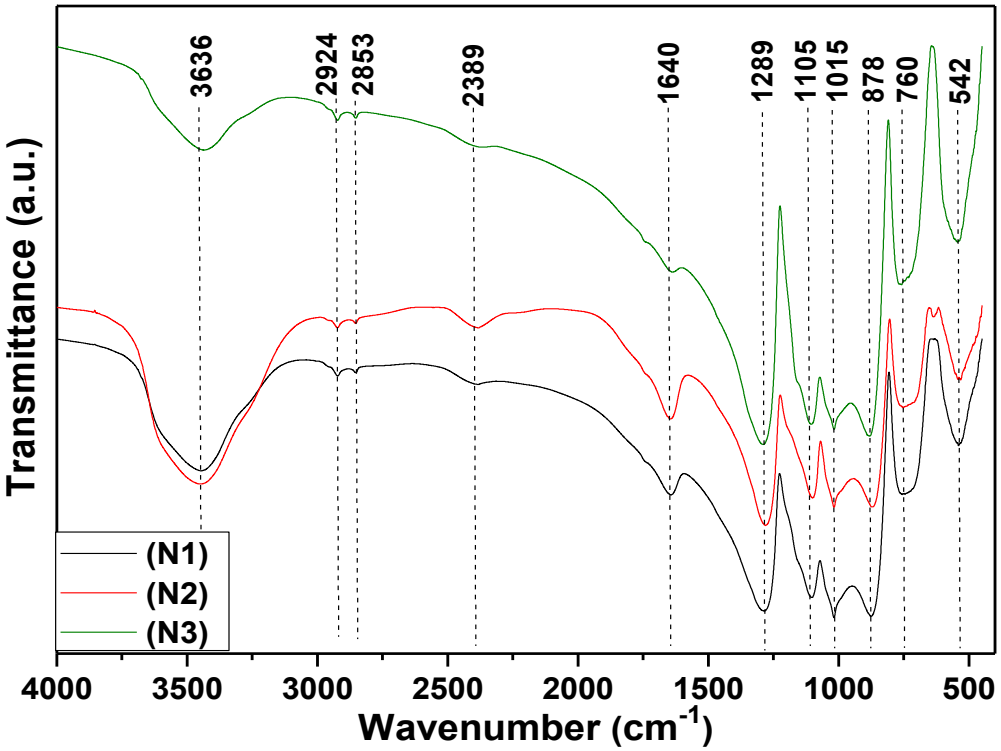

Fig. 4.1.8: FTIR spectra of the N1, N2 and N3 glasses.

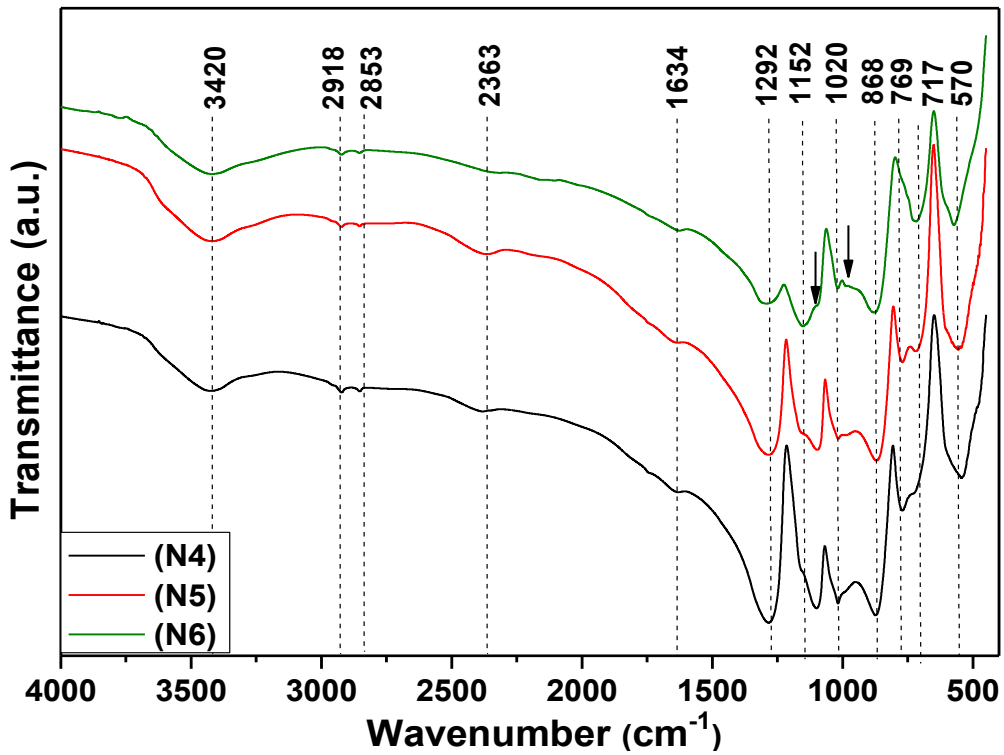

Fig. 4.1.9: FTIR spectra of the N4, N5 glasses and N6 glass-ceramic.

For N6 glass sample, the band ~ 760 cm^{-1} disappeared and a new band at 989 cm^{-1} is observed. All the identified bands along-with their assignment and different type of stretching present in the samples are given in table 4.1.2. It is well reported in literature that the water content in phosphate glasses is always higher than silicate and borate glasses due to hygroscopic nature of P_2O_5 **[7].** Water absorption also depends on the chemical nature of initial constituents. Band ~ 3440 cm^{-1} present in all the samples is attributed to the oscillations of hydroxyl groups **[8].** A certain shift in this band with Na_2S content to the lower region (3453 ⟶ 3436 cm^{-1}) designates that weakening of OH^- group is taking place. On the other hand, from 45 to 50 mol% Na_2S, the shift of the band towards a higher region (3436 ⟶3442 cm^{-1}) is observed. This shift designates that enhancement of OH^- has taken place. Moreover, bands at about 2852-2918, 2363-2395 and 1628-1653 cm^{-1} for all samples are attributed to strongly H-bonded hydrous compound, S-H vibrations and H_2O bending vibrations, respectively **[9].** The strong band near 1280-1292 cm^{-1} for all glasses and glass-ceramic is attributed to $(P=O)_{sym}$ stretching **[10].** Furthermore, the two bands near 1014-1020 cm^{-1} and 1097-1152 cm^{-1} in all glasses (N1, N2, N3, N4 and N5) are related to asymmetric stretching vibrations of P-O-P groups **[11].**

Table 4.1.2: FTIR assignments for N1, N2, N3, N4, N5 glasses and N6 glass-ceramic.

Sample label → / Wave number (cm^{-1})	N1	N2	N3	N4	N5	N6	Assignments ↓	
	540	535	542	543	554	570	ν_{as}(P-S) stretching of the PS_4^{3-}	[01]
	…	…	…	724	715	717	P-O-P stretching vibrations	[12]
	750	750	760	770	769	…	ν_s(P-O-P)	[12]
	872	870	878	872	868	878	meta-phosphate groups	[12]
	…	…	…	…	…	989	$\nu_s(SO_4^{2-})$	[09]
	1017	1014	1015	1017	1016	1020	ν_{as}(P-O-P)	[11]
	1102	1099	1105	1100	1097	1152	ν_{as}(P-O-P)	[11]
	1284	1280	1289	1283	1280	1292	ν_{as}(P=O)	[10]
	1640	1644	1640	1628	1653	1634	H_2O bending vibrations	[09]
	2395	2381	2389	2388	2370	2363	S-H vibrations	[09]
	2852	2853	2853	2853	2853	2853	OH stretching strongly H-bonded	[09]
	2923	2923	2924	2924	2920	2918	OH stretching strongly H-bonded	[09]
	3453	3452	3436	3442	3430	3420	Oscillations of hydroxyl groups	[08]

While in the case of N6 sample, the shift of a band towards the high-frequency region (1097 1152 cm^{-1}) is observed. This might be due to change in bond length and bond angle between P-O-P. Basically, higher content of Na_2S (modifier) weaken the glass network. The bands at 750-770 and 868-878 cm^{-1} are related to the symmetric stretching vibrations of P-O-P bands and different meta-phosphate groups **[12].** Berbano *et al.* **[1]** have reported that the bands near 535-570 cm^{-1} are related to asymmetric P-S stretching of the PS_4^{3-} tetrahedral unit. In the case of N6 glass-ceramic sample, this band shifted towards the higher-frequency region (535 ⟶ 570 cm^{-1}). Moreover, a new band is observed at 715-724 cm^{-1} for N4, N5 and N6 sample it can be attributed to P-O-P stretching vibrations from Q^2 units **[12].** In addition to this, in N6 glass-ceramic sample the band near 750 cm^{-1} has disappeared and new band at 989 cm^{-1} is observed. This new band at 989 cm^{-1} is related to the SO_4^{2-} symmetric stretching modes **[9].** The formation of SO_4^{2-} group can be understood as follows **[9]:**

$$S^{2-} + 4H_2O \leftrightarrow SO_4^{2-} + 4H_2 \qquad (4.2)$$

From equation (4.2), it can be concluded that large amounts of hydrogen are locally generated during oxidization of sulphide to sulphate. The IR analysis further indicates that compositions of $45Na_2S.55P_2S_5$ and $55Na_2S.45P_2S_5$ glasses have less water content and less structural change as compared to other glasses and glass-ceramics.

4.1.4. Analysis of Raman bands

Fig. 4.1.10 shows the Raman spectra of N1, N2, N3, N4, N5 and N6 samples after exposing in air for 10 min. For N1 sample, the peak intensity at 1164 cm^{-1} is found to be maximum as compared to other samples. A shift of the band toward the low-frequency region (1279 ⟶ 1256 cm^{-1}) with an increase in Na_2S content is observed. On the other hand, a shift in frequency toward higher frequency region (294 ⟶ 343 cm^{-1}) and (379 ⟶ 487 cm^{-1}) for all samples with an increase in Na_2S content is also observed.

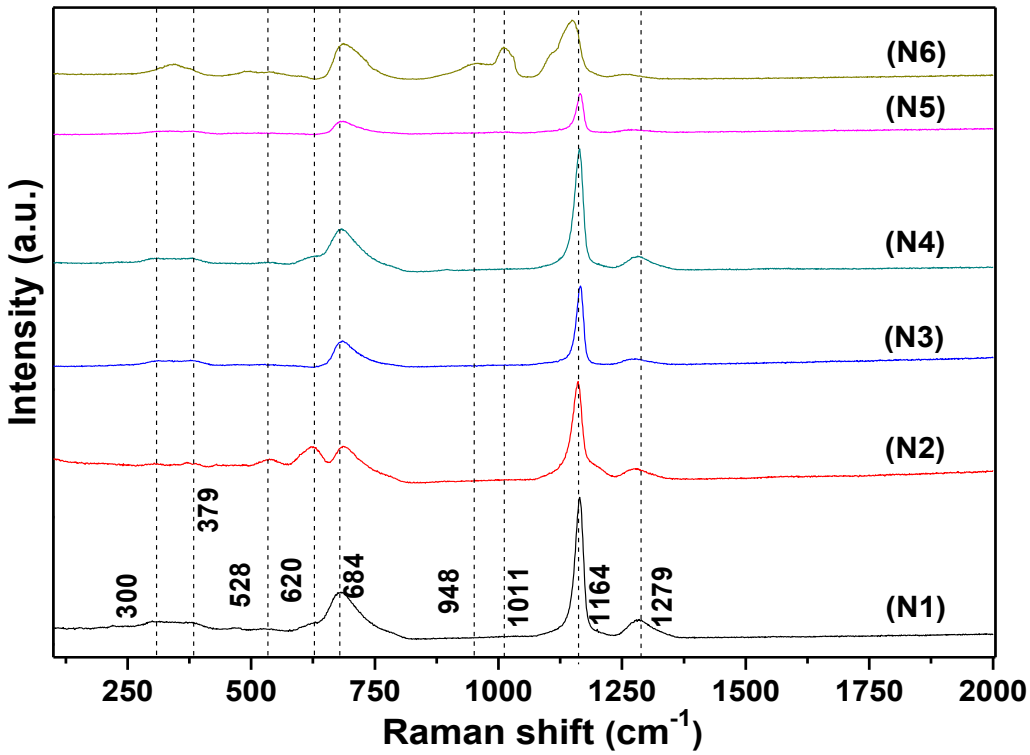

Fig. 4.1.10: Raman spectra of the N1, N2, N3, N4, N5 glasses N6 glass-ceramic.

Moreover, a strong band at 1011 cm^{-1} is observed for N6 sample as shown Fig. 4.1.10. In addition to this, for N6 glass-ceramic, a new band is observed at 948 cm^{-1} which attributed to SO_3^{2-} ion. Moreover, there is no signature of $(P\text{-}O\text{-}P)_{sym}$ stretching is observed at 621 cm^{-1} for N3, N5 and N6 samples. In all samples, N3 and N5 glasses have minor structural changes as compared to other glasses and glass-ceramic after exposing in air. All observed bands with their wave numbers are given in table 4.1.3.

Table 4.1.3: Raman assignments for N1, N2, N3, N4, N5 glasses and N6 glass-ceramic.

Sample label →	N1	N2	N3	N4	N5	N6	Assignments ↓	
Wave number (cm^{-1})	300	294	300	307	303	343	ν_{as}(P-S-P)	[15]
	379	375	386	382	384	487	P-S bond	[15]
	528	540	…	…	…	539	ν_s(P-S-P)	[14]
	620	621	…	…	…	878	ν_s(POP)	[09]
	684	690	684	683	683	690	P = S mode	[01]
	…	…	…	…	…	948	SO_3^{2-} ion	[20]
	…	…	…	1011	…	1011	$\nu_s(SO_4^{2-})$	[19]
	1164	1162	1164	1161	1164	1151	$\nu_s(PO_2)$	[13]
	1279	1276	1279	1266	1274	1256	$\nu_{as}(PO_2)$	[14]

In all the samples, an intense band is observed ~ 1151-1164 cm^{-1} after an exposure of 10 min. This intense peak has arisen due to symmetric stretching of PO_2 groups **[13].** Band intensity changes due to enhanced vibrations of PO_2 with decreasing content of Na_2S. In addition to this, the peak intensity of Raman peaks depends on the polarizability of the molecules, the intensity of the source and the concentration of the active groups. On the other hand, N2, N3, N4, N5 and N6 samples show reverse trends as observed for N1 sample. A second intense peak at 683-690 cm^{-1} is observed in all samples. It belongs to stretching vibrations of the P=S mode **[1].** Additionally, a weak band at 528-540 cm^{-1} is also seen for N1, N2 and N6 samples, it is related to P-S-P stretching mode **[14].** As the Na_2S content increases the P-S-P bond intensity increases as observed in Fig. 4.1.10. It might be attributed to enhancement of non-bridging sulfur (NBS). The creation of NBS arises due to de-polymerization of P-S-P network in glass. Consequently, the P=S stretching band intensity decreases and P-S-P stretching band intensity increases. Variation in these band intensities also depends on π-bond delocalization of Q^3, $PS(S_{3/2})$ species, which stretches the P=S terminal sulfur bond and build up the bridging sulfur P-S-P linkages with increasing Na_2S content **[1].** A third intense peak at 1256-1279 cm^{-1} is indexed with asymmetric stretching of the doubly bonded oxygen vibration in P=O modes **[14].** This mode becomes almost constant for N1, N2, N3 and N4 glass samples, whereas, for N5 and N6 this band intensity decreases. A certain shift of this band toward the low-frequency region (1279 $\longrightarrow$ 1256 cm^{-1}) and decrease in its intensity with Na_2S content is also seen. It might be attributed to increase in bond length in P-BO (phosphorus-bridging oxygen) or by the change in the P-O-P bond angles. Higher concentration of modifier is also responsible for shifting of band position. A weak band at 621 cm^{-1} is also observed in N1, N2 and N4 glass samples assigned to the symmetric stretching of tetrahedrally connected oxygens **[9].**

Furthermore, two-weak bands at 294-343 cm^{-1} and 375-487 cm^{-1} are also observed for all samples. These bands designate to the asymmetric stretching of P-S-P bond and $P_2S_6^{4-}$ ion, respectively **[15].** The certain shift of a band from (294 ⟶ 343 cm^{-1}) is related to slight non-stoichiometry in the materials **[15].** Moreover, the stretching vibration of the P-S bond in the hexathiophosphate ($P_2S_6^{4-}$) ion is also responsible for the higher-frequency **[16].** The formation of $P_2S_6^{4-}$ can arise from a well-known disproportionation reaction as given below **[17]:**

$$P_2S_7^{4-} \longrightarrow P_2S_6^{4-} + 1/8S_8 \qquad (4.3)$$

The peak ~ 380 cm^{-1} strongly depend upon the amount of Na_2S content. Higher Na_2S content is responsible for the higher intensity of bands associated with the large number of non-bridging sulfur atoms. Moreover, in the present samples, this peak does not show much more change with respect to Na_2S concentration. On the other hand, a shift is also observed from (375⟶ 487cm^{-1}) in N6 glass-ceramic sample. It indicates that the reaction between P and S for the formation of $P_2S_6^{4-}$ (phosphorus-sulfur) has taken place. The same behavior is also observed in the Li_2S based glass-ceramics **[18].** Moreover, a new strong band ~ 1011 cm^{-1} is observed for N6 glass-ceramic sample as shown in Fig. 4.1.10. This peak is attributed to the asymmetric stretching of P-O-P groups linked with small meta-phosphate rings **[19].** In addition to this, for N6 glass-ceramic sample, a new band is also observed at 948 cm^{-1}, which is due to SO_3^{2-} ions **[20].**

4.1.5. H_2S gas generation

The relative amount of H_2S gas generated from the prepared glasses and glass-ceramic are investigated by gas chromatography. The amount of H_2S gas generated after different time exposure in air for all glasses including for N6 glass-ceramic samples is shown in Fig. 4.1.11. The amount of H_2S at the y-axis indicates the calculated amounts of H_2S generated by these sulfide glasses and glass-ceramic after exposure to air at 10, 20 and 30 min, respectively.

The calculated amounts of H_2S after exposure for the different time period for all samples are given in table 4.1.1. N3 and N5 glass samples generated lesser amount of H_2S gas as compared to other samples. Among all the studied samples, the H_2S generation is found to be maximum for N1 glass sample at different time intervals. The H_2S generation decreases from 35 to 45 mol% Na_2S. As modifier (Na_2S) concentration increases from 45 to 50 mol%, the H_2S generation further increases. Moreover, from 50 to 55 mol% Na_2S, the decreasing trend of H_2S generation is found. On the other hand, for 60 mol% Na_2S, the H_2S generation further increases after exposure of air for 10 min. The same behavior was also observed when the samples were exposed to air for 20 and 30 min. It is worth mentioning that the amount of H_2S generated from the Na_2S-P_2S_5 glasses is highly dependent on the glass composition. The presence of two sulfide compounds in the glass system is highly favorable condition for generation of H_2S in the presence of water molecules **[21, 22].** For N1 glass sample, total number of S atoms present in the composition ($35Na_2S$-$65P_2S_5$) is more as compared to other compositions.

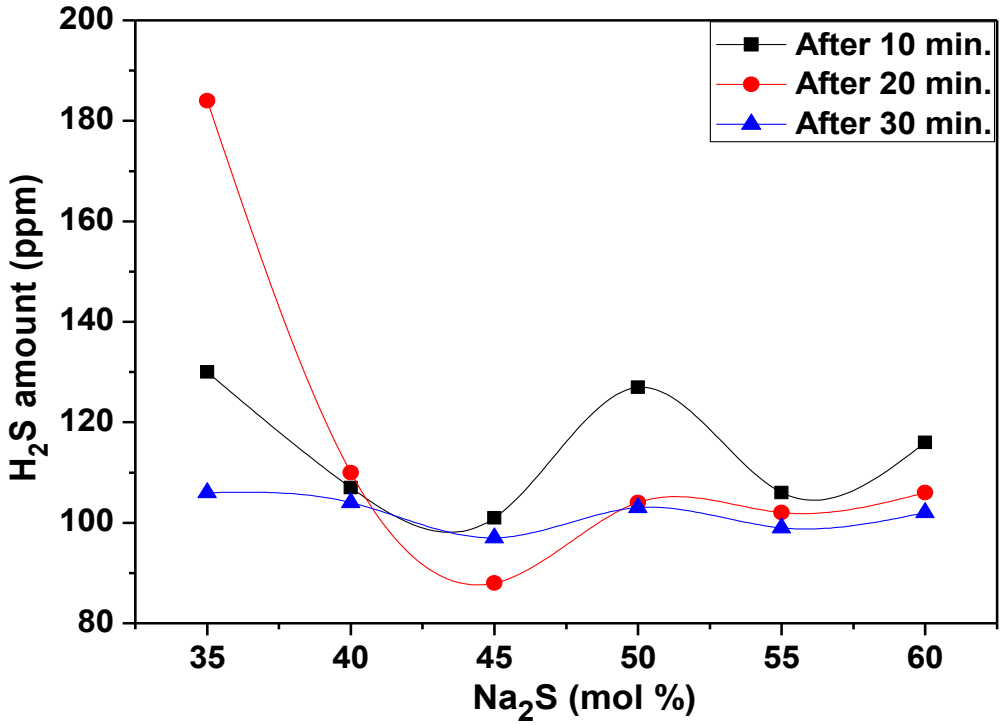

Fig. 4.1.11: Amounts of H_2S generated after 10, 20 and 30 min from glasses and glass-ceramic.

During exposure in air transformation of $Na_4P_2S_7 \longrightarrow Na_4P_2O_7$ occurs **[1]** where S is replaced by O and amount of S in the form of H_2S is liberated after reacting with atmospheric H_2O. As time increases from 10 to 20 min., the reaction $Na_4P_2S_7 \longrightarrow Na_4P_2O_7$ generates more amount of S at the surface which further increases the H_2S content. However, with further increase in time from 20 to 30 min. system gets saturated that lead to decrease in H_2S content. With increase in Na_2S content from 35 to 60 mol% the similar trend of H_2S liberation is also found with respect to time. Glasses N2, N3, N4, N5 and glass-ceramic N6, liberated less amount of H_2S content as compared to N1 glass. However, in all samples the variation observed for 10 and 20 min. is more as compared to 30 min. In addition to this, after 30 min. exposure of all glasses, amount of H_2S liberated is nearly same (97 to 106 ppm) as shown in table 4.1.1. Similar behavior of H_2S gas generation is also reported for Li_2S-P_2S_5 glasses where amount of H_2S generated in one minutes of exposure in air decreases up-to 75 mol% Li_2S content after that it increases **[22].** From above discussion, it is conclude that compositions of $45Na_2S.55P_2S_5$ and $55Na_2S.45P_2S_5$ glasses generated lesser amounts of H_2S as compared to other glasses. This shows that compositions of $45Na_2S.55P_2S_5$ and $55Na_2S.45P_2S_5$ glasses have more stability as compared to other glasses. This is in good agreement with Raman and dilatometric studies. After above study, best N3 and N5 glass samples are further investigated for their crystallization kinetics and electrical conductivity.

4.1.6. Crystallization kinetics analysis from DTA

The crystallization kinetic of present samples is studied in terms of T_g, T_c and E_a of the thermal relaxation. The T_g of an amorphous material is the critical temperature at which the material changes its behavior from a hard (relatively brittle) state to a molten (rubber-like) state. The kinetics of phase transformation which involves the nucleation and growth under non-isothermal condition is calculated using Kissinger's model. Figs. (4.1.12) and (4.1.13) show the

DTA curves for N3 and N5 glass samples at four heating rates of 10, 20, 30 and 40 ºCmin^{-1} in the temperature range 50-700 °C. A very weak endothermic signature below 120 ºC in both glasses is attributed to the dehydration of absorbed water. The T_g, T_c and T_m at different heating rates are marked in Figs. (4.1.12) and (4.1.13). The T_g of the present glasses are found to be lower than the silicate glasses **[23, 24].** In addition to this, it was found that an increase in Na_2S content with 45 mol % to 55 mol %, T_g and T_c decreases. In the present case, some Na_2S might have converted into Na_2O during processing since glasses were prepared in air atmosphere. The formed Na_2O and Na_2S act as a glass modifiers that increases the non-bridging oxygens (NBOs) and non bridging sulfurs (NBSs) causing a decrease in T_g and T_c values **[25]**. On the other hand, the reverse trend is found for T_m. As the melting temperature of $Na_2S.9H_2O$ is ~ 920 ºC and the melting temperature of P_2S_5 is ~ 280 ºC. So, from 45 mol % to 55 mol %, the content of Na_2S increases, this increases the T_m. Moreover, it has been observed that the characteristic thermal constants of both glasses are showing an increasing behavior with increasing heating rates as given in table 4.1.4. The increase in T_g with increasing heating rate is attributed to the relaxation dynamics in the glass transition. Theoretically, the product of relaxation time (τ) and T_g is always constant i.e. $\tau.T_g$ = constant **[26].** Hence, as the heating rate increases, the relaxation time decreases and the T_g increases. Moreover, the shift of T_c to higher temperatures with high heating rate is also observed. It might be attributed to the fact that the system does not get sufficient time for nucleation and crystallization. In other words, we can say that with increase in heating rate, delayed nucleation process is taking place. In DTA curves, the maxima of crystallization peak correspond to temperature at which the rate of transformation of viscous liquid into crystals becomes the maximum **[27].** For both glasses, the activation energy of T_g and T_c has been calculated by using Kissinger model.

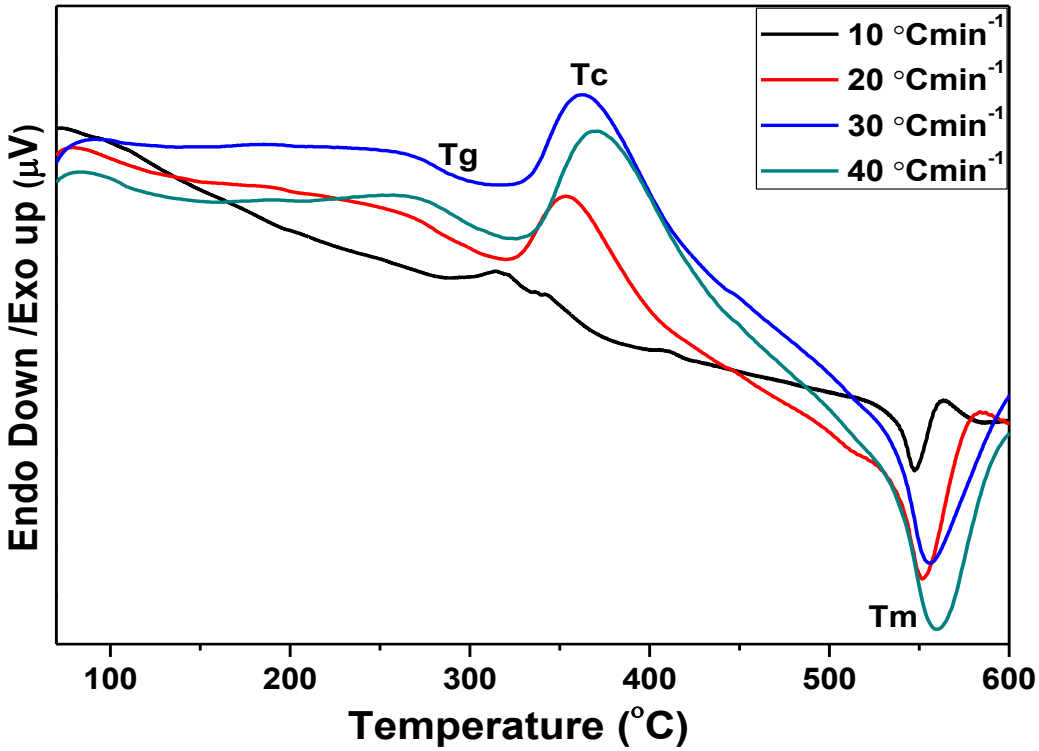

Fig. 4.1.12: DTA curve for N3 glass at different heating rates.

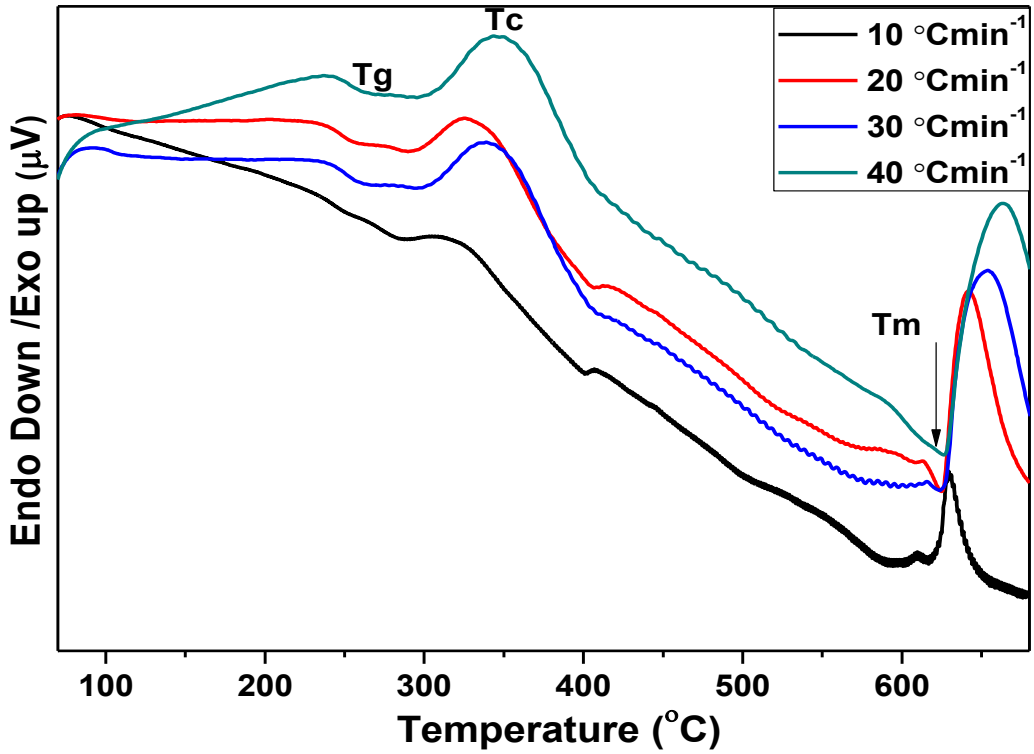

Fig. 4.1.13: DTA curve N5 glass at different heating rates.

For homogenous with spherical nuclei crystallization, Kissinger model can be used as follows **[27]:**

$$ln\,[T_c^2/\alpha] = E_a/(RT_c) + \text{constant} \quad (4.4)$$

where T_c is the peak crystallization temperature, α is the heating rate, R is the gas constant and E_a is the activation energy. A graph between ln $[T_c^2/\alpha]$ and $1000/T_c$ gives straight line. The slope (E_a/R) of the fitted line provides the activation energy of the crystallization. The data were well fitted with T_g and T_c in straight lines at different heating rates for N3 and N5 glass samples as shown in Figs. 4.1.14 (a and b). Moreover, the values of activation energy for T_g, and T_c, are given in table 4.1.4, which indicates that glass sample N3 has high activation energy as compared N5. In the present study, Na_2S or some converted Na_2O are acting as a modifier. As the modifier content Na_2S/Na_2O increases from 45 to 55 mol % it increases the number of NBSs/NBOs in the glass. These NBSs/NBOs are considered as defects, which lead disordering in the system. Consequently, the activation energy decreases with increasing defects (NBSs/NBOs).

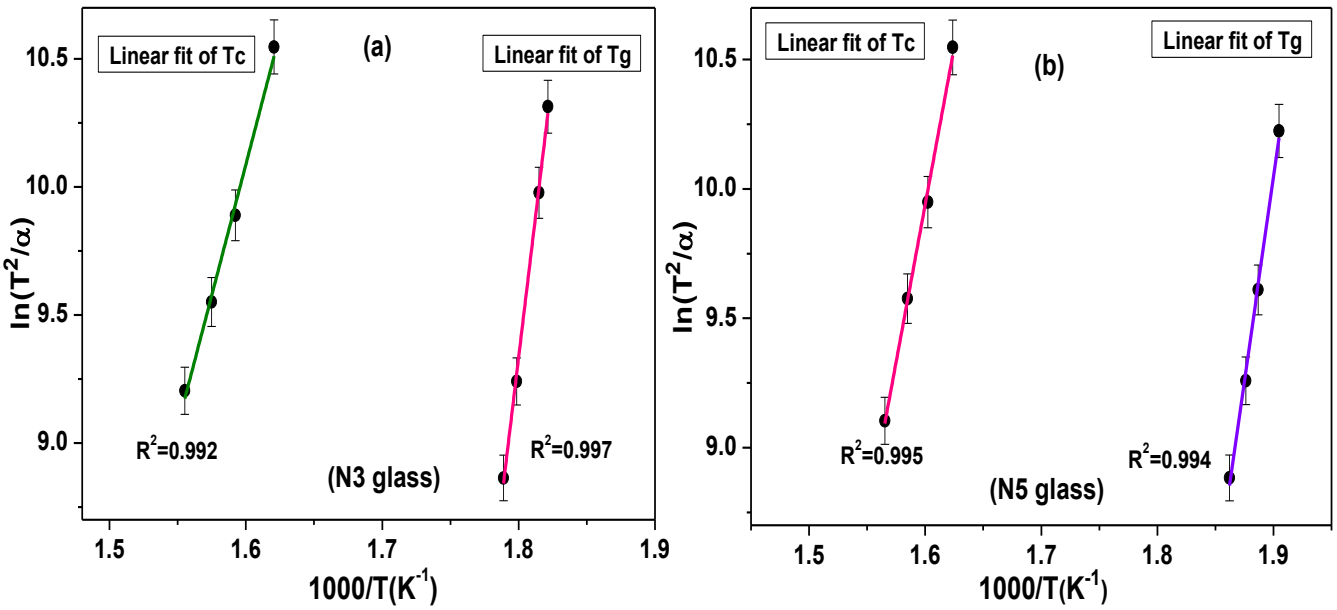

Fig. 4.1.14: Kissinger plots for T_g and T_c at different heating rates for N3 (a) and N5 (b) glass sample.

A parameter (ΔT) **[28]** usually employed to glass stability is as follows:

$$\Delta T = T_c - T_g \quad (4.5)$$

This parameter is calculated at different heating rates, and the values of T_c and T_g obtained from Fig. 4.1.12 and Fig. 4.1.13 are different, which is also presented in table 4.1.4. Usually, the large difference between T_c and T_g attributes to higher glass stability **[24].** If we compare the stability parameter, N3 glass shows high stability than N5 glass. Another aspect which combines both nucleation and growth of glass transformation, the parameter is H_r **[29].** It can be related as given in equation (4.6):

$$H_r = (T_c - T_g)/(T_m - T_c) \quad (4.6)$$

where, T_c, T_g and T_m corresponds to crystallization temperature, glass transition temperature and melting temperature of glass, respectively. From table 4.1.4, we observe that H_r value increases with increasing heating rate. This study further indicates that nucleation is delayed at higher heating rate as the value of H_r increases for N3 glass from 0.33 to 0.44 and for N5 glass from 0.22 to 0.29.

Table 4.1.4: Thermal constants at different heating rates for N3 and N5 glass samples.

Sample label	α (^{0}C min^{-1})	T_g (^{0}C)	T_x (^{0}C)	T_c (^{0}C)	T_m (^{0}C)	$\Delta T = T_c - T_g$ (^{0}C)	E_a (kJ mol^{-1})	$H_r = (T_c - T_g)/(T_m - T_c)$
N3	10	276	288	344	547	68		0.33
	20	278	292	355	552	77	370 (T_g)	0.39
	30	283	297	362	555	79	170 (T_c)	0.40
	40	286	300	370	559	84		0.44
N5	10	252	302	318	616	66	264 (T_g)	0.22
	20	257	321	325	621	68	167 (T_c)	0.22
	30	260	324	338	624	78		0.27
	40	264	328	345	626	81		0.29

4.1.7. Electrical conductivity

A graph between Z' and Z'' are plotted for N3 and N5 glass samples which is presented in the Fig. 4.1.15 (a) and (b). The value of resistance (R) in the present glass samples at room temperature was evaluated from the intercepts of the semicircle on the real axis (Z') and calculated the conductivity using the following relation:

$$\sigma = \frac{l}{RA} \tag{4.7}$$

where σ represents the conductivity, A is the cross-sectional area and l is the thickness of the prepared pellet of glass sample. High electrical conductivity in any solid electrolyte generally occurs because of large number of the charge carriers along with less activation energy for the movement of ions. From Fig. 4.1.15 (a) and (b), it is observed that glass sample N3 have more grain resistance as compared to N5 glass samples. The ac conductivities are calculated and presented in the table 4.1.5. The N5 glass sample exhibit higher conductivity than N3. This phenomenon occurs because as the Na_2S/Na_2O content increases from 45 to 55 mol %, it increases the number of NBSs/NBOs in the glass. The NBSs/NBOs generally creates disorderness which is responsible for the high ionic conductivity. An extensive range of materials, including polycrystalline semiconductors, organic-inorganic composites, transition metal oxides, polymers, glasses, glass-ceramics, etc., exhibit a frequency-dependent conductivity often known as *Johnscher's Universal Response* **[30].** In these materials, at high frequencies, the conductivity becomes strongly frequency-dependent**;** on the other hand, at low frequencies, it gives constant conductivity. To separate out these frequency-dependent/independent behaviors from the present samples, we used *Johnscher's power law* as given below **[31]:**

$$\sigma_{ac}(\omega) = \sigma_{dc} + B\omega^{s} \tag{4.8}$$

where, σ_{dc} is the direct current conductivity of the glass sample, *B* is a constant temperature dependent parameter and s is the power exponent. The exponent *s* designates the interactions of the electrons, impurities, charges, etc. The transport mechanism generally occurs by the thermally activated hopping process between two sites separated by an energy barrier.

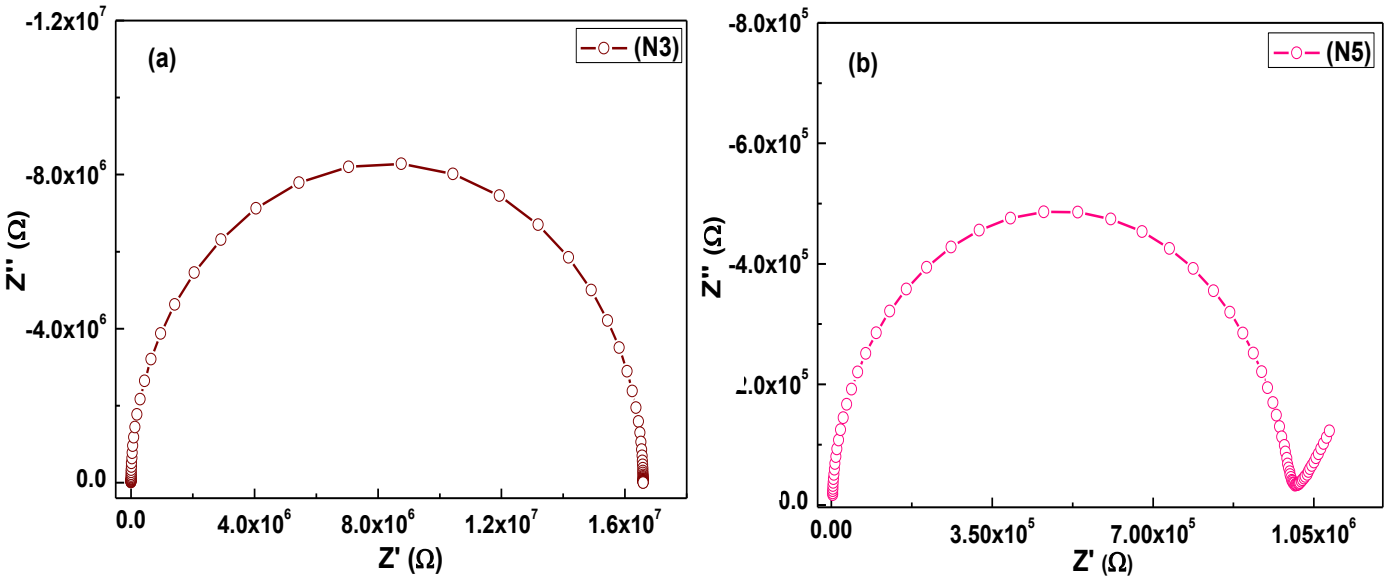

Fig. 4.1.15: Impedance spectra of N3 (a) and N5 (b) glass samples at room temperature.

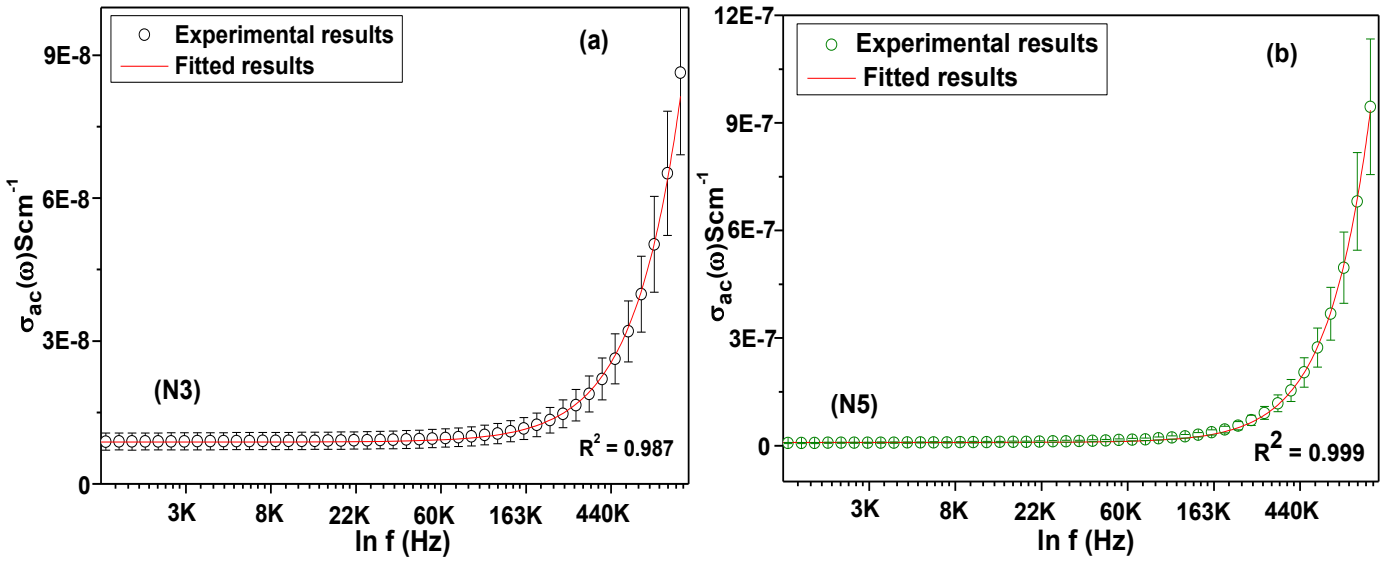

Fig. 4.1.16: Johnscher's plots for N3 (a) and N5 (b) glass samples at room temperature.

Table 4.1.5: Grain resistance, ac and dc conductivity at room temperature and other fitting parameters for N3 and N5 glass samples.

Sample	R_g (Ω) $\times 10^6$	σ_{ac} $\times 10^{-7}$(Scm^{-1})	σ_{dc} $\times 10^{-9}$(Scm^{-1})	B $\times 10^{-19}$	s	R^2	ω_h $\times 10^4$ (Hz)
N3	16.7	0.87	8.87	2.11	1.92	0.999	33.45
N5	1.02	9.45	9.07	6.17	2.02	0.999	10.79

Equation (4.8) is used to fit the ac conductivity data to calculate dc conductivity. During fitting, *B* and *s* values were varied simultaneously to attain best fits. The fitted graphs for N3 and N5 glass samples have been shown in the Fig. 4.1.16 (a) and (b). After fitting, the parameters *B*, *s* along with dc conductivity have been calculated and presented in the table 4.1.5. In addition to this, for the present samples the hopping frequency (ω_h) is also calculated. It is known as that frequency at which value of dc conductivity crossover to the ac conductivity.

A formula for hoping frequency is given below

$$\omega_h = \left(\frac{\sigma_{dc}}{B}\right)^{1/s} \quad (4.9)$$

The as obtained values of *B*, *s* and σ_{dc} were taken from table 4.1.5 and with the help of equation (4.9) the hoping frequencies (ω_h) for both samples were calculated and presented in table 4.1.5. From table 4.1.5, it is observed that glass sample N3 can easily crossover from dc to ac at high frequency. On the other hand, for glass sample N5; lower frequency is required to crossover from dc to ac conductivity. It is observed from above study that sample having 55 mol% Na_2S shows good stability along-with high electrical conductivity. Therefore, CuS is replaced with Na_2S for this particular composition $45P_2S_5$-$55Na_2S$ to increase the durability of glasses and electrical conductivity, which is discussed in details in the next section.

4.2. $45P_2S_5$-(55-*x*)Na_2S-*x*CuS; (*x* = 5 and 10)

4.2.1. XRD analysis

Fig. 4.2.1 shows the XRD patterns of $45P_2S_5$-(55-*x*)Na_2S-*x*CuS; (*x* = 5 and 10 mol%) melt-quench samples. *x* = 5 and *x* = 10 mol% CuS is labeled as NC5 and NC10, respectively. The XRD patterns show two broad halos maxima ~ 17º and 31º including one crystalline peak ~ 32.13º for NC5 and NC10 samples. The presence of two halos in Fig. 4.2.1 indicates phase separated amorphous nature of both the samples which is already discussed in the previous section 4.1.1. The presence of crystalline peak is indexed with $Cu_{1.8}S$ (ICDD No. 01-085-1693) having rhombohedral crystal structure. The crystalline phase $Cu_{1.8}S$ is a stable p-type compound, which is generally used in solar cells as absorber materials **[32, 33].**

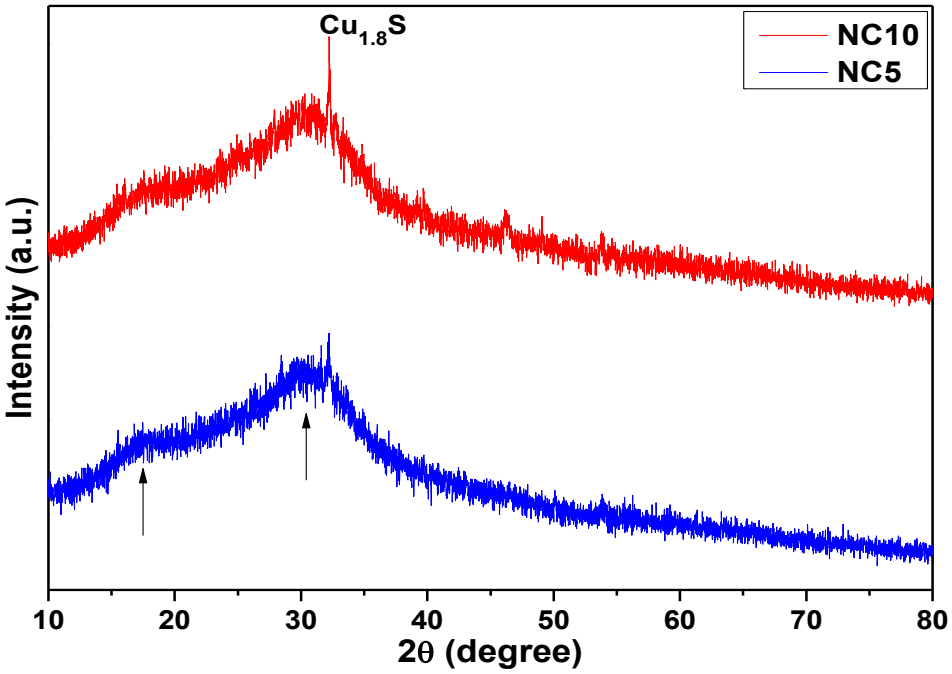

Fig. 4.2.1: XRD patterns of NC5 and NC10 glass samples.

4.2.2. Thermal analysis

Fig. 4.2.2 shows the DTA curves for NC5 and NC10 glasses at heating rate of 10 °Cmin^{-1} from 50 to 600 °C. For both glasses, the characteristics temperatures are marked clearly. From DTA curves, the values of T_g, T_x, T_c and T_m were evaluated and given in the table 4.2.1.

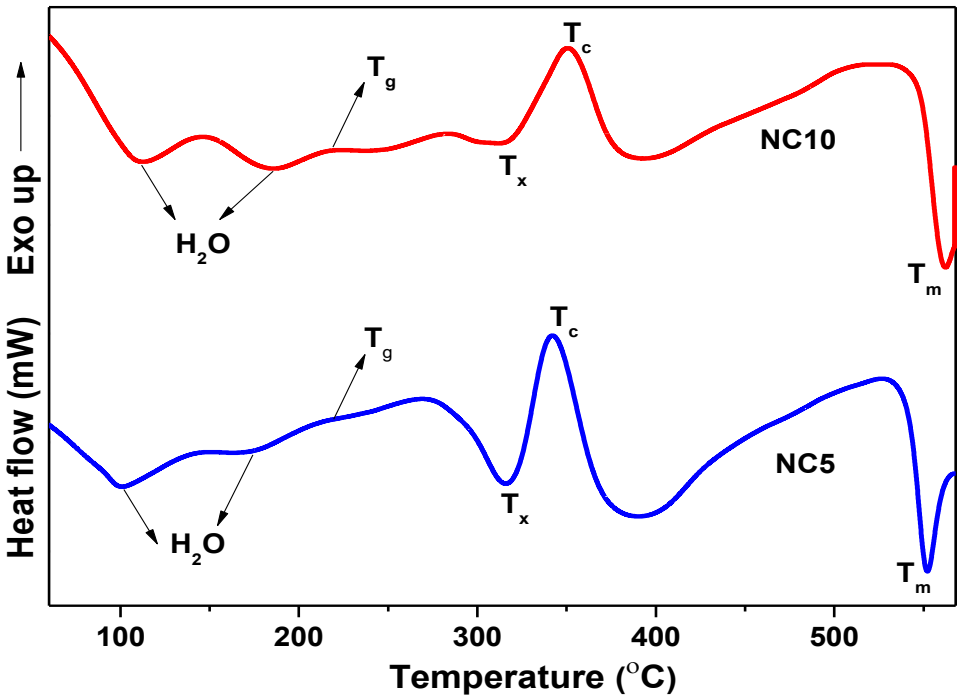

Fig. 4.2.2: DTA curves of NC5 and NC10 glass samples at heating rate of 10 °Cmin^{-1}.

From table 4.2.1, it is observed that as the content of CuS increases from 5 to 10 mol%, all the characteristics temperatures are shifted at higher temperature which indicates that with CuS content thermal stability increases. A parameter (ΔT) which is employed to glass stability is evaluated with the help of equation (4.5). The large difference between T_c and T_g attribute to highly stable category of glass **[24].** From table 4.2.1, it is observed that the value of ΔT is high in NC10 than NC5 glass, which indicates that NC10 glass is more stable than NC5 glass. The addition of CuS on the expense of Na_2S increases the stability of the glass samples.

Saad and Poulain **[34]** have also given an equation for thermal stability in glasses as follows:

$$S = (T_c - T_x)\,(T_x - T_g)/T_g \qquad (4.10)$$

where, S corresponds to resistance to devitrification after the formation of the glass. $(T_c - T_x)$ corresponds to the rate of devitrification transformation of the glassy phases whereas; the high value of $(T_x - T_g)$ designates the delayed nucleation process.

Table 4.2.1: Characteristic temperatures of glasses with their stability parameter.

Sample label	T_g (°C)	T_x (°C)	T_c (°C)	T_m (°C)	ΔT	S	H_r
NC5	215	316	342	551	127	12.21	0.60
NC10	219	313	350	562	131	15.89	0.62

This analysis further supported the ΔT values that NC10 glass exhibits high stability than NC5 glass. Hurby *et al.* **[29]** have given a parameter H_r which combines both nucleation and growth aspects of glass transformation which is calculated with the help of equation (4.6). From table 4.2.1, we have observed that NC10 glass showed high values of H_r than NC5 glass. This phenomenon further indicated that NC10 glass is more stable than NC5 glass. In the initial composition $45P_2S_5$-$55Na_2S$, the stability parameter ΔT was observed ~ 66. However, replacing the Na_2S by CuS with 5 and 10 mol%, ΔT observed is ~ 130 which further confirmed that with CuS content thermal stability of the glasses increases.

4.2.3. FTIR analysis

FTIR spectra of the NC5 and NC10 glass samples in the frequency range of 2800-450 cm^{-1} are shown in Fig. 4.2.3. There are nearly eleven bands present in the both glasses. They are mainly composed of the phosphorus–oxygen, phosphorus–sulfur and hydrogen–oxygen bonds. The bands ~ 2360, 2332 and 1649 cm^{-1} present in both glass samples is attributed to bending vibration of H_2O molecules **[35, 36].** The intense peak ~ 1277 cm^{-1} and small signature ~ 1151 cm^{-1} in both glasses correspond to the asymmetric and symmetric stretching modes of PO_2 groups in Q^2 phosphate tetrahedral, respectively **[37, 38].** In addition to this, bands ~ 1097 and 987 cm^{-1} are associated with the formation of the PO_3^{2-} (terminal phosphate groups) in Q^1 structural units and SO_4^{2-} symmetric stretching modes **[39 9].** The formation of SO_4^{2-} group can be understood from equation (4.2). From equation (4.2), it can be concluded that large amounts of hydrogen are locally generated during oxidization of sulphide to sulphate.

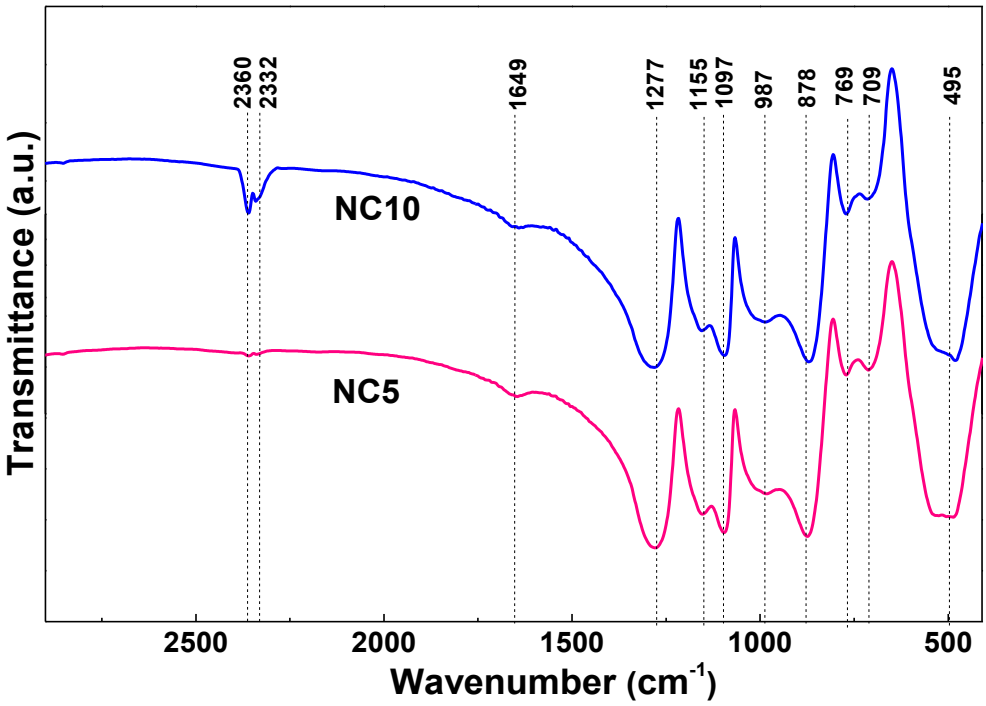

Fig. 4.2.3: FTIR spectra of NC5 and NC10 glass samples.

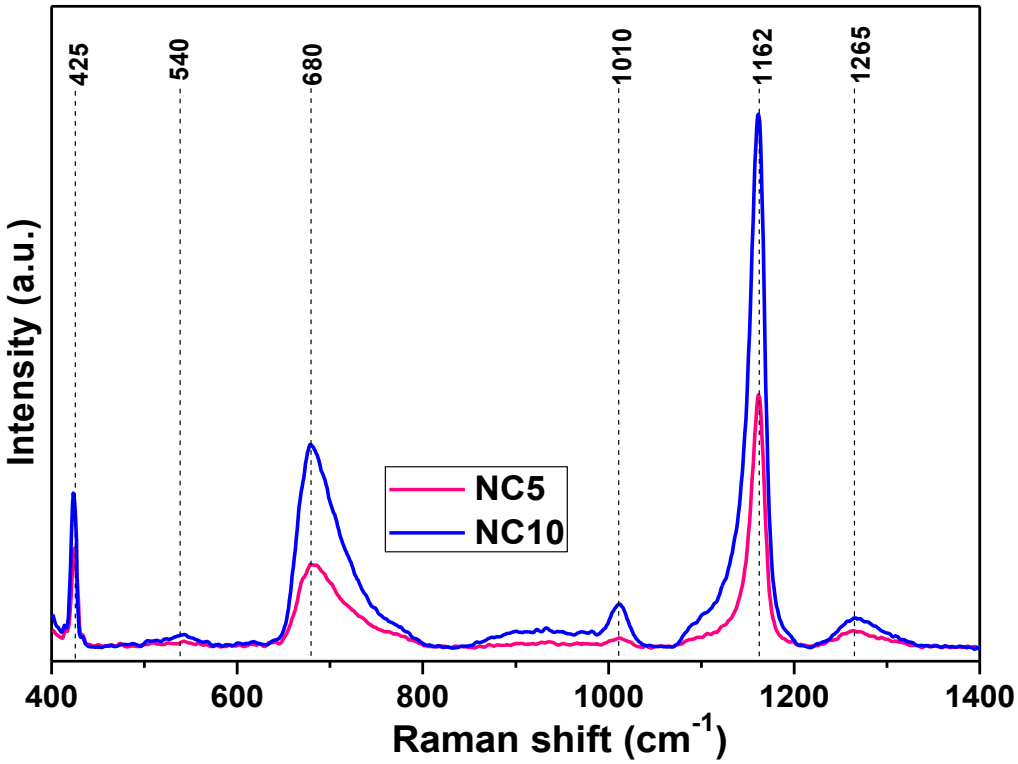

Fig. 4.2.4: Raman spectra of NC5 and NC10 glass samples.

Apart from this, the bands ~ 878 and 769 cm^{-1} are related to the different meta-phosphate groups and symmetric stretching vibrations of P-O-P bands, respectively **[12].** A small signature ~ 709 cm^{-1} is associated to the symmetric stretching in the P-O-P groups. The same signature is also observed as the ratio of Cu^{2+} is increased in the copper-phosphate glasses **[40].** In addition to this, an intense peak ~ 495 cm^{-1} is attributed to S-S stretching vibration in S_8 rings **[41].**

4.2.4. Raman analysis

The Raman spectra of NC5 and NC10 glasses in the frequency range of (400–1400) cm^{-1} are shown in Fig. 4.2.4. Both spectra are mainly composed of three strong and three weak bands. The first weak signature ~ 1265 cm^{-1} and first intense peak ~ 1162 cm^{-1} are associated to the asymmetric and symmetric stretching modes of PO_2 groups in Q^2 phosphate tetrahedra **[37, 38].** With CuS content, the band intensity ~ 1162 cm^{-1} increases dramatically which indicates that the covalency character in the P-O bond increases **[40].** The second small signature ~ 1010 cm^{-1} and second intense peak ~ 680 cm^{-1} are attributed to asymmetric stretching of P-O-P groups linked with small metaphosphate rings and stretching vibrations of the P=S mode, respectively **[19, 1].** A very small signature ~ 540 cm^{-1} with CuS content is observed in NC10 glass associated to the asymmetric stretching of PS_4^{3-} tetrahedral group which belongs to the high conducting Na_3PS_4 phase **[41].** Moreover, another band ~ 425 cm^{-1} is attributed to ortho-thiophosphate (PS_4^{3-}) units, which also belongs to the high conducting Na_3PS_4 phase **[42].** It is also observed that this band increases as CuS content increases from 5 to 10 mol%.

4.2.5. Electrical conductivity

A graph for NC5 and NC10 glasses in between Z' and Z'' are plotted and is presented in the Fig.4.2.5 (a) and (b). For these glasses, the value of resistance (R) is obtained from the intercepts of the semicircle on the real axis (Z').

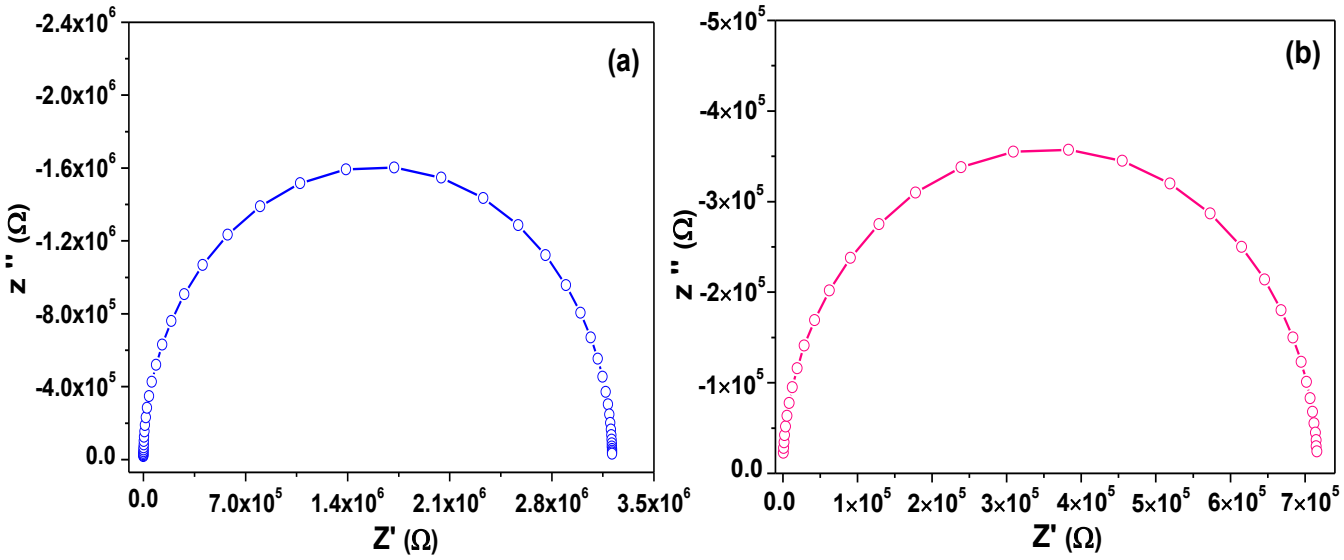

Fig. 4.2.5: Impedance spectra of (a) NC5 and (b) NC10 glasses at room temperature.

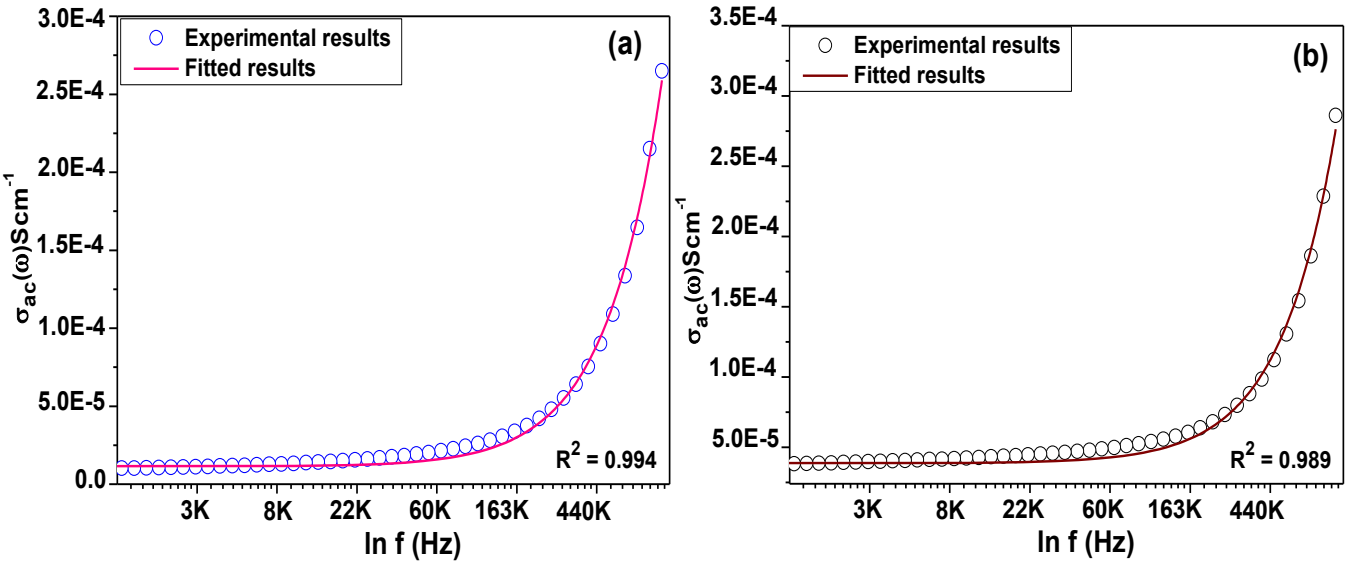

Fig. 4.2.6: Johnscher's plots of NC5 and NC10 glasses at room temperature.

Thereafter, the conductivity is calculated using the equation (4.7) and presented in the table 4.2.2. From Fig. 4.2.5 (a) and (b), it is observed that NC5 has more grain resistance as compared to NC10 glass sample. Consequently, NC10 glass sample exhibit higher electrical conductivity than NC5 glass. In the present glasses, to separate out the ac and dc conductivity Johnscher's power law was used. Equation (4.8) was used to fit the room temperature ac conductivity data and calculated the dc conductivity.

Table 4.2.2: Grain resistance, dc and ac conductivity at room temperature and other fitting parameters for NC5 and NC10 glass samples.

Sample	R_g (Ω) $\times 10^5$	σ_{ac} $\times 10^{-4}$ (Scm^{-1})	$\sigma_{dc} \times 10^{-5}$ (Scm^{-1})	$B \times 10^{-13}$	s	R^2
NC5	0.32	2.65	1.12	7.42	1.42	0.994
NC10	7.15	2.86	3.85	5.71	1.44	0.989

While fitting, the values of *B* and *s* were varied at the same time to get best fits. The fitted graphs for NC5 and NC10 glasses are shown in the Fig. 4.2.6 (a) and (b). After fitting, *dc* conductivity, parameter *B* and the value of exponent *s* were calculated and are presented in the table 4.2.2. It is observed from table 4.2.2 that NC10 glass exhibits high ionic conductivity than NC5 glass. Previously, in the $45P_2S_5$-$55Na_2S$ glass composition, the electrical conductivity observed was ~ 9.45×10^{-7} Scm^{-1} at room temperature. The addition of CuS content in the $45P_2S_5$-$55Na_2S$ glass composition increases the overall conductivity three orders higher than the base glass at room temperature.

4.3. $xNa_2O+(100-x)P_2O_5$; $(40 \leq x \leq 55)$

4.3.1. X-ray analysis

Fig. 4.3.1 shows the XRD patterns of NP1, NP2, NP3 and NP4 glass-ceramic samples. These samples have been obtained after heat treatment of as prepared glasses at 410 °C, 395 °C, 380 °C and 365 °C for 4h, respectively. The X-ray diffraction pattern indicates that two crystalline phases are present in all the samples. Sample NP1 exhibit mainly two crystalline phases having major phase of $Na_2H_2P_2O_7$ (ICDD No. 00-010-0192) and minor phase of $NaPO_3$ (ICDD No. 00-002-0436), respectively. As the amount of Na_2O content increases in the initial glass composition, the volume fraction of the $NaPO_3$ crystalline phase increases at the cost of $Na_2H_2P_2O_7$ phase. However, the observed peaks in the XRD were slightly shifted towards higher angle. This shift in XRD pattern indicates the presence of some amount of strain.

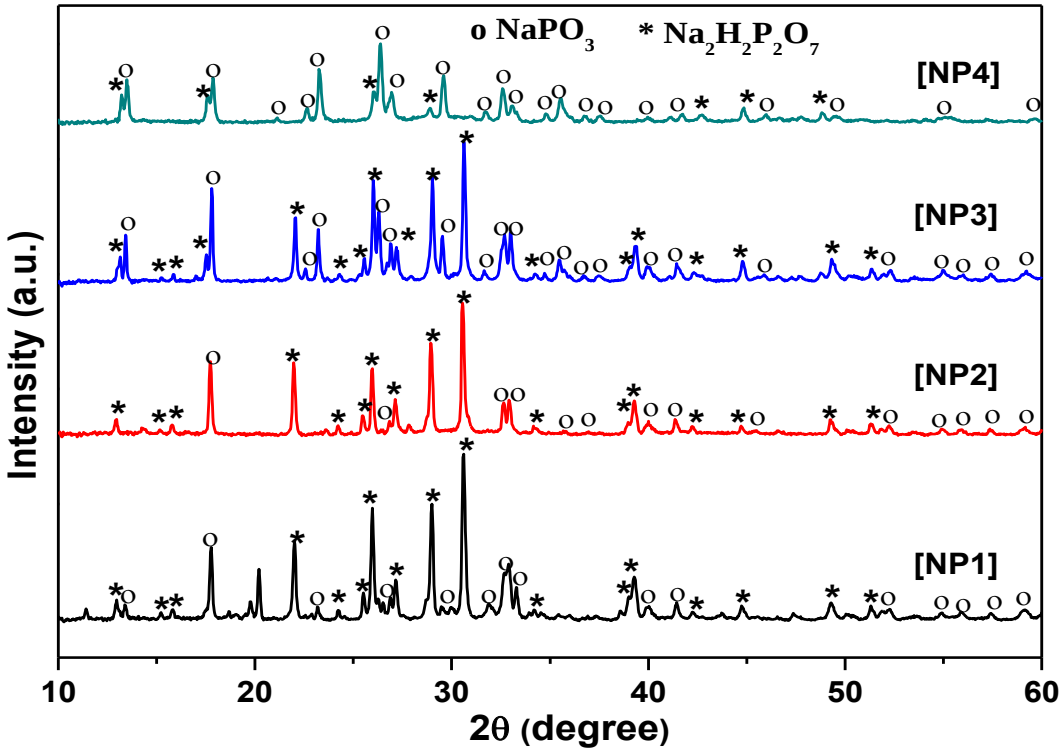

Fig. 4.3.1: XRD pattern of NP1, NP2, NP3 and NP4 glass-ceramic samples.

Basically, during heat treatment, the various species react with each other to form crystalline phase (stable) within glass matrix. The strain is calculated using equation (4.11) as given below **[43]:**

$$\varepsilon = \frac{\beta_{hkl}}{4tan\theta} \tag{4.11}$$

where, ε stands for strain, β_{hkl} for FWHM and θ for Bragg angle. Fig. 4.3.2 shows the variation of strain with mol % of Na_2O content. From table 4.3.1, it can be seen that with higher content of Na_2O, strain values decreases from 4.1 to 3.2 for $NaPO_3$ crystalline phase. It indicates that modifier (Na_2O) in glasses enhances the formation of $NaPO_3$ phase with respect to $Na_2H_2P_2O_7$.

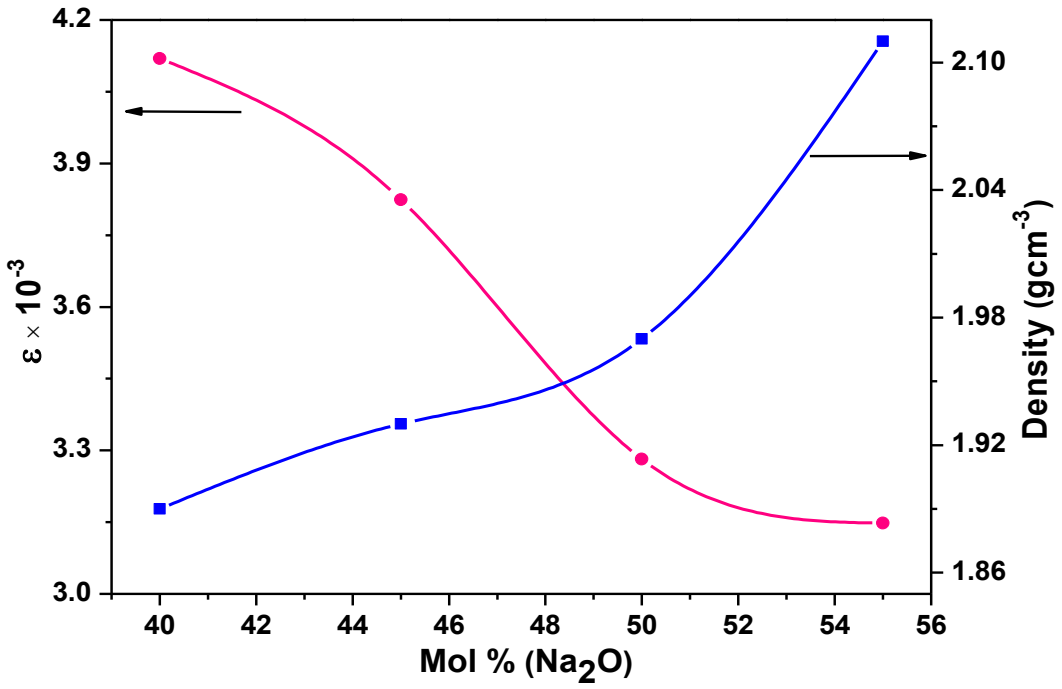

Fig. 4.3.2: Variation of strain for $NaPO_3$ phase and density with mol % of Na_2O content.

Secondly, $Na_2H_2P_2O_7$ phase is less symmetric and thermally stable than $NaPO_3$ phase **[44].** In case of silicate based glasses, it is well reported that initially SiO_2 (glass former) segregates during heat treatment. Thereafter, with passage of time some other cations modify the initial structure and formed the crystalline phases depending upon, time, temperature and initial constituents of the glasses **[45].**

4.3.2. Density analysis

Fig. 4.3.2 also shows the variation of density with mol % of Na_2O for xNa_2O-(100-x)P_2O_5 glass-ceramic system. The value of density increased from 1.89 to 2.11 gcm^{-3}; with the gradual increase of the Na_2O content. It is a manifestation of sodium oxide, which acts as modifier and causes the formation of non-bridging oxygen ions (NBOs) in the phosphate matrix. The NBOs are responsible for weakening the glass network **[46].** So, in the present case, sodium ions are linked to the surrounding oxygens by ionic bonds, which are weaker than the P-O bond. Thus, the structure of sodium phosphate glass-ceramic is always weaker than the other phosphate glass-ceramics. As the Na_2O content increases, the number of non-bridging oxygens also increases. This results in a compact structure with less polymerization due to the shortened chain, which may cause a decrease in the volume of the network structure and simultaneously, the reason for an increase in the value of density. Secondly, it is also associated with the density of crystalline phases formed during heat treatment. It is observed from XRD results that the volume fraction of $NaPO_3$ phase increases with Na_2O content. The observed $NaPO_3$ phase has higher density (ρ = 2.18 gcm^{-3}) as compared to $Na_2H_2P_2O_7$ (ρ = 1.86 gcm^{-3}) phase. So, higher NBOs and higher $NaPO_3$ phases are responsible for increasing density with Na_2O contents. The calculated densities for all samples are presented in table 4.3.1.

Table 4.3.1: Density, micro-hardness and strain of sodium-phosphate glass-ceramics.

Sample label	Density (gcm^{-3})	Micro Hardness (MPa) ± 5	Strain (10^{-3})
NP1	1.89	82	4.119
NP2	1.93	100	3.824
NP3	1.97	275	3.282
NP4	2.11	918	3.148

4.3.3. FTIR analysis

Fig. 4.3.3 shows the FTIR spectra of NP1, NP2, NP3 and NP4 glass-ceramics in the frequency region (400-2000 cm^{-1}). It is a well-known phenomenon that as the modifier content increases in the phosphate matrix, probable phosphate structural unit changes from $Q^3 \rightarrow Q^2 \rightarrow Q^1 \rightarrow Q^0$. The possible mechanism of Na_2O (modifier) with P_2O_5 (glass former) to satisfy the equilibrium equation can be written as:

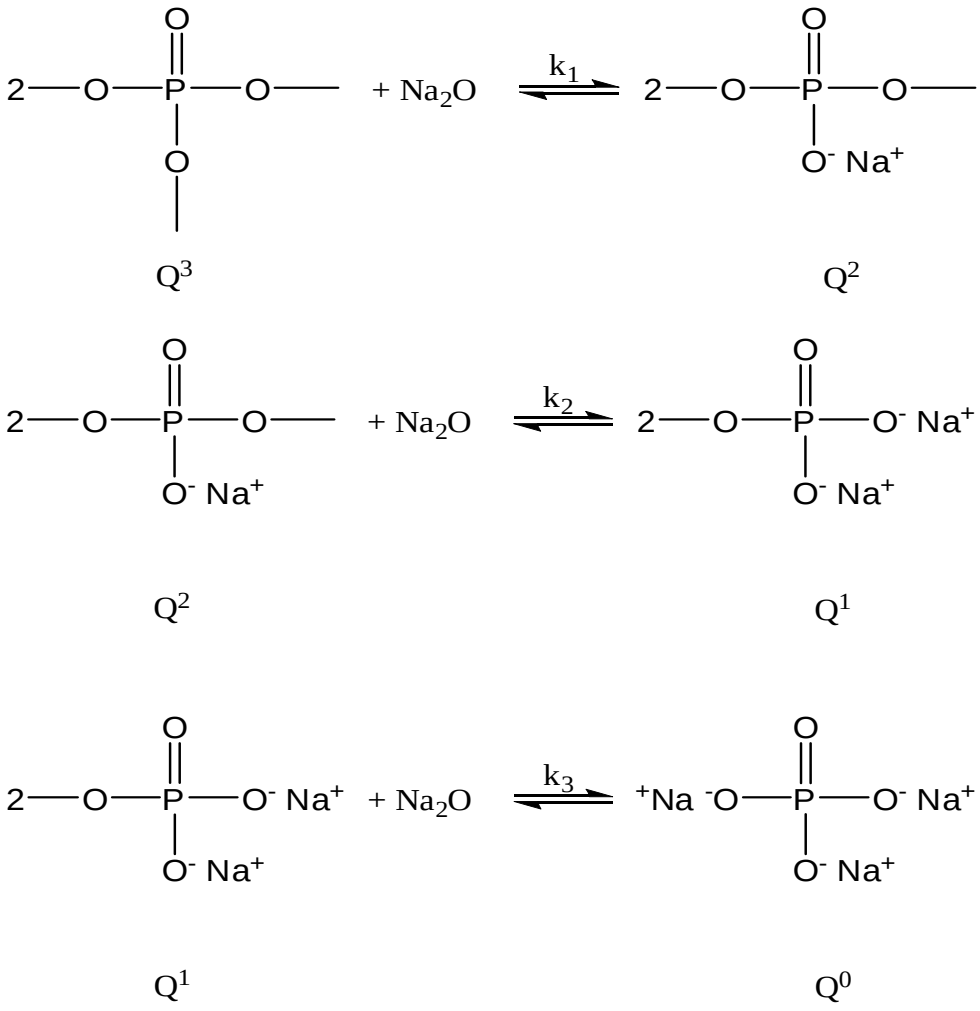

where, k_1, k_2 and k_3 are the equilibrium constants. This conversion of structural units from Q^3 to Q^0 generally provides NBOs which form rigid structures with less polymerization due to the shortened micro-molecule chain length. As observed from Fig. 4.3.3, there are nearly fifteen bands present in all the samples. They have main characteristics of the phosphorus–oxygen

networks. A very small signature in all samples ~ 1633 cm^{-1} might be due to presence of small amount of water absorbed from air during the preparation of pellets or due to the H_2O bending vibrations **[9].** The broad-band ~ 1294 cm^{-1} designate to the asymmetric stretching of the doubly bonded oxygen vibration, i.e. ν_{as} (P=O) **[47]**, while that at 1317-1334 cm^{-1} is associated to the harmonics of the above band **[48].** It is well reported by Bridge *et al.* **[48]** that the PO_4 units generally have two non-bridging bonds along with two bridging oxygen bonds such as P-O- and P=O, which are in resonance with each other. Therefore, in all the spectra splitting of bands ~ (1294-1334 cm^{-1}) is observed. It indicates that the P=O bond is strongly localized in the central phosphate groups. In the 650-1280 cm^{-1} spectral range, the present samples show three bands specific to meta-phosphate groups.

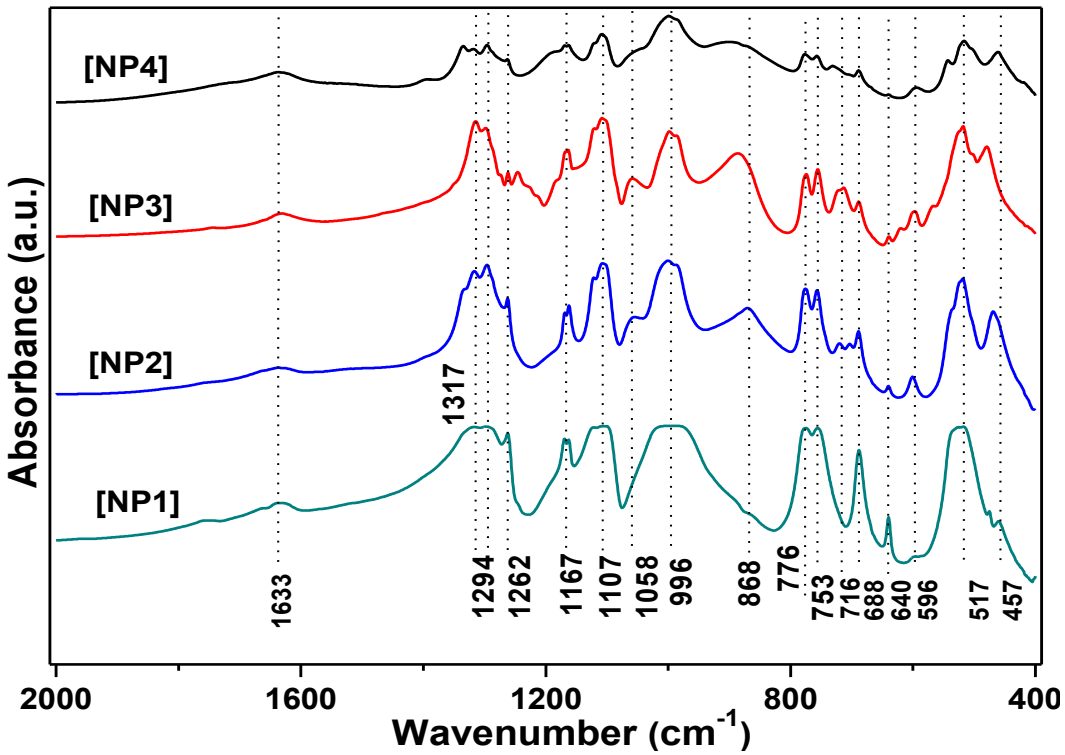

Fig. 4.3.3: FTIR spectra of the NP1, NP2, NP3 and NP4 glass-ceramic samples.

The first band ~ 1262 cm^{-1}, attributes to the symmetric stretching of the P=O terminal oxygen (Q^2 tetrahedra); the second band observed ~ 1167 cm^{-1}, attributes to the symmetric stretching mode of O-P-O non-bridging oxygens indicating the formation of Q^2 phosphate tetrahedra and

third one located at about ~ 688 cm^{-1} attributes to symmetric stretching of P-O-P mode vibration in the long-chain phosphate groups (Q^2 units) **[49, 50].** The bands ~ 1107 cm^{-1} and ~ 868-898 cm^{-1} are assigned to the symmetric stretching vibrations of PO_3 groups (Q^1 structural units) and asymmetric stretching of P-O-P groups, respectively **[51].** The absorption band ~ 868-898 cm^{-1} designate that the phosphate group is built from short chains containing phosphorus-oxygen and pyrophosphate groups ($P_2O_7^{4-}$). These observed bands fall in between the value observed in sodium pyrophosphate (940 cm^{-1}) and in $NaPO_3$ chains (865 cm^{-1}). Furthermore, a shift of the band from 868 → 898 cm^{-1} with increasing Na_2O content, reflects the de-polymerization of longer chain into shorter chains and formation of Q^1 structural units (pyrophosphate) **[52].** The band ~ 1058 cm^{-1} is assigned due to the motion of the non-bridging oxygens (PO_3) in Q^1 tetrahedra, while the band ~ 996 cm^{-1} is attributed to the symmetric stretching mode of non-bridging oxygens in Q^0 tetrahedra **[53].** The intensity of the band around 996 cm^{-1} increases with increasing Na_2O content at the cost of the band at ~ 1058 cm^{-1}, which reflect the conversion of Q^1 structural units to Q^0 structural units that are taking place **[54]**. At lower frequency, the bands ~ 753 cm^{-1} and 776 cm^{-1} are characteristics of symmetric stretching vibrations of P-O-P groups in Q^1 structural units, whereas the band ~ 716-728 cm^{-1} attributed for symmetric stretching of P-O-P linkages in between Q^1 and Q^2 structural units **[55].** An increase in intensity of the band ~ 716-728 cm^{-1} at the expense of bands ~ 753 cm^{-1} and 776 cm^{-1} may be a sign of the conversion of Q^2 structural units to Q^1 structural units that is occurring with increasing Na_2O content. The broad IR feature ~ 517 cm^{-1} and a small signature ~ 640 cm^{-1} are assigned to the bending vibration O-P-O modes **[56].** In addition to this, bands ~ 457-477 cm^{-1} and ~ 596 cm^{-1} correspond to the P−O−P bending vibration and stretching of P-O-P mode, respectively **[56, 57].**

Table 4.3.2: FTIR bands of NP1, NP2, NP3 and NP4 glass-ceramic samples.

NP1	NP2	NP3	NP4	Assignments	
457	468	477	460	P−O−P bending vibration	[59]
517	517	517	517	Harmonics of δ(P=O) modes	[59]
596	596	596	596	Stretching of P-O-P mode	[60]
640	640	640	640	δ(O-P-O) units	[59]
688	688	688	688	v_s(P-O-P) in the long chain of (Q^2 units)	[53]
-	716	718	728	v_s(P-O-P) linkages in between Q^1 and Q^2 units)	[58]
753	753	753	753	v_s(P-O-P) in Q^1 units	[58]
776	776	776	776	v_s(P-O-P) in Q^1 units	[58]
-	868	883	898	v_{as}(P-O-P) groups	[54]
996	996	996	996	v_s of NBOs in Q^0 tetrahedra	[56]
-	1058	1058	1058	Motion of NBOs (PO_3) in Q^1 tetrahedra	[56]
1107	1107	1107	1107	v_s of PO_3 groups (Q^1 units)	[54]
1167	1167	1167	1167	v_s(O-P-O) of NBOs in Q^2 tetrahedra	[53]
1262	1262	1262	1262	v_s(P=O) in Q^2 tetrahedra	[52]
1294	1294	1294	1294	v_{as}(P=O) modes	[50]
1317	1318	1317	1334	Harmonics of v_{as}(P=O) modes	[51]
1633	1633	1633	1633	H_2O bending vibrations	[49]

The shift in band from 457 → 477 cm^{-1} indicates the change in pyrophosphate group (Q^2) to orthophosphate group (Q^1). With an increase in Na_2O content, the modification in phosphate structures can be understood further because of change in terminal charge density at an anionic site **[58].** These changes in phosphate structures appear because of sodium ions, which generally provide ionic cross-linking between non-bridging oxygens of groups. This cross linking further increases the bond strength**.** Therefore, the strength and density of samples with Na_2O content increases as also discussed in other sections. The observed IR assignments at different frequencies are presented in table 4.3.2.

4.3.4. Raman analysis

The obtained Raman spectra in the frequency range between (400-1600) cm^{-1} for all glass-ceramic samples are shown in Fig. 4.3.4. All the spectra are mainly composed of four strong and ten weak Raman signatures. The most intense band ~ 1174 cm^{-1} along-with the small peak ~ 1160 cm^{-1} in all the samples correspond to the symmetric stretching vibrations of PO_2 groups (Q^2 structural units) **[52, 13].** On the other hand, the less intense peaks ~ 1275 and ~1287 cm^{-1}

are attributed to asymmetric stretching modes of PO_2 groups in Q^2 phosphate tetrahedra **[37].** The weak signature ~ 1331 cm^{-1} is associated to the presence of hydroxyl group (OH^-) or stretching vibration of surface-absorbed H_2O molecules **[59].** Another small signature ~ 1094 cm^{-1} corresponds to the formation of the terminal phosphate groups; PO_3^{2-} in Q^1 structural units **[39].** In addition to these bands, two weak signatures ~ 994 and 980 cm^{-1} are assigned to the PO_4^{3-} symmetric stretching modes in Q^0 structural units **[60, 61].**

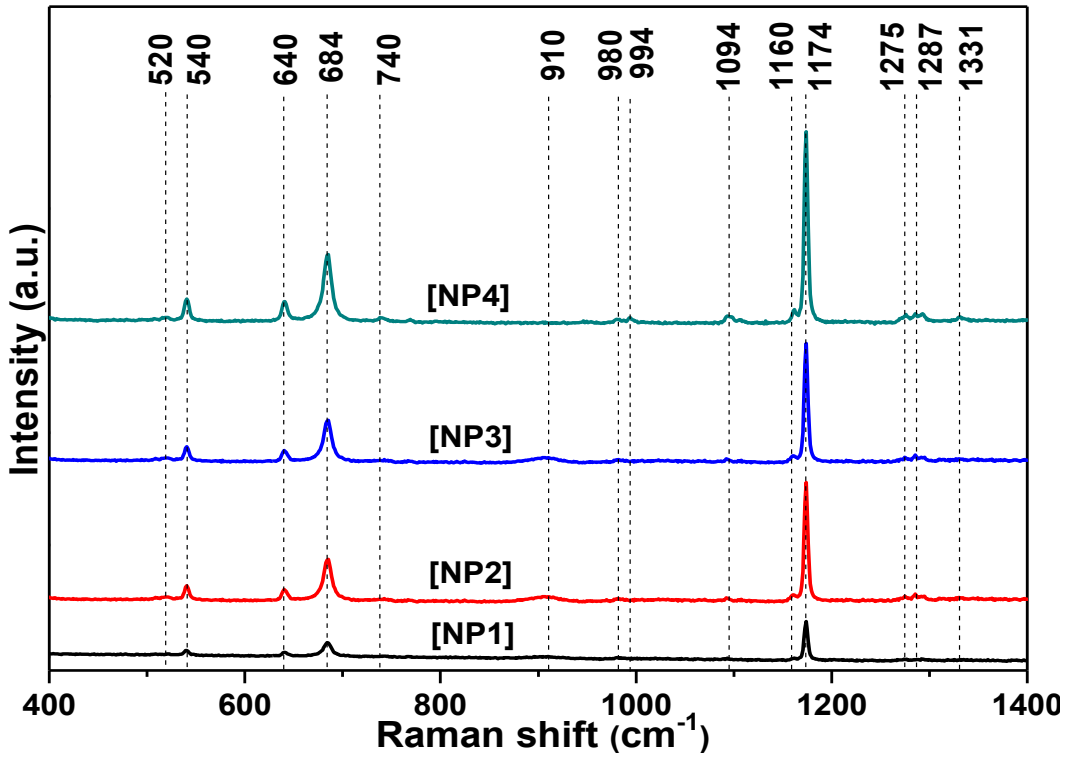

Fig. 4.3.4: Raman spectra of the NP1, NP2, NP3 and NP4 glass-ceramic samples.

The second intense peak ~ 684 cm^{-1} and small signature ~ 740 cm^{-1} are attributed to the symmetric stretching of P-O-P groups in Q^2 and Q^1 structural units, respectively **[50, 62].** The third intense peak ~ 640 cm^{-1} corresponds to bending vibration of O-P-O groups and a very small signature ~ 910 cm^{-1} is attributed to the symmetric stretching of P-O-P groups in Q^2 structural units **[56, 38].** The fourth intense peak ~ 540 cm^{-1} is described as a fundamental frequency of PO_4^{3-} groups or as harmonics of P=O bending vibrations and a less intense peak ~ 520 cm^{-1} is assigned as bending vibrations of $(P_2O_7)^{4-}$ groups **[40, 62].**

The Raman spectra of all the samples show increase band intensities with increasing concentration of Na_2O. It indicates that shorter chains or ring structures of the phosphate units increases with Na_2O concentration which acts as modifier and break the long chains **[63].** It is well known phenomenon that the strong band in the Raman spectra of a compound corresponds to weak band in the FTIR spectra and vice versa **[64].** The strong bands observed in FTIR ~753 cm^{-1} (Q^1 units) and ~ 1167 cm^{-1} (Q^2 units) are in well agreement with weak bands observed in Raman ~740 cm^{-1} (Q^1 units) and ~ 1160 cm^{-1} (Q^2 units). Moreover, in Raman a strong band ~ 684 cm^{-1} (Q^2 units) and a weak band ~ 994 cm^{-1} (Q^0 units) are in well agreement with a weak band ~ 688 cm^{-1} (Q^2 units) and a strong band ~ 996 cm^{-1} (Q^0 units). The above observations clearly indicate the de-polymerization of phosphate groups that changes $Q^2 \rightarrow Q^1 \rightarrow Q^0$ with Na_2O content, which is also supported by the FTIR results.

4.3.5. Mechanical properties

The ultrasonic wave velocities measured in the present samples are found to be sensitive to the glass composition as given in table 4.4.3. It is observed from table 4.3.3 that as the Na_2O content increases, consequently, both of the longitudinal (V_L) and shear (Vs) velocities increases. Fig. 4.3.5 and table 4.3.3 show the variation of elastic moduli with different mol % of Na_2O. Longitudinal modulus (L) was observed to vary from 25.6 to 28.9 GPa whereas, shear modulus (G) from 6.53 to 8.10 GPa. In both the cases, marginal variation is observed. It clearly indicates that the present system is more or less isotropic in nature. It is possible due to presence of glass matrix and polycrystalline nature of the glass-ceramics. In addition to this, bulk modulus (K) varied from 16.8 to 18.2 GPa and Young's modulus (E) from 17.3 to 21.5 GPa. In general, ionic and covalent bonds are considered as strong bonds than metallic bonds.

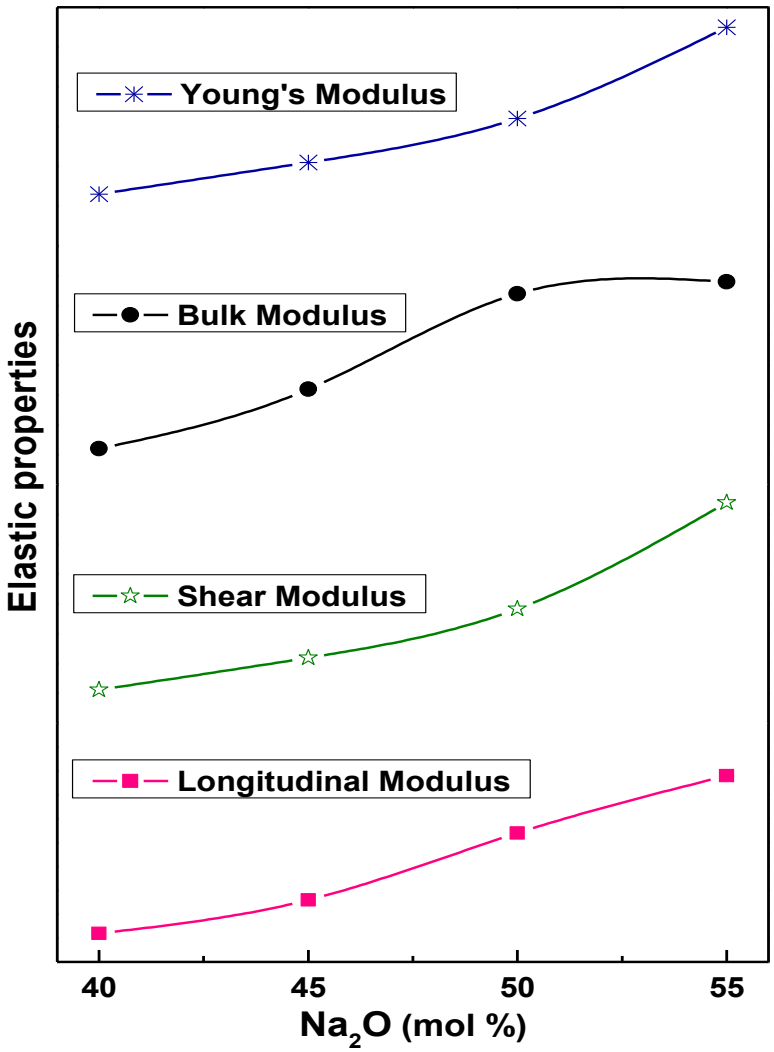

Fig. 4.3.5: Variation in Elastic constants for glass-ceramics at different mol % of Na_2O content.

Because of this reason glasses, ceramics and ionic crystals are hard and brittle in nature. In order to suppress the cracking of solid electrolytes, low and variable bond energy is required. It is only possible when glass is not converted completely into crystalline phases. The Young's moduli of present oxide glass-ceramics are in the range of 17.3 to 21.5 GPa. These values are lower than the conventional oxides (~ 50 GPa) and higher than organic polymers (~ 9 GPa). All the present samples have nearly comparable Young's moduli, which are well reported for the glass and glass-ceramics samples **[65].** Poisson's ratio is defined as the ratio between longitudinal and lateral strains produced under stress.

Table 4.3.3: Longitudinal velocity (V_L), shear velocity (Vs) and elastic constant values for NP1, NP2, NP3 and NP4 glass-ceramics.

Sample label	Longitudinal velocity V_L (ms^{-1})	Shear velocity Vs (ms^{-1})	Longitudinal modulus L (GPa)	Shear modulus G (GPa)	Bulk modulus K (GPa)	Young's modulus E (GPa)	Poisson 's ratio (V)
NP1	3680	1860	25.6	6.53	16.8	17.3	0.328
NP2	3707	1883	26.3	6.80	17.3	18.1	0.326
NP3	3772	1924	27.7	7.21	18.1	19.2	0.324
NP4	3823	2023	28.9	8.10	18.2	21.5	0.305

Fig. 4.3.6 shows the variation in Poisson's ratio for glass-ceramics that varied from 0.328 to 0.305 as the Na_2O content increases. It shows the highest value for NP1 and a lowest value for NP4 glass-ceramic samples, which is also summarized in table 4.3.3. It is well reported that as the Poisson's ratio decreases, the rigidity increases in glasses **[66]**. The rigidity is generally dependent upon the bond strength and cross-link density. The decrease in Poisson's ratio with an increase in Na_2O content is attributed to increasing the cross-link density and rigidity of glass-ceramics **[67].** Modi *et al.* **[68]** and Manupriya *et al.* **[69]** have also reported that a low cross-link density containing glass has higher Poisson's ratio i.e. 0.2 to 0.5. On the other hand, high cross-link density has Poisson's ratio between 0.1 and 0.2. Consequently, the present glass-ceramics contain low cross-link density.

4.3.6. Microstructure and hardness relationship

Fig. 4.3.6 also shows the variation in micro-hardness for different mol % of Na_2O. From table 4.3.1, it is observed that as Na_2O content increases the micro-hardness value increases from 82 MPa to 918 MPa. This phenomenon could be explained on the basis of density of glass-ceramics. Compact glasses generally have higher hardness. Table 4.3.1 show the density of glass-ceramic samples which increase from 1.89 to 2.11 gcm^{-3}. The indentation mark on the glass-ceramic samples taken under SEM is shown in Fig. 4.3.7 (a, b, c & d). The observed indentations clearly indicate that as Na_2O content increases, the diagonal length also decreases, which further supports to high density phases grown during heat treatment. In addition to this,

the microstructure developed in the glass-ceramics also influences the micro-hardness [**70].** It is a well-known phenomenon that mechanical properties of glass-ceramics depend upon the nucleated crystalline phase, their volume fractions, grain size, and shape of the crystals **[71].** The SEM micrographs of fractured surfaces for NP1, NP2, NP3 and NP4 glass-ceramic samples are presented in Fig. 4.3.8 (a, b, c & d).

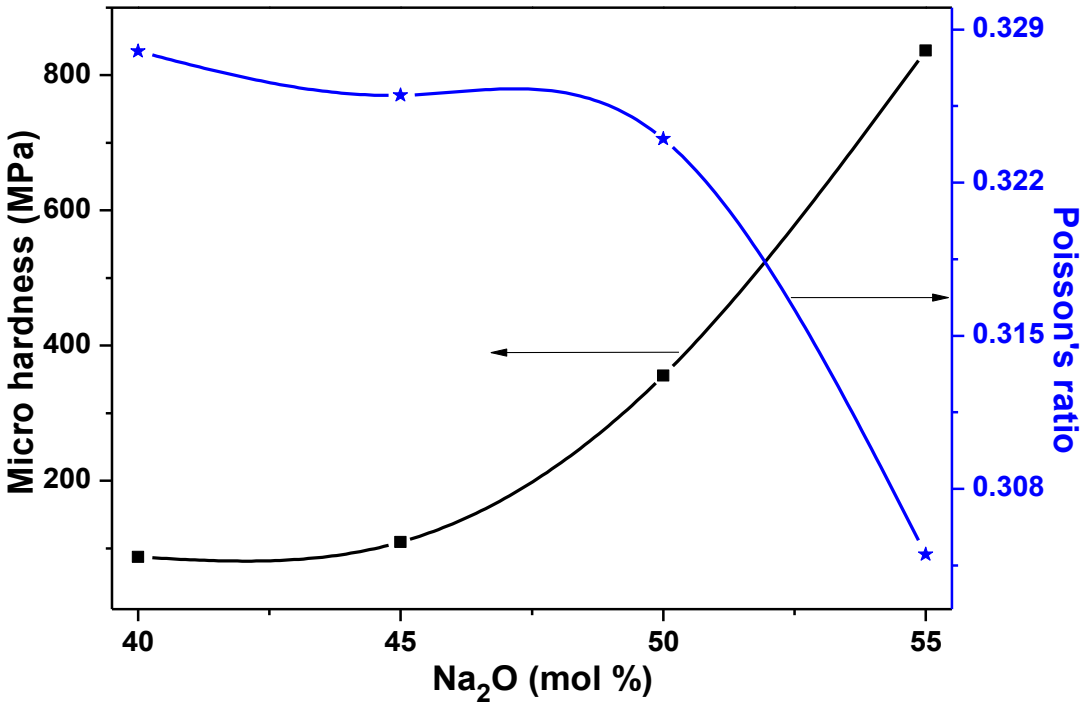

Fig. 4.3.6: Variation in Micro-hardness and Poisson's ratio with Na_2O (mol %).

The heterogeneous morphology is observed in all the samples, which supports the results of XRD. In all the micrographs, variation in shape and size of the grains are observed. For comparison, all the micrographs of the fractured surface of the samples are taken at same magnifications. The overall analysis of the structure reveals that a transition in microstructures exhibiting different crystalline phases occurs. Since, the amount of $NaPO_3$ phase increases as the content of Na_2O is increased. In Fig. 4.3.8 (a), NP1 sample exhibits two different types of morphology.

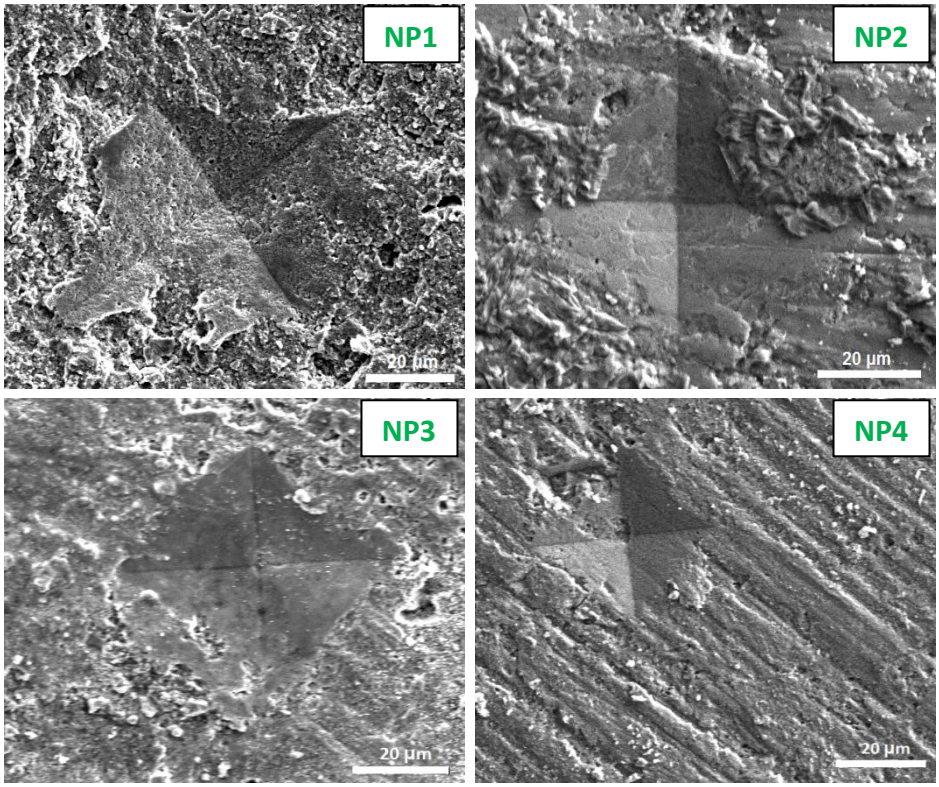

Fig. 4.3.7: SEM micrographs showing the indentation for NP1, NP2, NP3 and NP4 glass-ceramics.

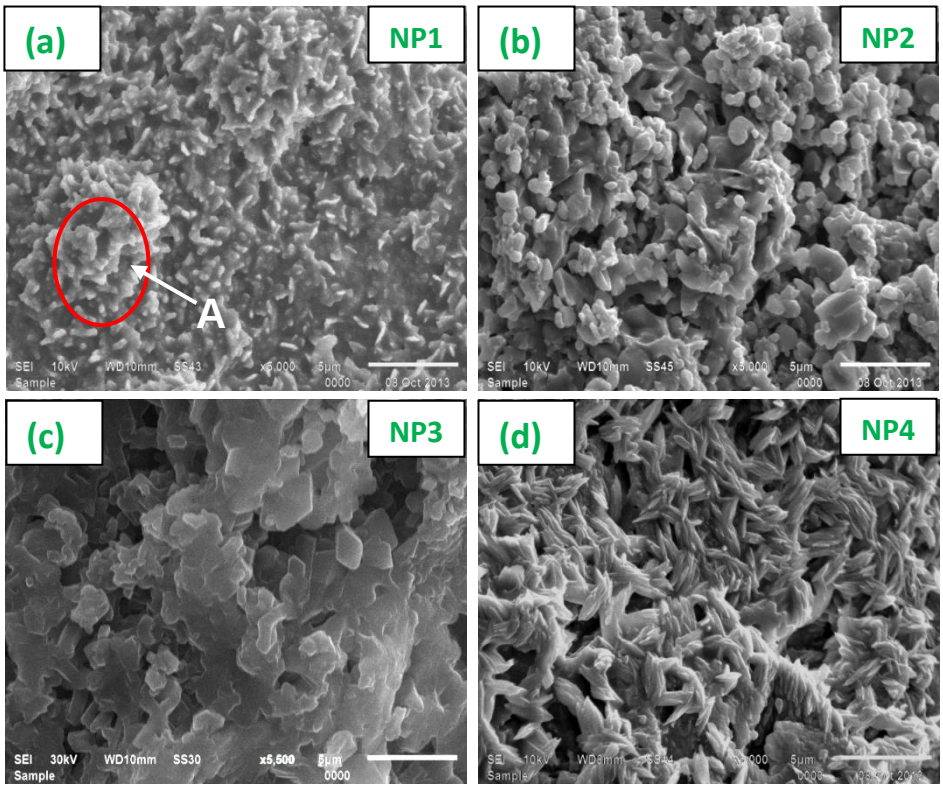

Fig. 4.3.8: SEM micrographs showing the variation in structure for NP1, NP2, NP3 and NP4 glass-ceramics.

One exhibiting to thicker morphology marked as A corresponds to $NaPO_3$ phase whose volume fraction observed from XRD is lower and the other exhibiting the elongated phase is for $Na_2H_2P_2O_7$. As the content of Na_2O increases the nucleated phase becomes thicker which is highest for NP3 sample, where the fully grown phase having faceted morphology can be seen in Fig. 4.3.8 (c). For NP4 sample, it is observed that the grown phase acquires brush type morphology and gets further refined. The flow pattern observed indicates that the liquid phase has migrated and has come out from the tip of the grown phases. It is related to the loss of the water molecules from the $Na_2H_2P_2O_7$ phase leading to formation of the higher amount of $NaPO_3$ phase as per following reaction:

$$Na_2H_2P_2O_7 \longrightarrow 2NaPO_3 + H_2O \qquad (4.12)$$

Moreover, few pores are also observed as can be in Fig. 4.3.8. These pores can be controlled by optimizing the heat treatment temperature and applied load during pellet preparation **[72].** From SEM micrographs, it is observed that sample NP4 exhibits interwoven structure along with network of fine needle-like interlocked crystals embedded in the glassy matrix. As reported by Ghaffari *et al.* **[73],** these interlocked crystalline phases create hindrance in propagation of cracks and further increase the toughness of the materials.

4.4. $55P_2O_5$-(45-x)Na_2O-xLi_2O; ($5 \leq x \leq 25$)

4.4.1. Density and molar volume

The experimental densities are calculated for all glasses and are presented in table 4.4.1. Theoretical values of density shows decreasing trend with Li_2O content. It is a well-known phenomenon that density decreases, because molecular mass of Li_2O (29.88 $gmol^{-1}$) is lower than that of molecular mass of Na_2O (61.97 $gmol^{-1}$). The measured density value decreases from 2.44 to 2.36 gcm^{-3} for NL15 to NL25 glasses, which are in well agreement with theoretical values and reported values **[74].** Basically, density is additive properties of the system and usually follows the mixture rule. In the present case, the Li_2O (2.01 gcm^{-3}) has less density than Na_2O (2.27 gcm^{-3}). So, the density decreases as the concentration of Li_2O increases from 15 to 25 mol %. However, the measured density increases from 5 to 15 mol % of Li_2O content. This anomaly might be related to the lower cross linking, which lead to high value of density. The variation of experimental density and molar volume with mol % of Li_2O for $55P_2O_5$-$x$$Na_2O$-(1-$x$)$Li_2O$; ($5 \leq x \leq 25$) system is shown in Fig. 4.4.1. It clearly indicates that Li_2O is a strong modifier than Na_2O. Moreover, the electronegativity of Li^+ (0.98) is more than Na^+ (0.93), which is responsible to compact the glass network and increases the density of glasses. As shown in Fig. 4.4.1, the molar volume also decreases with increasing content of Li_2O. It also indicates a compact structure with less polymerization due to the shortened chain, which may cause a decrease in the volume of the network structure and simultaneously, an increase in density. Overall, we can say that variation in density is observed because of mixed alkali effect.

Table 4.4.1: Experimental density and molar volume for all glass samples.

Sample label	P_2O_5	Na_2O	Li_2O	Density (gcm^{-3})	Molar volume (V_M)
NL5	55	40	5	2.37	183.24
NL10	55	35	10	2.40	180.77
NL15	55	30	15	2.44	179.17
NL20	55	25	20	2.41	177.57
NL25	55	20	25	2.36	175.96

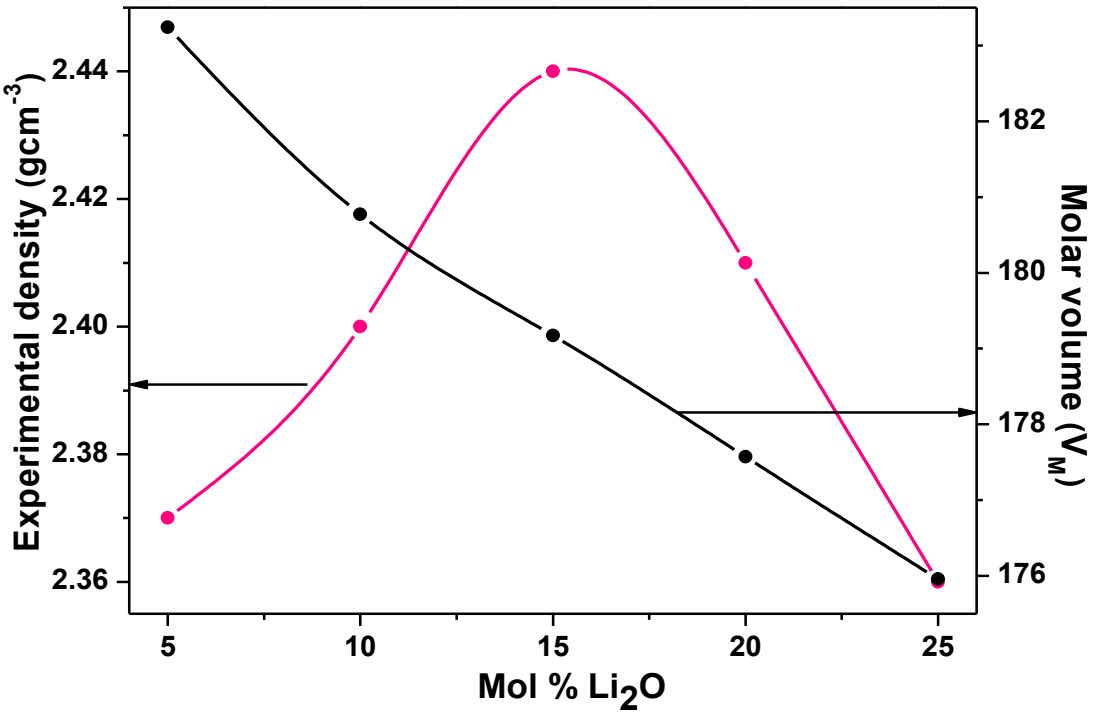

Fig. 4.4.1: Variation in density and molar volume at different Li_2O content.

Moreover, lithium-ion with higher field strength (0.21) attracts the oxygen ions more than sodium (0.17), leading to a decrease in the size of the interstices. The decrease in the size of the interstices supports the decrease in molar volume, which shows that glass network became compact leading to increased density.

4.4.2. Structural and thermal analysis

Fig. 4.4.2 shows the X-ray powder diffraction patterns of the as-quenched samples (NL5, NL10, NL15, NL20 and NL25) at room temperature. The presence of broad halo in range of 20º–30º for all the five samples indicates their amorphous nature. Moreover, the XRD patterns of all the glasses show only one broad halo indicating the absence of phase separation. In general, the presence of two network formers and modifiers leads to the formation of phase-separated glass. The DTA measurements at different heating rates; 10, 20, 30 and 40 $^{o}Cmin^{-1}$ in the temperature range 50-800 °C are carried out for all the glasses.

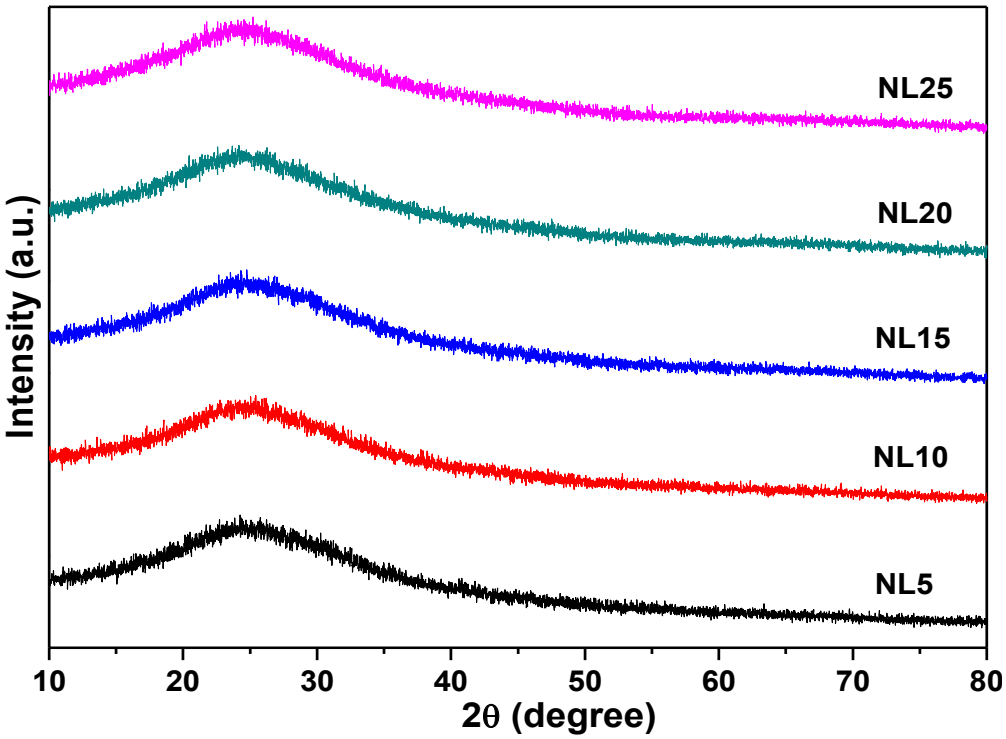

Fig. 4.4.2: XRD patterns of NL5, NL10, NL15, NL20 and NL25 glass samples.

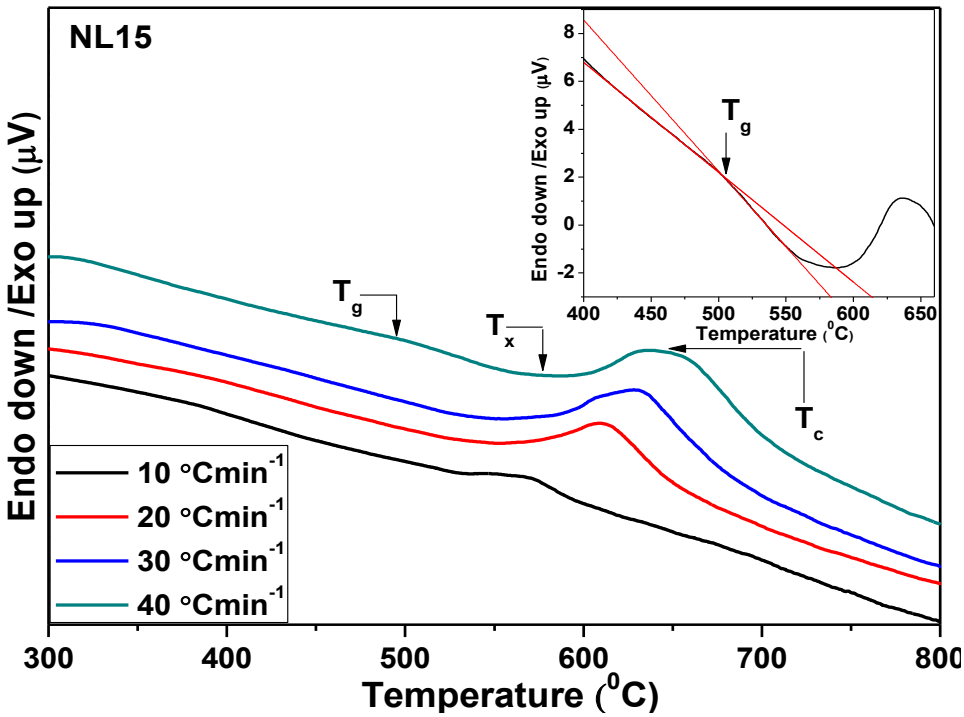

Fig. 4.4.3: DTA curve of NL15 glass sample at different heating rates.

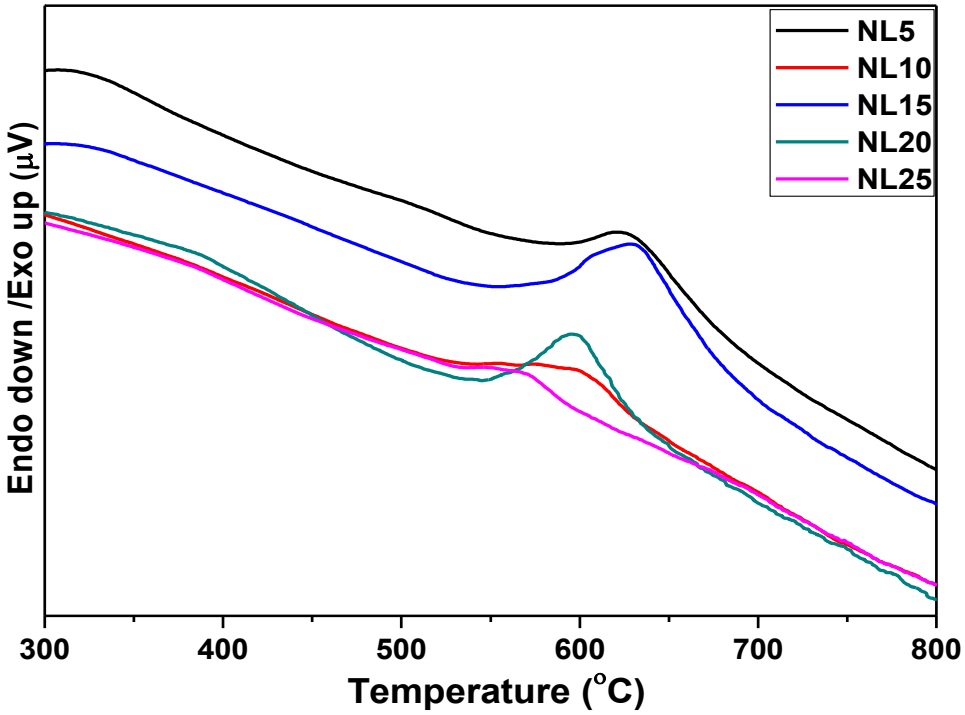

Fig. 4.4.4: DTA curve of NL5, NL10, NL15, NL20 and NL25 glass samples at heating rate of 30 $^{o}min^{-1}$.

Thermal analysis of these glasses is shown in Fig. (4.4.3) and (4.4.4). T_g, T_x and T_c of glasses was determined from the DTA curves is given in the table 4.4.2. DTA curves of all the samples were differentiated (DDTA), and maximum peak temperatures were assigned as inflection-point temperature (T_f). It is observed from table 4.4.2 that as the heating rate increases, the characteristic temperatures of glasses shifted towards higher temperatures. The increase in T_g with an increase in heating rate indicates the relaxation dynamics. Theoretically, T_g is defined as the temperature at which observed experimental time (τ_{obs}) is equal to the relaxation time (τ) i.e; $\tau_{obs} = \tau$. Furthermore, it is a well-known phenomenon at the same time, $\tau T_g = 1$ **[26].** Therefore, as the heating rate increases, correspondingly τ_{obs} decreases and hence T_g increases. The increase in crystallization temperature (T_c) with an increase in heating rates is related to viscous liquid that could not get sufficient time to nucleate and crystallize.

Table 4.4.2: Characteristics temperatures observed from DTA at different heating rates for NL5, NL10, NL15, NL20 and NL25 glass samples and stability parameter (ΔT).

Sample label	α (^{0}Cmin^{-1})	T_g (^{0}C)	T_x (^{0}C)	T_f (^{0}C)	T_c (^{0}C)	$\Delta T = T_c - T_g$ (^{0}C)	ΔT (Mean)
NL5	10	340	518	545	555	215	
	20	405	546	582	590	185	185
	30	445	566	611	622	177	
	40	469	583	620	632	163	
NL10	10	336	511	540	553	217	
	20	386	530	558	567	181	189
	30	414	552	586	595	181	
	40	445	570	610	625	180	
NL15	10	358	545	558	583	225	
	20	395	550	583	605	210	200
	30	422	561	615	632	210	
	40	498	580	624	650	152	
NL20	10	330	500	534	537	207	
	20	375	520	555	574	199	196
	30	402	545	591	598	196	
	40	429	562	604	610	181	
NL25	10	323	460	509	528	205	
	20	361	518	540	553	192	188
	30	395	540	577	572	177	
	40	424	560	592	600	176	

A typical DTA curve for NL15 sample at different heating rates is shown in Fig. 4.4.3. A typical graph for NL15 at 40 ^{o}Cmin^{-1} is also shown in inset in the Fig. 4.4.3. It is also observed from DTA measurements (table 4.4.2) that as the concentration of Li_2O increases from 5 mol % to 10 mol % and from 15 to 25 mol %, all the characteristic temperatures are found to decrease. In the present glasses, lithium oxide is acting as the network modifier, which creates non-bridging oxygens (NBOs). NBOs disrupt the long chains and break the chemical bonds causing a decrease in all the characteristic temperatures **[75].** However, from 10 to 15 mol % Li_2O, all the characteristic temperature increases. This phenomenon can be explained on the basis of nature of bonding present in the system. Basically, lithium has electronegativity (0.98) which is higher than sodium (0.93). As a result, P-O-Li and Li-O bonds formed within the glass matrix

might exhibit higher covalent character than P-O-Na and Na-O bonds **[76].** Wullen *et al.* **[77]** also reported that after an optimum limit of modifier (Li_2O) content**,** the LiO_n polyhedra approaches to each other and share common NBOs. Because of this, the structural changes lead to successive cross-linking of phosphate chains. Consequently, all the characteristic temperature increases. The above phenomenon can also be understood with the help of density and structural units obtained from FTIR, which shows changes with Li_2O concentration as explained in the following sections. A typical DTA graph for NL5, NL10, NL15, NL20 and NL25 glasses at a heating rate of 30 $^oCmin^{-1}$ is shown in Fig. 4.4.4. A parameter (ΔT) which corresponds to glass stability was obtained with the help of equation (4.5) at different heating rates and presented in table 4.4.2. The value of (ΔT) for NL15 is maximum, which indicates its highest thermal stability than other glasses. Furthermore, from table 4.4.2, it is also observed that as the heating rates increases from 10 to 40 $^oCmin^{-1}$ the value of (ΔT) for all glasses decreases. This phenomenon indicates that the glass samples are more stable at low heating rate as compared to high heating rate.

4.4.3. FTIR analysis

FTIR spectra of the glass samples NL5, NL10, NL15, NL20 and NL25 in the frequency range of 2000-400 cm^{-1} are shown in Fig. 4.4.5. The possible mechanism of Li_2O (modifier) with P_2O_5 (glass former) for phosphate structural units can be understood as follows:

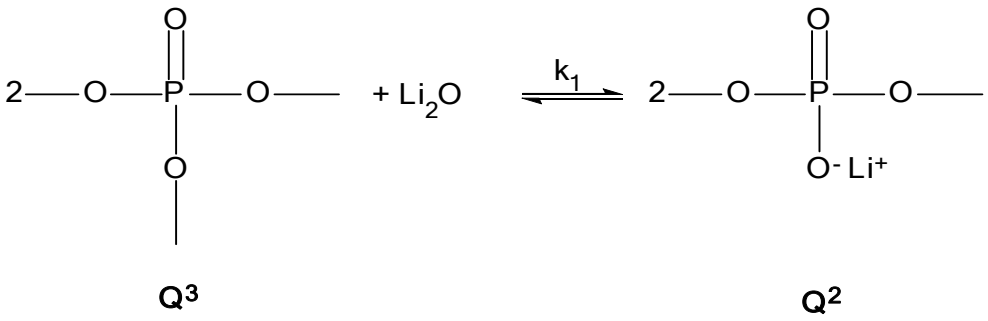

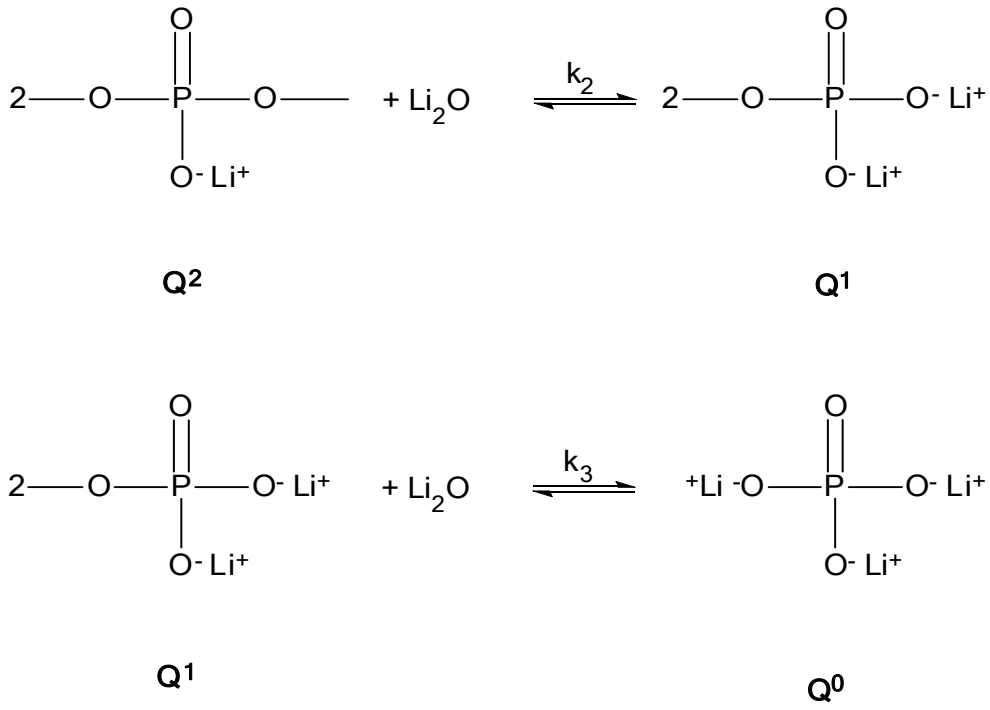

where, k_1, k_2 and k_3 corresponds to the equilibrium constants. The change in structural units from Q^3 to Q^0 usually provides NBOs with less polymerization, which forms rigid structures due to the shortened chain length. It is observed from Fig. 4.4.5 that there are nearly twelve bands present in all the glasses. They have main assignments of the phosphorus–oxygen and hydrogen–oxygen networks. The band in between 3425-3455 cm^{-1} and 2918-2930 cm^{-1} present in all the glass samples is associated with the oscillations of hydroxyl groups and stretching vibrations of P-O-H group in different structural sites, respectively **[78, 79].** A certain shift in these bands at lower region (3436 ⟶ 3425 cm^{-1}) and (2930 ⟶ 2918 cm^{-1}), designates the weakening of OH^- group in NL5, NL10 and NL15 glasses. On the other hand, the shift of these bands at higher region (3425 ⟶ 3455 cm^{-1}) and (2918 ⟶ 2930 cm^{-1}) designates the enhancement of OH^-, which has taken place in case of NL20 and NL25 glasses. A very weak band is also observed ~ 2854 cm^{-1} in NL10 glass. It is associated to the stretching vibrations of P-O-H group **[79].** Two weak bands and one intense band between 2365-2378 cm^{-1}, 2330-2348 cm^{-1}, and 1640-1643 cm^{-1} are also observed in all glasses, which is attributed to bending

vibration of H_2O molecules **[35, 36].** Interestingly, in NL10 glass an extra very small signature ~ 1380 cm^{-1} obtained are associated to the stretching modes of bridging oxyegen in P=O bond **[80].** This signature designates that the polymerization of phosphate groups is initiated. The band in between 1285-1290 cm^{-1} corresponds to the asymmetric stretching modes of PO_2 groups in Q^2 phosphate tetrahedra **[37].** As the Li_2O content increases, these band shifts from 1285 cm^{-1} to 1319-1330 cm^{-1}. The band in between 1319-1330 cm^{-1} is associated to the symmetric stretching of P=O bond in Q^3 structural units **[81].** This phenomenon indicates that as Li_2O content increases from 10 to 25 mol % some polymerization in the phosphate network as well as the decrease in the average bond length of P-O (NBOs) is taking place **[80].** Moreover, NL15 glass shows maximum intensity ~ 1319 cm^{-1} than other glasses, which confirms that the polymerization of phosphate network in NL15 sample, is maximum.

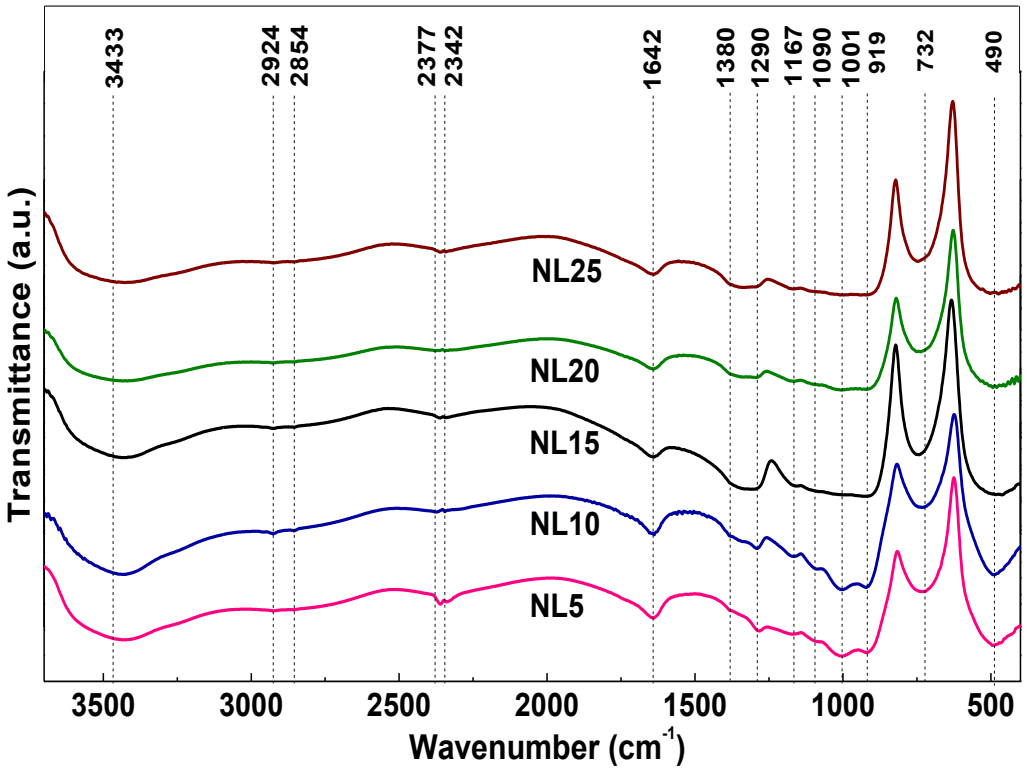

Fig. 4.4.5: FTIR spectra of the NL5, NL10, NL15, NL20 and NL25 glasses.

Table 4.4.3: FTIR bands of NL5, NL10, NL15, NL20 and NL25 glass samples.

NL 5	NL 10	NL 15	NL 20	NL 25	Assignments	
3436	3433	3425	3442	3455	Oscillations of hydroxyl groups	[78]
2930	2924	2918	2925	2930	Stretching vibrations of P-O-H group	[79]
----	2854	----	----	----	Stretching vibrations of P-O-H group	[79]
2365	2377	2365	2378	2366	δ (H_2O molecules)	[35]
2332	2342	2330	2332	2348	δ (H_2O molecules)	[35]
1643	1642	1640	1643	1641	δ (H_2O molecules)	[36]
----	1380	----	----	----	Stretching modes of bridging oxyegen in P-O	[80]
1285	1290	1319	1325	1328	v_{as} (PO_2 groups) in Q^2 units	[37]
1170	1167	1155	1166	1167	v_s (PO_2 groups) in Q^2 units	[38]
1094	1090	----	1096	----	Terminal groups; PO_3^{2-} in Q^1 structural units	[39]
1004	1001	----	1009	1118	v_s (PO_4^{3-} groups) in Q^0 structural units	[60]
920	919	914	925	914	v_s (P-O-P groups) in Q^2 structural units	[38]
728	732	743	737	749	v_s (P-O-P groups) in Q^1 structural units	[62]
492	490	476	491	497	δ (O-P-O groups)	[82]

This observation is also supported by density and molar volume of the glasses as discussed in section 4.4.1. The band at around 1155-1170 cm^{-1} is associated to the symmetric stretching modes of PO_2 in Q^2 structural units **[38].** Apart from this, two weak bands ~ 1094 cm^{-1} and 1004 cm^{-1} are also observed. These bands are due to the formation of the terminal phosphate groups; PO_3^{2-} in Q^1 structural units and the PO_4^{3-} symmetric stretching modes in Q^0 structural units, respectively **[39, 60].** It is observed that as Li_2O content increases from 5 to 10 mol %**,** these bands get shifted from (1094 $\longrightarrow$ 1087 cm^{-1}) and (1004 $\longrightarrow$ 997 cm^{-1})**,** and finally disappears in higher Li_2O content glasses (above NL15). In addition to this, the bands at around 914-925 cm^{-1} and 728-749 cm^{-1} are assigned to the asymmetric and symmetric stretching vibrations of P-O-P groups in Q^2 and Q^1 structural units, respectively **[38, 62].** It is also observed that glass NL15 exhibit maximum intensity ~ 743 cm^{-1}. This phenomenon further indicates that the polymerization of phosphate network is maximum in NL15 glass with higher bond strength **[60].** In addition to above bands, an intense band ~ 476-497 cm^{-1} correspond to the deformation modes of PO_4^{3-} groups and bending vibration of O-P-O groups **[82].** The FTIR band assignments of all glasses are presented in table 4.4.3.

4.4.4. Raman analysis

The Raman spectra of NL5, NL10, NL15, NL20 and NL25 glasses are shown in Fig. 4.4.6 in the frequency range between (400-1500) cm^{-1}. All the spectra are mainly composed of three strong bands. In addition to this, NL5 and NL15 glasses show extra bands ~ 1200 cm^{-1} and 804 cm^{-1}, respectively. It is observed from Fig. 4.4.6, all glasses show broad bands. This phenomenon indicates the formation of terminal phosphate groups, PO_3^{2-} **[39].** The first broad-band ~ 668 cm^{-1} and a small band ~ 804 cm^{-1} corresponds to the symmetric and asymmetric stretching of bridging oxygens (BOs) in the P-O-P groups, respectively **[83, 14].** The maximum relative area and maximum peak intensity at 668 cm^{-1} in glass NL15 confirms that the polymerization in the phosphate group is maximum, which is in well agreement with obtained FTIR results. The second broad-band ~ 1157 cm^{-1} is attributed to asymmetric stretching vibrations of P-O-P groups in Q^2 structural units **[53].**

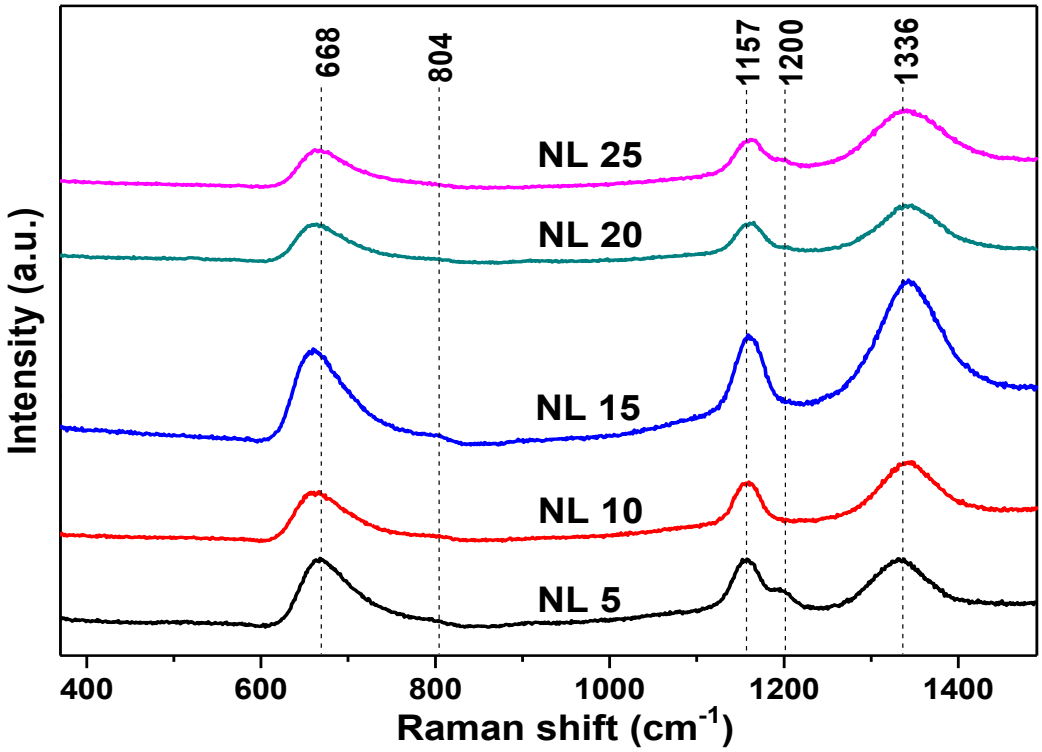

Fig. 4.4.6: Raman spectra of the NL5, NL10, NL15, NL20 and NL25 glasses.

With Li_2O content, this band shifted towards the higher-frequency region (1157 ⟶ 1165 cm^{-1}). This shift occurs because of change in bond length and bond angle between P-O-P **[84].** Furthermore, it is also observed that NL15 glass exhibits a higher intense peak as compared to other glasses. The occurrence of continuous de-polymerization of big structural units (Q^4 or Q^3) into small structural units (Q^2 or Q^1) could also be the reason of less intense peak in (NL5, NL10, NL20, NL25) and shift at higher frequency in this band. The third broad-band ~ 1336 cm^{-1} is associated with the asymmetric stretching of P=O bonds, while a very small signature ~ 1200 cm^{-1} in NL5 glass correspond to the symmetric stretching of P=O bonds **[12].** The above study further confirms that NL15 glass exhibits higher polymerization than other glasses.

4.4.5. Kinetics of phase transformations

The nucleation and growth of crystalline phases in a glassy matrix depend upon glass compositions and network rigidity. The different thermodynamic and kinetic parameters such as free energy, diffusion coefficient and interfacial energy between glassy and crystalline phases are also responsible for the controlled crystallization **[85].** During amorphous to crystalline phase transformation, two types of activation energies are evolved i.e. the activation energy for nucleation (E_n) and activation energy for crystal growth (E_G). In various studies, the activation energy for growth (E_G) is taken equal to the activation energy of whole crystallization (E_c) **[86].** The dependence of T_g under non-isothermal conditions (different heating rates) are explained using two approaches. The first approach is the estimation of glass transition activation energy (E_g) using Kissinger's model **[27].** Equation (4.4) was used to calculate the value of E_g. A plot of $\ln(T_g^2/\alpha)$ against $1000/T_g$ gives straight line is shown in Fig. 4.4.7 (a) for all compositions. From the slope of these straight lines, the value of the activation energy for glass transition (E_g) is calculated and presented in table 4.4.4.

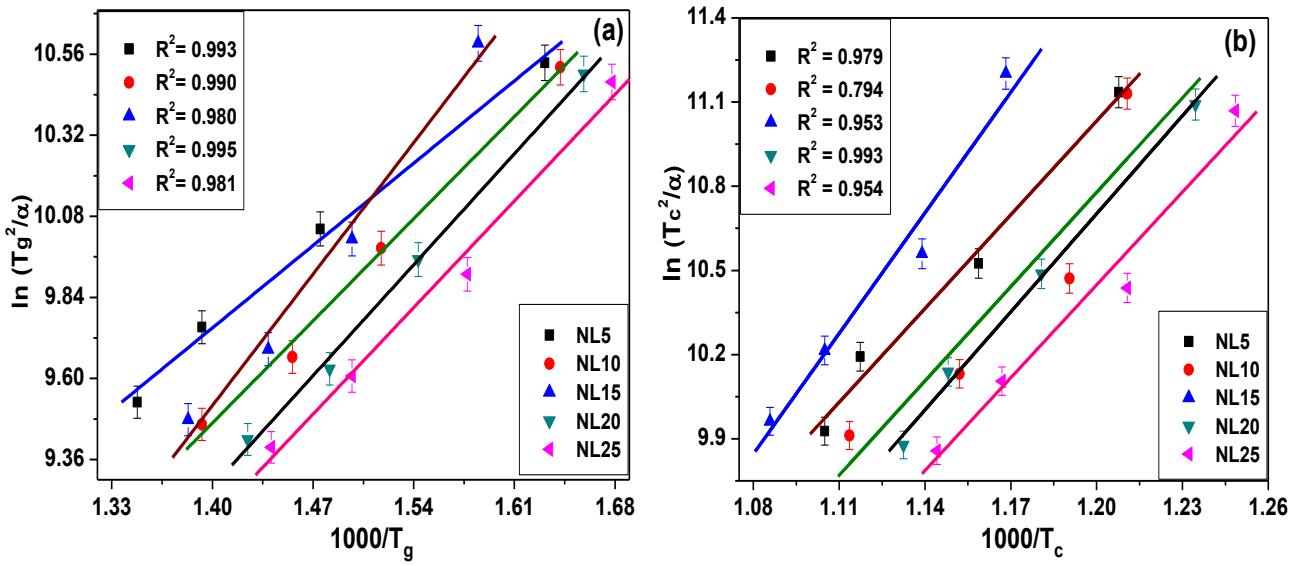

Fig. 4.4.7: (a) Variation of $\ln(T_g^2/\alpha)$ against $1000/T_g$ and **(b)** $\ln(T_c^2/\alpha)$ against $1000/T_c$ according to Kissinger formula for NL5, NL10, NL15, NL20 and NL25 glasses.

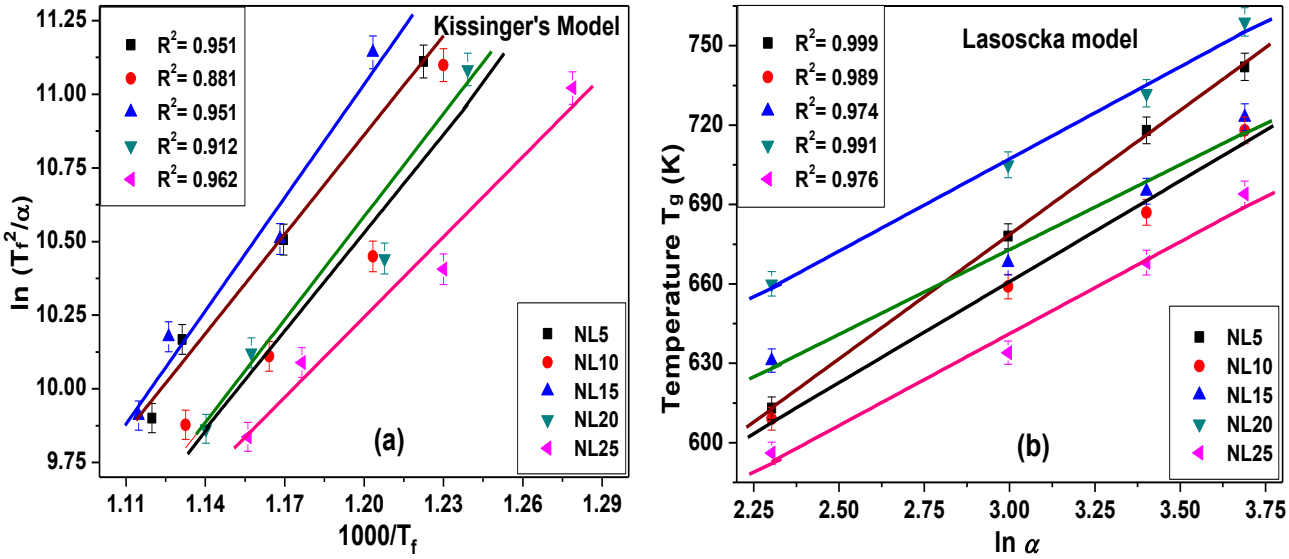

Fig. 4.4.8: (a) Variation of $\ln(T_f^2/\alpha)$ against $1000/T_f$ according to Kissinger's model and **(b)** variation of T_g (K) against $\ln\alpha$ according to Lasoscka model for NL5, NL10, NL15, NL20 and NL25 glasses.

The second approach is the estimation of Lasoscka parameters using following equation **[87]:**

$$T_g = A + B \ln \alpha \qquad (4.13)$$

where A is known as the T_g at defined heating rate (1 ^{o}Cmin^{-1}). B parameter depends upon the modifier content, glass compositions and quenching rate, which generally show different chemical nature.

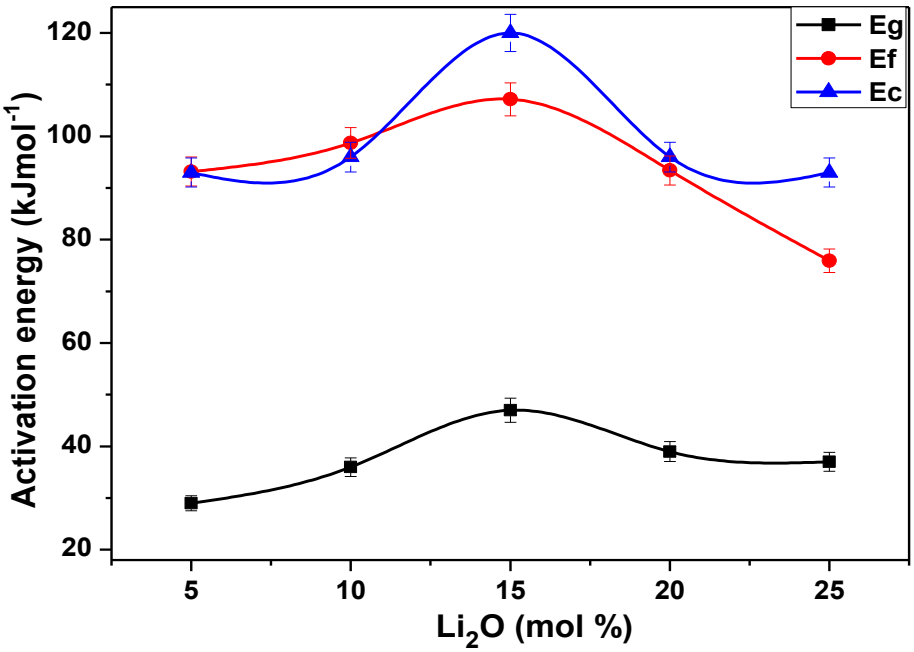

Fig. 4.4.9: Variation of mol % Li_2O with activation energies according to Kissinger formula.

Moreover, *B* gives the information about the various configurational changes, which occur near the glass transition region. The calculated value of *A* and *B* from Fig. 4.4.8 (b) is also presented in table 4.4.4 for all the glasses. It is observed from table 4.4.4 that NL15 glass shows the minimum value of B as compared to other glasses. The minimum value of *B* designates the configurational changes nearby T_g is minimum. This phenomenon further supports that NL15 glass has high thermal stability, which is also discussed in previous section. It is a well-known phenomenon that the crystallization mechanism in glasses takes place either internal (bulk) or through the surface. A broad peak shows surface crystallization, while a sharp DTA peak indicates bulk crystallization **[88]**. The nature of crystallization mechanism also depends upon modifier content, particle size of glass powder, heating rates and varies other factors **[89, 90].** In the present case, the effects of modifier content and heating rates on crystallization are clearly observed. The dependence of crystallization temperature (T_c) under non-isothermal condition is explained using two methods. The first method is the estimation of crystallization activation energy (E_c) using Kissinger's model **[27].**

Equation 4.4 was used to calculate the E_c for all glasses. For all compositions, a plot of $\ln(T_c^2/\alpha)$ against $1000/T_c$ gives straight line and is shown in Fig. 4.4.7 (b). From the slope of these straight lines, the value of the activation energy for crystallization (E_c) is calculated and listed in table 4.4.4. Also with the help of equation 4.4 a graph between $\ln(T_f^2/\alpha)$ and $1000/T_f$ is plotted and is shown in Fig. 4.4.8 (a). From the slope of the straight lines, the value of the activation energy for the inflection-point (E_f) is evaluated and summarized in table 4.4.4.

Secondly, Augis-Bennett method is used for the estimation of crystallization activation energy and frequency factor (v) by following equation **[91]:**

$$\ln [T_c/\alpha] = E_c/(RT_c) - \ln v \qquad (4.14)$$

where v is the crystallization frequency factor, which is defined as the number of attempts made by the nuclei to cross the energy barrier in 1 sec **[92].** Therefore, it gives the information about the available nucleation sites for crystal growth. Maximum value of ν indicates that the glass is the least thermal stable. Plots of $\ln(T_c/\alpha)$ against $1000/T_c$ are shown in Fig. 4.4.10 (a) for all glass compositions.

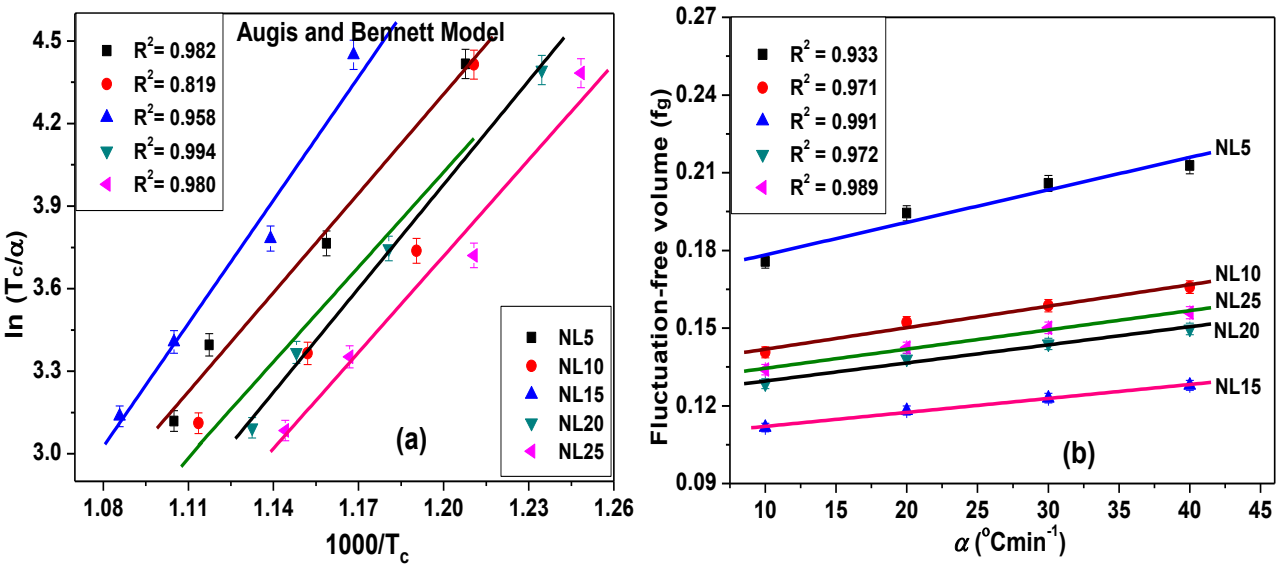

Fig. 4.4.10: (a) Variation of $\ln(T_c/\alpha)$ against $1000/T_c$ according to Augis-Bennett model and **(b)** variation of fraction of fluctuation-free volume different at heating rates for NL5, NL10, NL15, NL20 and NL25 glass samples.

By the least square fitting from the slope of these straight lines and intercepts, the values of the E_c and v are evaluated and listed in table 4.4.4. The value of v for NL15 sample is minimum, which indicates that the number of nucleation sites is less for crystal growth in this particular glass. The less nucleation sites for NL15 sample further indicate their high stability as compared to other glasses.

Apart from this, crystallization rate factors (K) have also been evaluated using following equations **[93]:**

$$K_f(T_g) = v\ exp[-(E/RT_g)\bullet(T_c - T_f)/T_f] \quad (4.15)$$

$$K_f(T_f) = v\ exp[-(E/RT_f)\bullet(T_c - T_f)/T_f] \quad (4.16)$$

$$K_f(T_c) = v\ exp[-(E/RT_c)\bullet(T_c - T_f)/T_f] \quad (4.17)$$

where T_f is known as the inflection point temperature. Crystallization rate factor (K) has great importance. Minimum value of K gives an indication of restriction for the crystallization, while the maximum value of K indicates very fast crystallization **[94].** With the help of equations 4.15, 4.16 and 4.17, the crystallization rate factors for T_g, T_f and T_c are evaluated at different heating rates and summarized in table 4.4.5. It is observed from table 4.4.5 that NL15 sample show minimum values of $K_f(T_g)$, $K_f(T_f)$ and $K_f(T_c)$ indicating their high thermal stability, which further supports the obtained results using different models. Using these models (Kissinger's Augis-Bennet) the activation energies for T_g, T_f and T_c are obtained and listed in table 4.4.4.

Table 4.4.4: The activation energies of all the samples using two different models, Lasoscka constants and crystallization frequency.

	Kissinger's Model			**Augis and Bennett Model**			**Lasoscka constants**	
Sample label	E_g	E_f (kJmol^{-1})	E_c	E_g	E_c (kJmol^{-1})	**Frequency v (s^{-1})**	**A (ºC)**	**B**
NL5	29	94	93	35	99	7.92×10^5	124	94
NL10	36	98	96	43	103	4.79×10^4	157	77
NL15	47	107	120	52	128	2.44×10^4	226	65
NL20	39	94	96	45	103	4.21×10^4	220	70
NL25	37	76	93	43	100	5.85×10^4	158	71

It is observed from table 4.4.4 that the activation energies obtained from different models are in well agreement with each other. However, the substantial differences between these activation energies are due to the use of different approximations followed for these models. A graph of activation energies versus mol % of Li_2O is shown in Fig. 4.4.9. The graph shows that as the concentration of Li_2O increases upto 15 mol % the activation energies for T_g, T_f and T_c also increases. The increase in activation energies can be understood on the basis of nature of bonding present in the glass which is already explained in section 4.4.2. However, in case of NL20 and NL25 glasses the activation energy decreases. It is well reported by Wers *et al.* **[95]** that with the addition of modifier content, the ionic character increase, which increases the de-polymerization and weakens the glass network structure. As a result, glass crystallizes at a lower temperature, which reduces the activation energies.

4.4.6. Fraction of fluctuation free volume (f_g) and bulk thermal expansion coefficients (α_f)

According to the theory, fluctuation-free volume (V_f) is defined as the sum of volume V_h of N_h fluctuation holes ($V_f = V_h N_h$). Where, V_h is the fluctuation hole of the volume attributed to local vibrational excitation. N_h is the number of fluctuation holes considered as the number of excited kinetic units responsible for a number of phenomena, including the glass transition **[96]**. According to Kaur *et al.* **[23]** after using above assumptions and other equations, the relation between E_g and fraction of fluctuation-free volume (f_g) can be written as follows:

$$E_g/RT_g = 1/f_g \qquad (4.18)$$

In general, thermal expansion is caused by the asymmetric nature of energy potential well **[4].** The asymmetric vibrations depend upon the chemical bonding, compositions and the temperature.

Table 4.4.5: Fluctuation-free volume, thermal expansion coefficients and crystallization rate constants for all glass samples.

Sample label	α (^{0}Cmin^{-1})	f_g	α_f × 10^{-4}	$K_f(T_g)$	$K_f(T_f)$	$K_f(T_c)$
NL5	10	0.1757	4.98	7.39×10^5	6.70×10^5	6.71×10^5
	20	0.1944	4.69	7.55×10^5	7.01×10^5	7.02×10^5
	30	0.2058	4.53	7.46×10^5	6.77×10^5	6.78×10^5
	40	0.2127	4.43	7.44×10^5	6.69×10^5	6.71×10^5
NL10	10	0.1406	4.53	4.28×10^4	3.80×10^4	3.83×10^4
	20	0.1522	4.35	4.46×10^4	4.11×10^4	4.13×10^4
	30	0.1587	4.25	4.48×10^4	4.15×10^4	4.17×10^4
	40	0.1658	4.15	4.32×10^4	3.82×10^4	3.85×10^4
NL15	10	0.1116	3.87	1.86×10^4	1.53×10^4	1.47×10^4
	20	0.1181	3.78	1.96×10^4	1.66×10^4	1.60×10^4
	30	0.1229	3.71	2.09×10^4	1.85×10^4	1.80×10^4
	40	0.1279	3.64	1.98×10^4	1.66×10^4	1.60×10^4
NL20	10	0.1285	4.37	4.09×10^4	3.99×10^4	3.99×10^4
	20	0.1381	4.22	3.56×10^4	3.07×10^4	3.08×10^4
	30	0.1439	4.13	3.97×10^4	3.78×10^4	3.78×10^4
	40	0.1497	4.05	4.02×10^4	3.85×10^4	3.85×10^4
NL25	10	0.1339	4.52	4.88×10^4	4.40×10^4	4.17×10^4
	20	0.1425	4.38	5.23×10^4	4.89×10^4	4.71×10^4
	30	0.1501	4.26	5.54×10^4	5.35×10^4	5.25×10^4
	40	0.1559	4.17	5.47×10^4	5.24×10^4	5.12×10^4

Usually, at the high temperature, the presence of more loosely bonded chemical units and a fast cooling rate increases the thermal expansion. On the other hand, a low temperature, a rigid network and annealing led to low thermal expansion. The change in thermal expansion coefficient (α_f) upon heating is related with an increase in the number of micro-voids (free volume) which are evaluated with the help of Frenkel equation **[97]**:

$$\alpha_f T_g = f_g \ln (1/f_g) \quad (4.19)$$

With the help of equations (4.18) and (4.19), at different heating rates, the values of f_g and α_f is evaluated and listed in table 4.4.5. It is observed from table 4.4.5; α_f and f_g are dependent on the glass compositions. NL15 glass exhibited the lower value of α_f and f_g as compared to other glasses. The lower value of f_g indicates that within glass, the degree of connectivity is higher, which leads to smaller free volume for the rearrangement of kinetic units. This phenomenon is

already discussed in FTIR analysis. The fraction of fluctuation-free volume with heating rates as shown in Fig. 4.4.10 (b). It is observed from table 4.4.5; the thermal expansion coefficient (α_f) for NL15 is lower. It indicates that the network of NL15 glass may have higher covalency that leads to smaller change in α_f than other glasses. It is also reported by Tiwari *et al.* **[52]** that the materials exhibiting strong bonds always show small change in α_f. On the other hand, other samples have high values of α_f, which shows lower covalency in bonds.

4.4.7. Electrical conductivity

A graph for NL15 glass in between Z' and Z'' are plotted and is presented in the Fig.4.4.11 (a). For this glass, the value of resistance (R) is obtained from the intercepts of the semicircle on the real axis (Z'). Thereafter, the conductivity is calculated using the equation (4.7). The obtained electrical conductivity for NL15 glass is ~ 17.4 × 10^{-5} Scm^{-1} at room temperature.

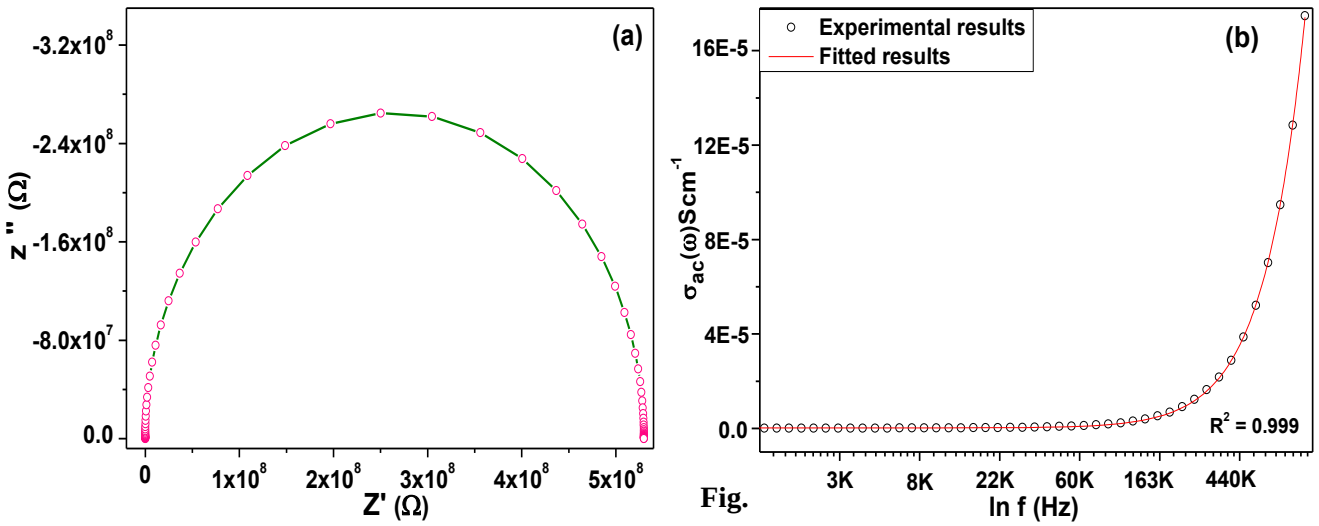

Fig.

4.4.11: (a) Impedance spectra and **(b)** Johnscher's plots of NL15 glass at room temperature.

In the present glasses, to separate out the ac and dc conductivity, Johnscher's power law was used. Equation (4.8) was used to fit the room temperature ac conductivity data and calculated the dc conductivity. The fitted graph for NL15 glass is shown in the Fig. 4.4.11 (b). After fitting, the dc conductivity for NL15 glass is observed ~ 18.2 × 10^{-7} Scm^{-1} at room temperature.

4.5. $55P_2O_5$-(45-*x*)Na_2O-*x*K_2O; ($5 \leq x \leq 25$)

4.5.1. Density and molar volume

For all glasses, the experimental densities are calculated and presented in table 4.5.1. Theoretical values of density shows increasing trend with K_2O content. It is a well-known phenomenon that density increases, because molecular mass of K_2O (94.20 $gmol^{-1}$) is higher than that of molecular mass of Na_2O (61.97 $gmol^{-1}$). The measured density value increases from 2.38 to 2.40 gcm^{-3} for NK5 to NK10 glasses and from 2.39 to 2.40 gcm^{-3} for NK15 to NK20 glasses, which are in well agreement with reported values and theoretical values **[98].** Basically, density follows the mixture rule which has additive properties in the multi-component systems. In the present case, the K_2O (2.35 gcm^{-3}) has high density than Na_2O (2.27 gcm^{-3}). So, the density increases as the concentration of K_2O increases from 5 to 10 mol % and 15 to 20 mol %. However, the measured density decreases, from 10 to 15 mol % and from 20 to 25 mol % of K_2O content. This inconsistency can be understood with the help of difference between the atomic radius.

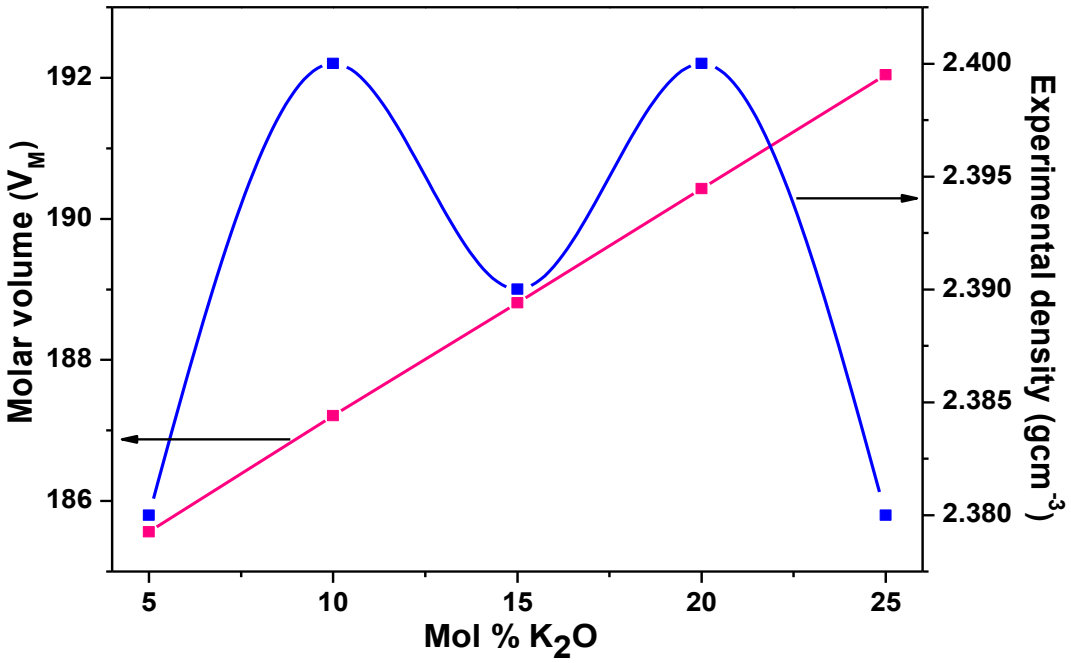

Fig. 4.5.1: Variation in density and molar volume at different K_2O content.

The density and molar volume of the samples depends on so many factors such as density of individual components as well as cross linking. The cross linking is responsible to change in the volume of the quenched samples. Furthermore, the cross linking also depends on the electronegativities of the components. In other words, it depends on the field strength of the modifiers (K_2O/Na_2O). So, density is the function of so many factors but marginally depends on the density of the individual components. Here K^+ (r = 1.38 Å) has higher atomic radius than that of Na^+ (1.02 Å). In present NK15 and NK25 glasses, K^+ is playing important role in the density instead of its higher atomic weight. Na^+ (0.971 gcm^{-3}) exhibits higher density than K^+ (0.862 gcm^{-3}) so with increase in K_2O content, the total volume of glass increases with the same atomic weight **[98].** Consequently, the value of density decreases. Moreover, the electronegativity of K^+ (0.82) is lesser than Na^+ (0.93), which is responsible for loose glass network and hence decreases the density of glasses. The variation of molar volume and experimental density with mol % of K_2O for $55P_2O_5$-(45-x)Na_2O-xK_2O; ($5 \leq x \leq 25$) system is shown in Fig. 4.5.1. As shown in Fig. 4.5.1, the molar volume also increases with increasing content of K_2O. It also indicates a loose structure with high polymerization due to the longer chain, which may cause an increase in the volume of the network structure and simultaneously, a decrease in density. The variation in densities in these glasses showed that these glasses have mixed alkali effect (MAE).

Table 4.5.1: Glass compositions, experimental density, molar volume (V_M), dilatometric (softening/glass transition temperature) for all glasses.

Sample label	P_2O_5	Na_2O	K_2O	Density (gcm^{-3})	Molar volume(V_M)	Softening temperature (T_s)/(^{0}C)
NK5	55	40	5	2.38	185.56	368 (T_g= 348)
NK10	55	35	10	2.40	187.21	392 (T_g = 359)
NK15	55	30	15	2.39	188.81	360 (T_g =345)
NK20	55	25	20	2.40	190.43	388 (T_g =368)
NK25	55	20	25	2.38	192.04	364 (T_g =338)

Moreover, potassium-ion with lower field strength do not attracts the oxygen ions more than sodium, leading to an increase in the size of the interstices. The increase in the size of the interstices supports the increase in molar volume, which shows that glass network became loosely packed and leading to decrease density.

4.5.2. Structural and thermal analysis

The X-ray powder diffraction patterns of the as-quenched samples (NK5, NK10, NK15, NK20 and NK25) are shown in Fig. 4.5.2. The presence of broad halo in between 15º–35º for all the five samples indicates their amorphous nature. Moreover, the XRD patterns of all the glasses show only one broad halo indicating the absence of any phase separation in the present glasses.

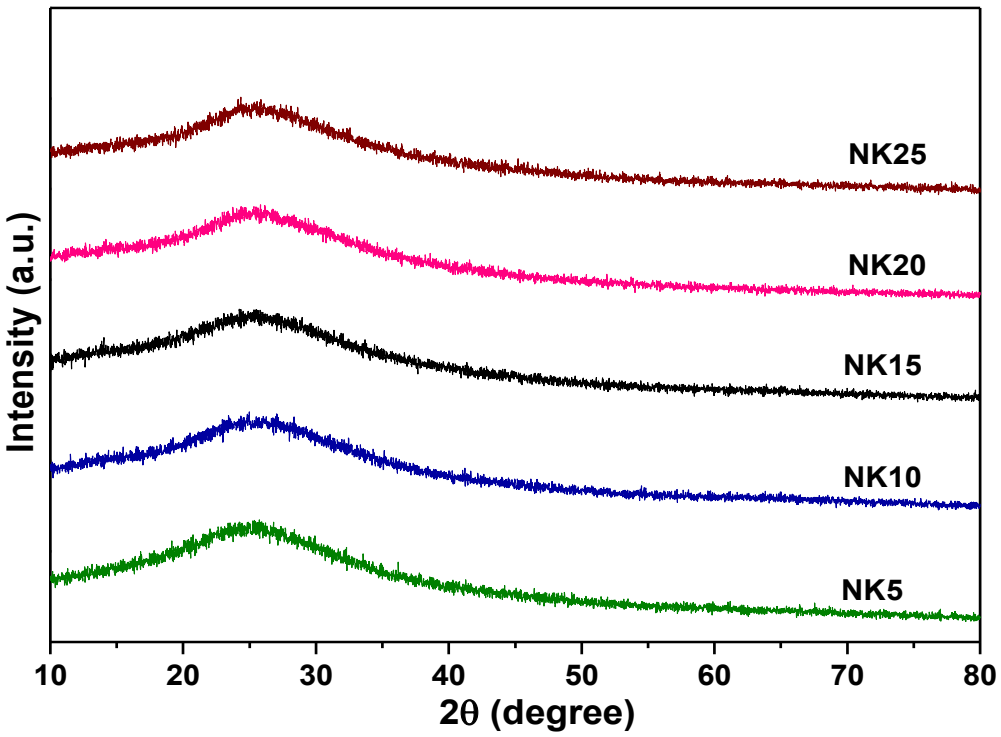

Fig. 4.5.2: XRD patterns of NK5, NK10, NK15, NK20 and NK25 glass samples.

The DTA curves of the glasses are shown in Fig. 4.5.3 and 4.5.4. The experiments were performed at different heating rates (20, 25, 30 and 35 ºCmin^{-1}) in the temperature range (200-800 ºC). From DTA curves, the value of T_g and T_c were determined and is given in the table 4.5.2. After differentiation of all DTA curves, the maximum peak temperatures were assigned

as inflection-point temperature (T_f). From table 4.5.2, it is observed that as the heating rate increases from 20 to 35 ºCmin^{-1} for all glasses, all the characteristic temperatures (T_g, T_f and T_c) shifted towards higher temperatures. Similar results have also been reported for silicate glasses **[23].**

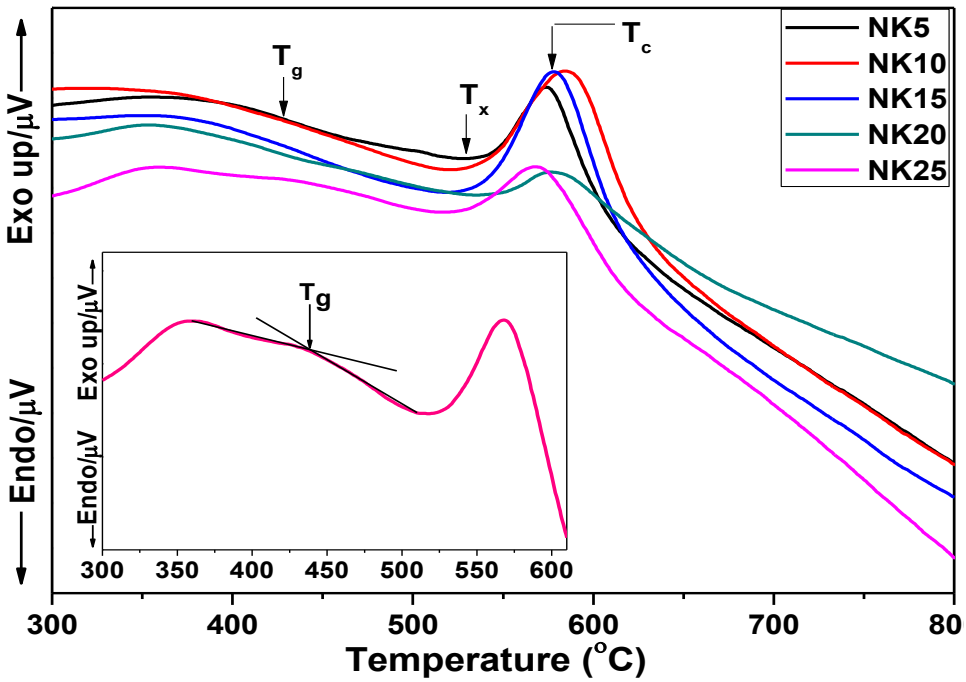

Fig. 4.5.3: DTA curve of NK5, NK10, NK15, NK20 and NK25 glasses at heating rate of 35 º min^{-1}.

With increase in heating rate, the increase in T_g indicates the relaxation dynamics phenomenon in all the glasses. This phenomenon is already discussed in the section 4.4.2. However, with an increase in heating rates, the increase in T_c is associated to viscous liquid which could not get sufficient time for nucleation and crystallization. A typical DTA curve for NK10 glass at 20, 25, 30 and 35 ºCmin^{-1} is shown in Fig. 4.5.4. It is observed from table 4.5.2 as the concentration of K_2O increases from 5 to 10 mol % and from 15 to 20 mol %, all the characteristic temperature increases.

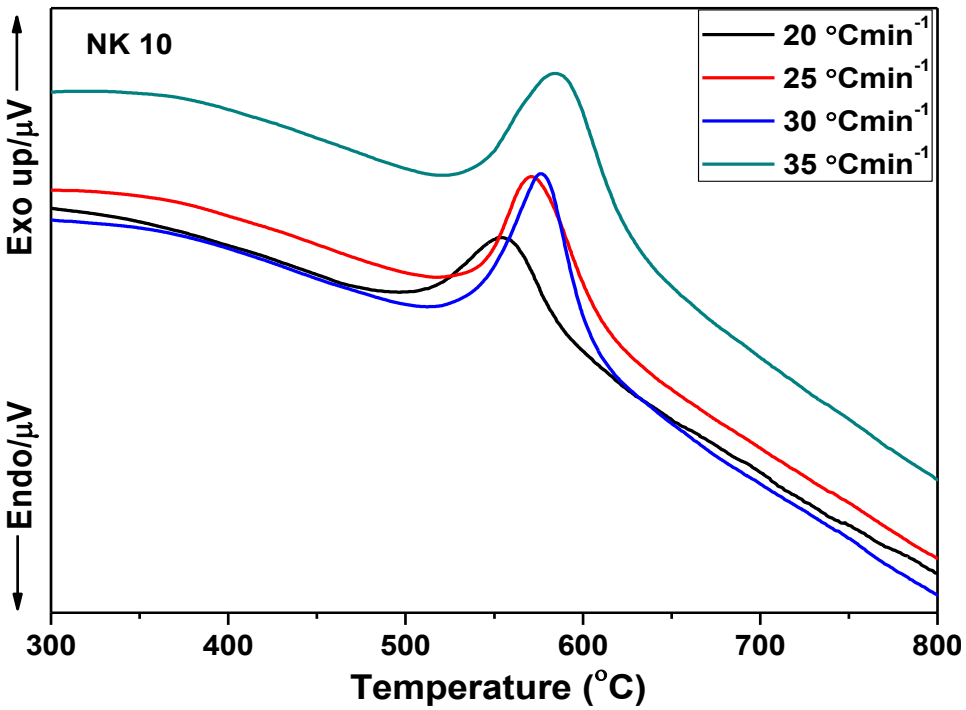

Fig. 4.5.4: DTA curve of NK10 glass sample at different heating rates.

The increase in T_g generally depends on the cross-link density, chain length of phosphate group and nature of bonding **[99]**. NK15 and NK25 glasses show decreasing trend in characteristic temperatures. As K_2O increases on the expense of Na_2O more and more non-bridging oxygen increases due to the increasing cleavage of P-O-P bonds to form less strong $P\text{-}O^{-}K^{+}$ bonds instead of more strong $P\text{-}O^{-}Na^{+}$ bonds **[100]**. Moreover, the ionic radius of K^{+} (r = 0.138 nm) > Na^{+} (r = 0.102 nm) and the field strength of K^{+} (0.13) < Na^{+} (0.17), thus increasing the K_2O content decreases the overall strength of phosphate glass network through the formation of weaker $P\text{-}O^{-}K^{+}$ bonds resulting a decrease in characteristic temperatures **[101].** The above phenomenon can also be understood with the help of structural units obtained from FTIR, which shows changes with K_2O concentration as discussed in the following sections. A typical DTA graph from 5 to 25 mol % of K_2O at a heating rate of 35 $^{o}Cmin^{-1}$ is shown in Fig. 4.5.3. A typical graph is also shown in inset for NK25 at 35 $^{o}Cmin^{-1}$ in the Fig. 4.5.3.

Table 4.5.2: Thermal constants observed from DTA at different heating rates for NK5, NK10, NK15, NK20 and NK25 glass samples and glass stability parameter (ΔT).

Sample label	α (^{0}C min^{-1})	T_g (^{0}C)	T_f (^{0}C)	T_c (^{0}C)	$\Delta T = T_c - T_g$ (^{0}C)	ΔT (Mean)
NK5	20	391	517	529	138	
	25	401	525	536	135	133
	30	423	548	555	132	
	35	445	565	574	129	
NK10	20	414	537	554	140	
	25	433	548	570	137	136
	30	444	554	578	134	
	35	456	572	588	132	
NK15	20	401	530	538	137	
	25	428	542	563	135	133
	30	442	550	575	133	
	35	452	568	580	128	
NK20	20	407	536	546	139	
	25	431	549	566	135	134
	30	445	561	578	133	
	35	456	572	584	128	
NK25	20	396	523	530	134	
	25	420	544	552	132	129
	30	434	552	560	126	
	35	448	561	573	125	

To check the glass stability, a parameter (ΔT) was calculated with the help of equation (4.5) at different heating rates and presented in the table 4.5.2. It is already discussed in previous section that the large difference in between T_g and T_c corresponds to the higher thermal stability in glasses. The values of (ΔT) for NK10 and NK20 glasses are maximum, which indicates their higher thermal stability. In these glasses, the effect of aggregation of Na^+ is partially diminished due to the decrease in Na^+ concentration. The complex role of Na^+ and K^+ cations might be responsible to create the anomalies in the present glasses. These results are also supported by dilatometeric study which is discussed in the next section 4.5.3. It is also observed from table 4.5.2, as the heating rates increases from 20 to 35 ^{o}Cmin^{-1} the value of (ΔT) for all glasses decreases. This phenomenon designates that as compared to high heating rate, the glass samples are more stable at low heating rate.

4.5.3. Dilatometric study

Dilatometric curves of NK5, NK10, NK15, NK20 and NK25 are shown in Fig. 4.5.5. The obtained softening temperature for all glasses is given in table 4.5.1. From these curves, T_g was also estimated and given in table 4.5.1. A typical graph is also shown in the Fig. 4.5.5 in inset for NK10 glass. All the glasses show almost linear behavior from RT to 320 ºC. The calculated T_g from dilatometer are observed to be lower than the DTA measurements. However, both the measurements follow the similar trend. The differences between DTA and dilatometer results are due to different heating rates i.e; 20 °Cmin^{-1} and 5 °Cmin^{-1}, respectively.

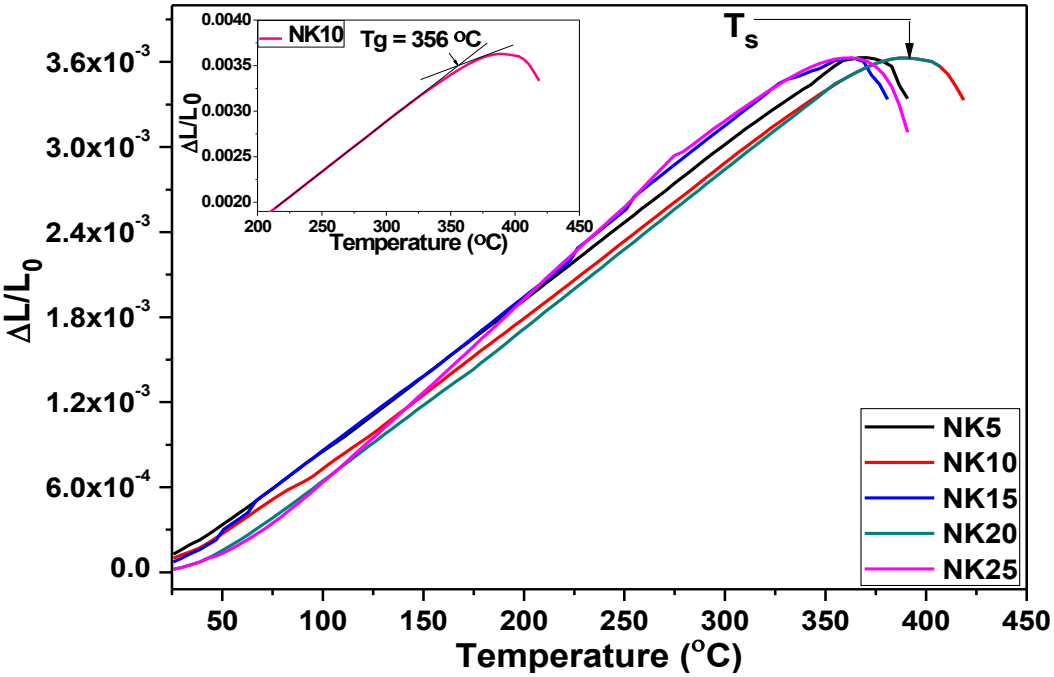

Fig. 4.5.5: Diltometric curve for NK5, NK10, NK15, NK20 and NK25 glasses.

It is well reported in the literature that lower heating rates decrease the characteristics temperatures as compared to higher heating rates **[102].** This is an inherent nature of the glass transition, which show sluggish relaxation phenomenon. Similar behavior has also been observed in the BaO-CaO-SiO_2 system **[103].** It is observed from dilatometeric study that softening point and T_g for NK10 and NK20 glasses are on higher side as compared to other

glasses as also observed in DTA measurements. The above results further confirmed that NK10 and NK20 glasses are more thermally stable than other glasses.

4.5.4. FTIR analysis

FTIR spectra of the glass samples NK5, NK10, NK15, NK20 and NK25 in the frequency range of 2000-400 cm^{-1} are shown in Fig. 4.5.6. The possible mechanism of K_2O (modifier) with P_2O_5 (glass former) in terms of change in structural units can be understood as follows:

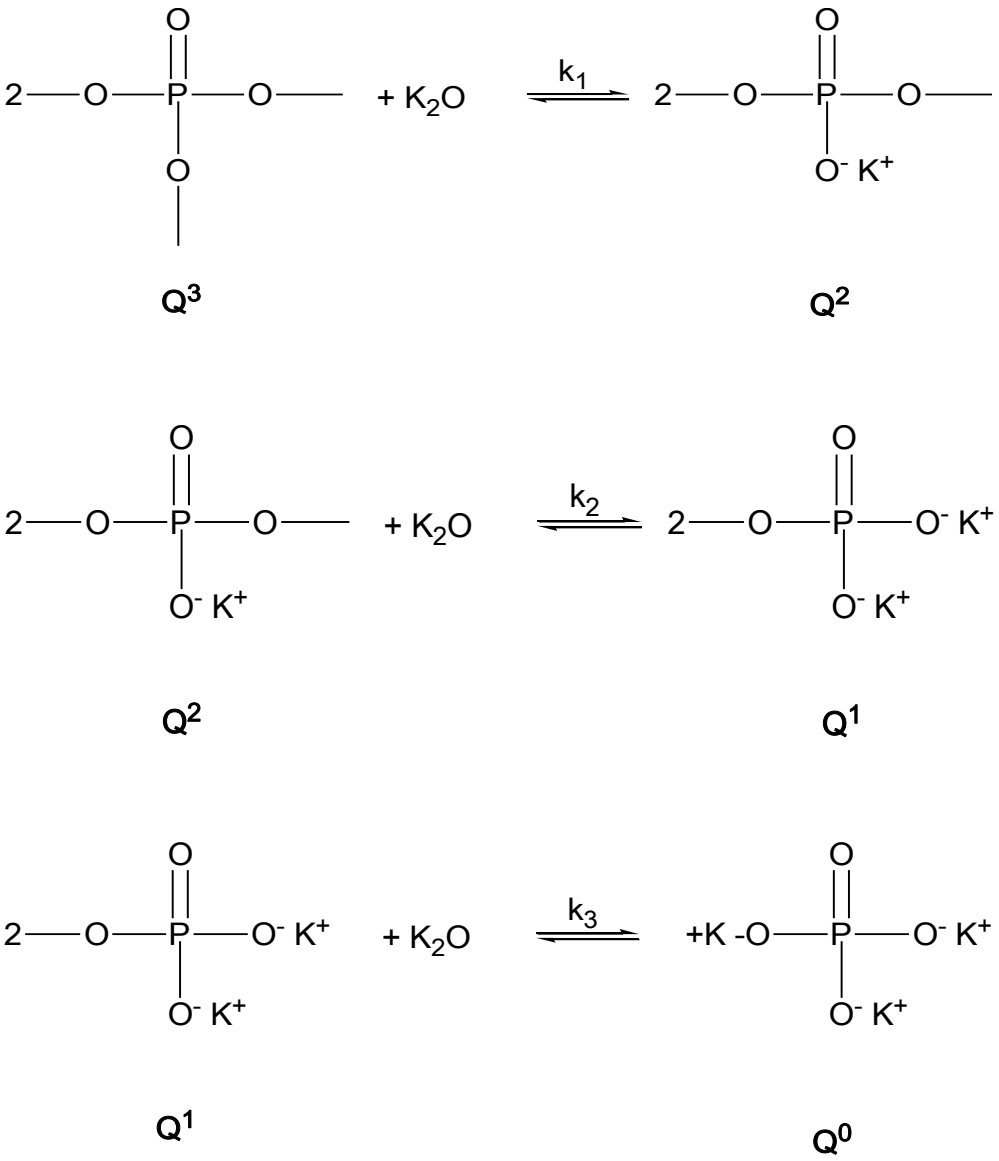

where, k_1, k_2 and k_3 designates the equilibrium constants. The change in phosphate structural units from Q^3 to Q^0 generally provides NBOs, which forms compact structures due to small chain length. Fig. 4.5.6 shows that there are nearly ten bands present in all the glasses. They are mainly composed of the phosphorus–oxygen and hydrogen–oxygen bonds. The band in between 3419-3430 cm^{-1} and 2900-2930 cm^{-1} present in all the glass samples is attributed to the stretching vibrations of P-O-H group and oscillations of hydroxyl groups, respectively **[85, 86].** A certain shift for NK10 and NK20 glasses in these bands at lower region (3430 ⟶ 3419 cm^{-1}) and (2930 ⟶ 2900 cm^{-1}), corresponds to the weakening of OH^- group. On the other hand, in case of NK15 and NK25 glasses, the shift at higher region (3421 ⟶ 3430 cm^{-1}) and (2918⟶ 2930 cm^{-1}) in these bands designates the enhancement of OH^- group.

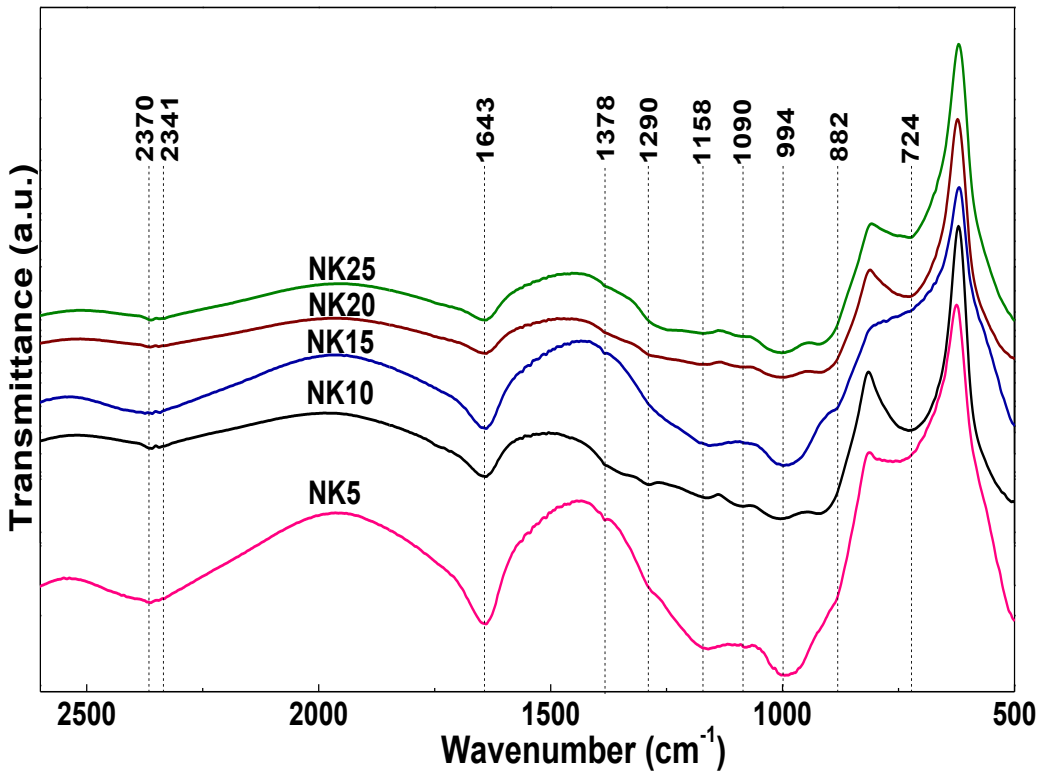

Fig. 4.5.6: FTIR spectra of NK5, NK10, NK15, NK20 and NK25 glasses.

Table 4.5.3: FTIR bands of NK5, NK10, NK15, NK20 and NK25 glass samples.

NK 5	NK 10	NK 15	NK 20	NK 25	Assignments	
2370	2360	2363	2355	2361	δ (H_2O molecules)	[35]
2341	2340	2341	2328	2343	δ (H_2O molecules)	[35]
1643	1642	1644	1637	1642	δ (H_2O molecules)	[36]
1378	1385	1375	----	----	Bridging oxyegen in P=O bond	[80]
1290	----	1287	1285	1271	v_{as} (PO_2 groups) in Q^2 units	[37]
1158	1159	1164	1154	1158	v_s (PO_2 groups) in Q^2 units	[38]
1090	----	1093	1087	1093	Terminal groups; PO_3^{2-} in Q^1 structural units	[39]
994	996	1012	1001	1002	v_s (PO_4^{3-} groups) in Q^0 structural units	[60]
882	883	917	920	919	v_{as} (P-O-P groups) in Q^2 structural units	[62]
724	745	726	733	726	v_s (P-O-P groups) in Q^1 structural units	[38]

Moreover, in all glasses, two small signature and one intense band between 2355-2370 cm^{-1}, 2328-2343 cm^{-1}, and 1637-1644 cm^{-1} are also observed, which is associated to the bending vibration of H_2O molecules **[35, 36].** Interestingly, in NK5, NK10 and NK15 glasses a very small signature in between 1375-1385 cm^{-1} is observed, which is attributed to the stretching vibrations of bridging oxyegen in P=O bond **[80].** However, this band got diminished in NK20 and NK25 glasses. The band in between 1271-1290 cm^{-1} and 1154-1164 cm^{-1} corresponds to the asymmetric and symmetric stretching modes of PO_2 groups in Q^2 phosphate tetrahedra **[37, 38].** In addition to this, two weak bands in between 1087-1093 cm^{-1} and 994-1012 cm^{-1} are also observed. These bands are associated to the formation of the PO_3^{2-} (terminal phosphate groups) in Q^1 structural units and the symmetric stretching modes of PO_4^{3-} in Q^0 structural units, respectively **[39, 60].** It is observed that as K_2O content increases from 5 to 10 mol %**,** the band ~ 1093 cm^{-1} disappears. However, from 15 to 20 mol % this band gets shifted from (1093 cm^{-1} → 1087 cm^{-1}). Apart from this, the bands at around 724-745 cm^{-1} and 882-920 cm^{-1} are attributed to the symmetric and asymmetric stretching vibrations of P-O-P groups in Q^1 and Q^2 structural units, respectively **[38, 62].** It is also observed that NK10 and NK20 glasses exhibited maximum intensity ~ 745 cm^{-1}. This phenomenon further indicates that in NK10 and NK20

glasses the polymerization of phosphate network with higher bond strength is maximum **[60].** The observed assignments from FTIR spectra for all glasses are presented in table 4.5.3.

4.5.5. Raman analysis

The Raman spectra of NK5, NK10, NK15, NK20 and NK25 glasses in the frequency range of (400–1500) cm^{-1} is shown in Fig. 4.5.7. All the spectra are mainly composed of four strong and three weak bands. It is observed that all spectra show broad bands, which indicate the formation of PO_3^{2-} (terminal phosphate groups) **[39].** The first very weak band ~ 507-512 cm^{-1} corresponds to the bending vibration of O-P-O groups and deformation modes of PO_4^{3-} groups **[82]**. It is also observed that in NK10 and NK20 glasses this band almost disappears. The second broad-band ~ 659-668 cm^{-1} corresponds to the symmetric stretching vibrations of bridging oxygens (BOs) in the P-O-P modes **[98].**

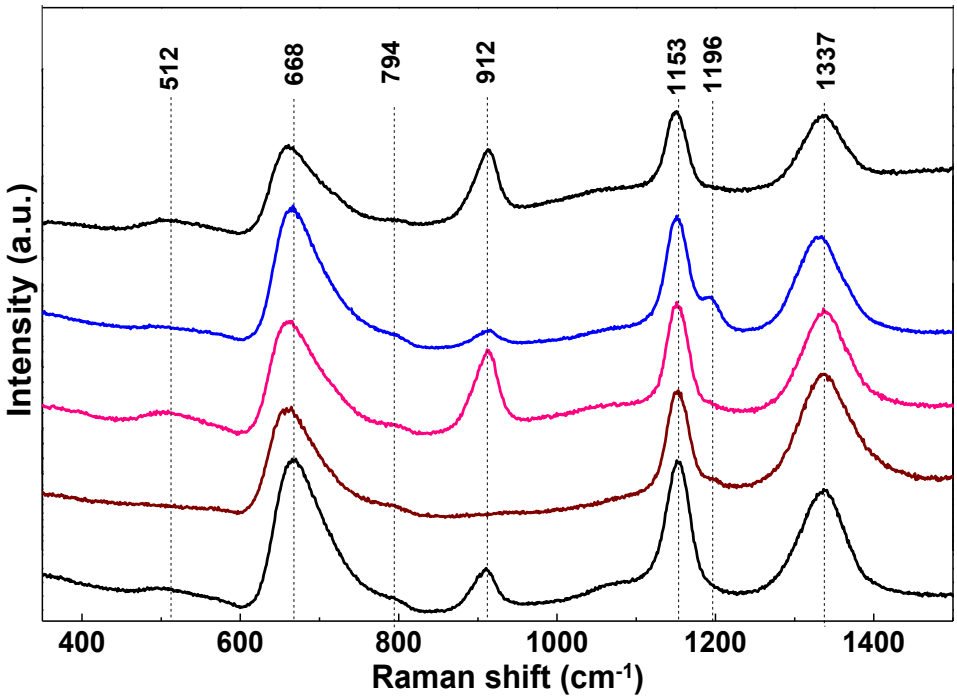

Fig. 4.5.7: Raman spectra of NK5, NK10, NK15, NK20 and NK25 glasses.

The maximum peak intensity with maximum relative area ~ 668 cm^{-1} in glasses NK10 and NK20 confirms that in the phosphate group the polymerization is maximum, which is in well agreement with FTIR results as discussed in previous section. A very weak third signature ~

792-798 cm^{-1} is associated to the asymmetric stretching of bridging oxygens (BOs) in the P-O-P groups **[14].** The fourth strong band 912-914 cm^{-1} is assigned to the asymmetric stretching vibrations of P-O-P groups in Q^2 structural units **[38].** It is observed in NK10 glass, this band almost disappears and in NK20 glass, this band has less intensity than rest of the glasses such as NK5, NK15 and NK25. This phenomenon indicates that NK10 and NK20 glasses are less de-polymerized. Another fifth strong band ~ 1149-1156 cm^{-1} is attributed to symmetric stretching vibrations of the two non-bridging oxygen atoms bonded to phosphorus atoms in PO_2 units (O-P-O) **[104].** With K_2O content, the shift in this band has taken place because of change in bond angle and bond length between P-O-P. The continuous de-polymerization of structural units (Q^4 or Q^3) to structural units (Q^2 or Q^1or Q^0) could also be the reason of change in peak intensity and shift in this band. The sixth weak signature ~ 1196 cm^{-1} and seventh broad-band ~ 1336 cm^{-1} are associated to the symmetric stretching of P=O bonds in Q^2 and symmetric stretching of P=O bond in Q^3 structural units, respectively **[19, 81].** The observed Q^3 structural units indicate the decrease in the average bond length of P-O (NBOs) as well as some polymerization in the phosphate network **[80].** Moreover, NK10 and NK20 glasses show maximum intensity and maximum relative area ~ 1336 cm^{-1} than NK5, NK15 and NK25 glasses.

Table 4.5.4: Raman bands of 5, 10, 15, 20 and 25 mol % K_2O glass samples.

NK 5	NK 10	NK 15	NK 20	NK 25	Assignments	
1337	1335	1336	1333	1337	v_s (P=O bonds) in Q^3 units	[81]
----	1196	---	1195	---	v_s (P=O bonds) in Q^2 units	[19]
1153	1151	1152	1156	1149	v_s (PO_2 groups) in Q^2 units	[86]
912	----	914	913	914	v_{as} (PO_2 groups) in Q^2 units	[38]
794	792	798	797	796	v_{as} (P-O-P modes) of bridging oxygens	[14]
668	659	664	666	661	v_s (P-O-P modes) of bridging oxygens	[83]
512	----	509	---	507	Deformation modes of PO_4^{3-} groups	[82]

This phenomenon indicates NK10 and NK20 glasses exhibits maximum polymerization in phosphate network. This observation is also supported by molar volume and density of the glasses. The observed assignments from Raman spectra for all glasses are given in table 4.5.4.

4.5.6. Kinetics of phase transformations

Under non-isothermal conditions, the dependence of T_g are explained using two models. The first approach is Kissinger's model to estimate the T_g related activation energy (E_g) using equation (4.4). A plot of $\ln(T_g^2/\alpha)$ vs. $1000/T_g$ gives straight line for all compositions which is shown in Fig. 4.5.8 (a). The value of E_g is calculated from the slope of these straight lines and presented in table 4.5.5. A best fit for all the results were done by the least-square method. The standard deviation and arithmetic mean were used to calculate the activation energies. It is observed from table 4.5.5 that NK10 and NK20 glasses exhibits maximum activation energy than other glasses. The second approach is to calculate the Lasoscka parameters by using equation (4.13).

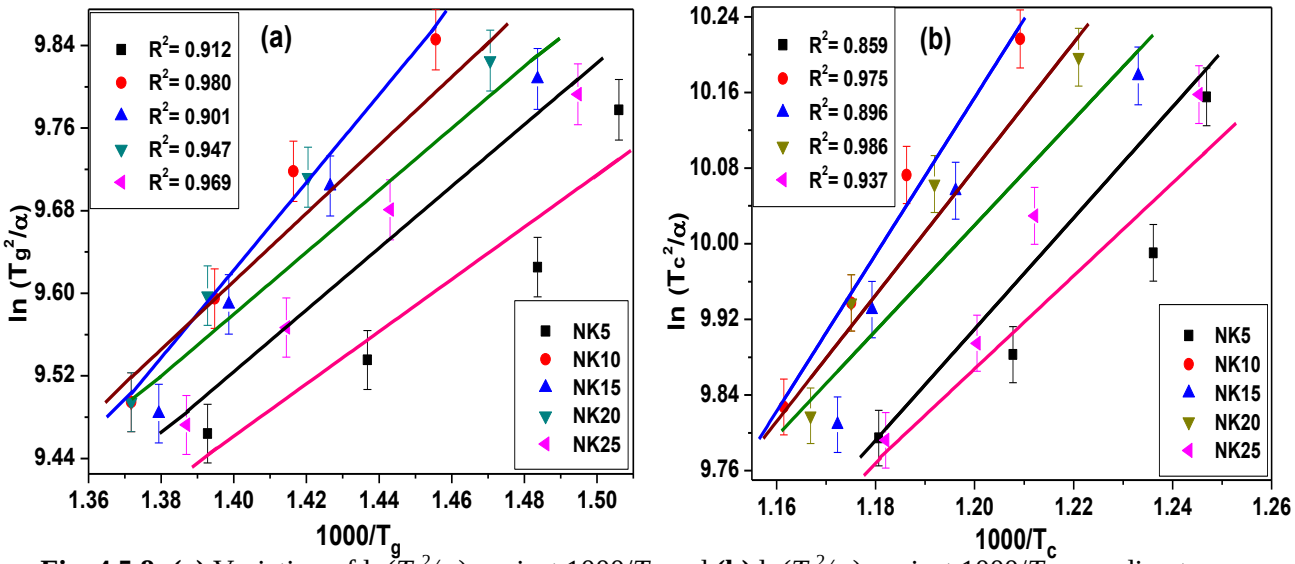

Fig. 4.5.8: (a) Variation of $\ln(T_g^2/\alpha)$ against $1000/T_g$ and **(b)** $\ln(T_c^2/\alpha)$ against $1000/T_c$ according to Kissinger formula for NK5, NK10, NK15, NK20 and NK25 glass samples.

From Fig. 4.5.9 (a), the value of A and B are calculated for all the glasses and presented in table 4.5.5. It is observed from table 4.5.5 that NK10 and NK20 glasses show the minimum value of B than NK5, NK15 and NK25 glasses. The minimum value of B indicates nearby T_g where the configurational changes are minimum. This phenomenon further supports that NK10 and NK20 glasses exhibits high thermal stability, which is already discussed in above sections.

In the present case, the effect of heating rates and effect of modifier content on crystallization are clearly observed. Under non-isothermal condition, the dependence of crystallization temperature (T_c) is explained using two models. To estimate the activation energy of crystallization (E_c), Kissinger's equation (4.4) was used. A plot of $\ln(T_c^2/\alpha)$ against $1000/T_c$ gives straight line for all glasses is shown in Fig. 4.5.8 (b). The activation energy for crystallization (E_c) is evaluated from the slope of these straight lines and listed in table 4.5.5. Furthermore, with the help of equation (4.4), a graph of $\ln(T_f^2/\alpha)$ against $1000/T_f$ is plotted and is shown in Fig. 4.5.10 (a). The value of the activation energy for the inflection-point (E_f) is calculated from the slope of the straight lines and summarized in table 4.5.5. Secondly, Augis-Bennett model is introduced to estimate the activation energy for crystallization and frequency factor (v). These parameters were calculated using equation (4.14).

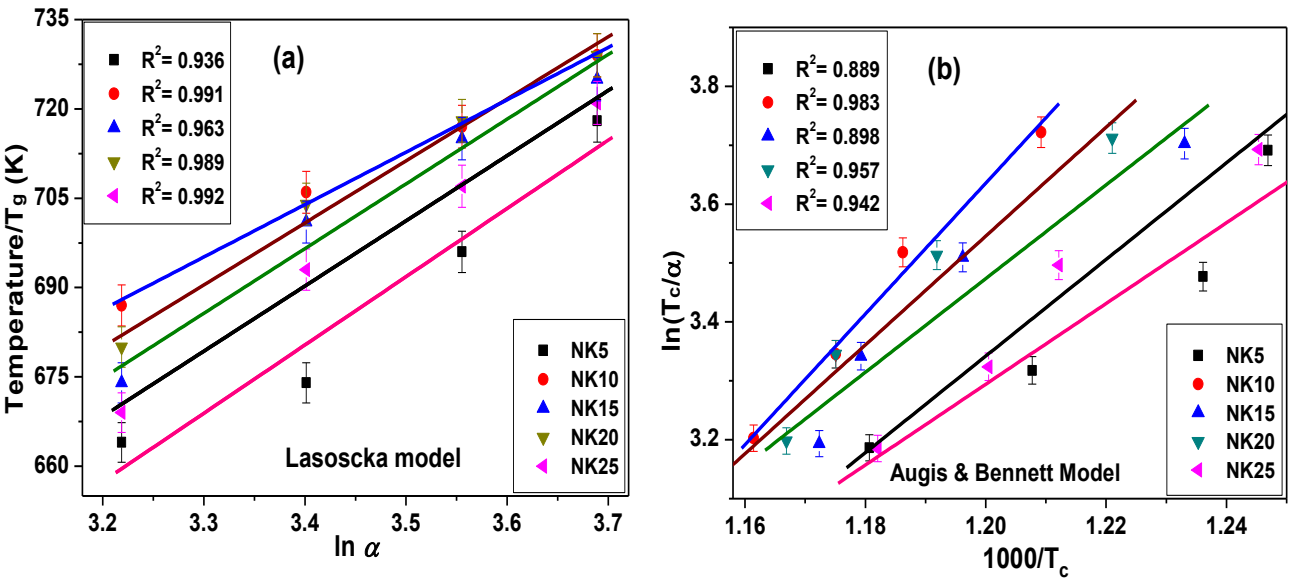

Fig. 4.5.9: (a) Variation of T_g (K) against ln α according to Lasoscka model and **(b)** variation of $\ln(T_c/\alpha)$ against $1000/T_c$ according to Augis-Bennet model for all glass samples.

A plot of $\ln(T_c/\alpha)$ against $1000/T_c$ for all glass compositions is shown in Fig. 4.5.9 (b). After least square fitting, from the intercepts and slope of these straight lines, the values of the v and E_c are calculated and listed in table 4.5.5.

It is observed that the value of *v* for NK10 and NK20 glasses are minimum, which designates that the number of nucleation sites for crystal growth is less in these glasses. The less nucleation sites for NK10 and NK20 glasses further indicate that these are highly stable as compared to other glasses. In addition to this, crystallization rate factors (*K*) are also calculated using equations 4.15, 4.16 and 4.17 at different heating rates and summarized in table 4.5.6.

Table 4.5.5: The activation energies of all the samples using two different models, crystallization frequency and Lasoscka constants.

	Kissinger's Model			Augis and Bennett Model			Lasoscka constants	
Glass Sample ↓	E_g (kJ mol^{-1})	E_f (kJ mol^{-1})	E_c (kJmol^{-1})	E_g (kJ mol^{-1})	E_c (kJ mol^{-1})	Frequency (v) (s^{-1})	A (ºC)	B
NK5	21	36	41	33	58	1.48×10^4	286	116
NK10	35	62	69	50	92	1.65×10^2	405	88
NK15	25	56	46	37	65	6.08×10^2	330	108
NK20	37	60	55	41	74	3.53×10^2	348	103
NK25	24	54	48	38	67	1.58×10^3	319	110

Table 4.5.6: Crystallization rate constants at different heating rates for all glasses.

Sample label	α (^{0}C min^{-1})	K_f (T_g)	K_f (T_f)	K_f (T_c)
NK5	20	1.40×10^4	1.36×10^4	1.35×10^4
	25	1.41×10^4	1.37×10^4	1.36×10^4
	30	1.43×10^4	1.41×10^4	1.41×10^4
	35	1.43×10^4	1.40×10^4	1.39×10^4
NK10	20	1.45×10^2	1.36×10^2	1.34×10^2
	25	1.41×10^2	1.29×10^2	1.27×10^2
	30	1.39×10^2	1.27×10^2	1.24×10^2
	35	1.48×10^2	1.40×10^2	1.37×10^2
NK15	20	5.82×10^2	5.59×10^2	3.30×10^2
	25	5.44×10^2	4.91×10^2	2.98×10^2
	30	5.35×10^2	4.74×10^2	2.90×10^2
	35	5.73×10^2	5.42×10^2	3.22×10^2
NK20	20	3.26×10^2	3.16×10^2	3.19×10^2
	25	3.10×10^2	2.94×10^2	3.00×10^2
	30	3.11×10^2	2.96×10^2	3.01×10^2
	35	3.24×10^2	3.13×10^2	3.16×10^2
NK25	20	1.52×10^3	1.47×10^3	1.54×10^3
	25	1.52×10^3	1.46×10^3	1.40×10^3
	30	1.52×10^3	1.46×10^3	1.42×10^3
	35	1.49×10^3	1.41×10^3	1.33×10^3

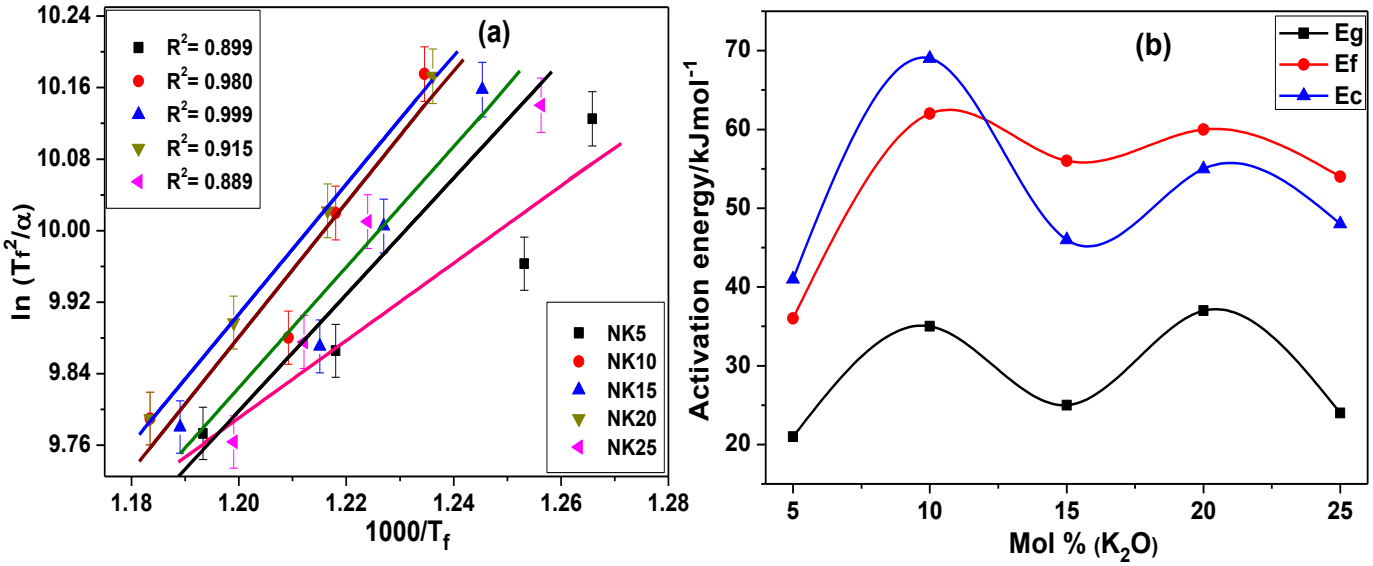

Fig. 4.5.10: (a) Variation of $\ln(T_f^2/\alpha)$ against $1/T_f$ and **(b)** variation of mol % K_2O with activation energies according to Kissinger formula and for NK5, NK10, NK15, NK20 and NK25 glasses.

It is observed from table 4.5.6 that NK10 and NK20 glasses show minimum values of $K_f(T_g)$, $K_f(T_f)$ and $K_f(T_c)$. This phenomenon indicates that these glasses exhibit high thermal stability, which further supports above results obtained from different models. Using Kissinger's and Augis-Bennet models the activation energies for T_g, T_f and T_c are evaluated and listed in table 4.5.5. It is observed from table 4.5.5 that the values of activation energies are in well agreement with each other for both models. However, in between these activation energies the substantial differences take place because of different approximations used for these models. A graph of activation energies against mol % of K_2O is shown in Fig. 4.5.10 (b). The graph shows that as the concentration of K_2O increases from 5 to 10 mol % and from 15 to 20 mol % the activation energies for T_g, T_f and T_c are also increased. The increase in activation energies in NK10 and NK20 glasses can be understood with the help of nature of bonding which is already explained in previous section. However, in case of NK15 and NK25 glasses the activation energy decreases. It is well-known phenomenon that with the addition of modifier content the ionic character increases in glass, which increases the de-polymerization and looses the glass network

structure **[95].** Consequently, glass crystallizes at a lower temperature with the reduction in activation energies.

4.5.7. Electrical conductivity

A graph for NK10 and NK20 glasses in between Z' and Z'' are plotted and is presented in the Fig. 4.5.11 (a) and (b). For these glasses, the value of resistance (R) is obtained from the intercepts of the semicircle on the real axis (Z'). Thereafter, the electrical conductivity is calculated using equation (4.7). From Fig. 4.5.11 (a) and (b), we observe that NK20 has more grain resistance as compared to NK10 glass sample.

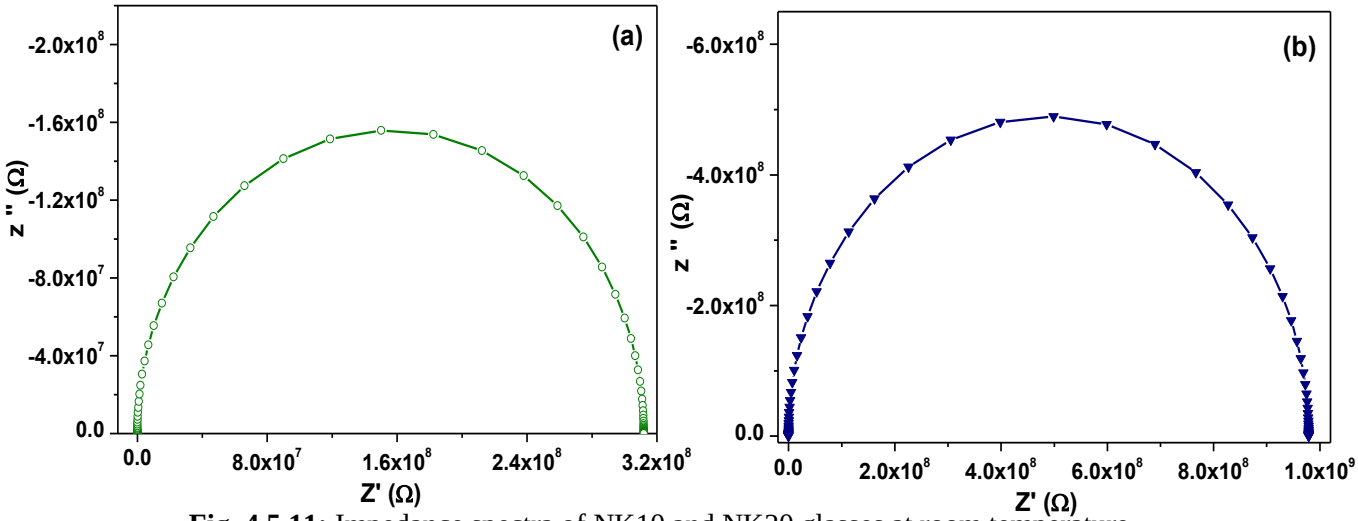

Fig. 4.5.11: Impedance spectra of NK10 and NK20 glasses at room temperature.

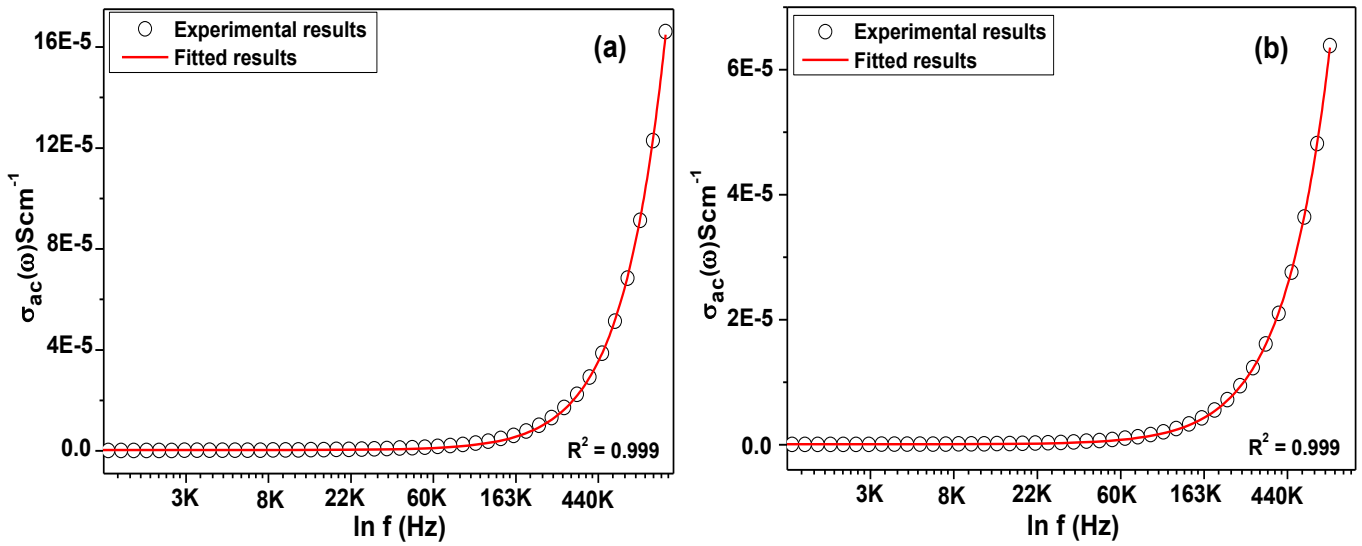

Fig. 4.5.12: Johnscher's plots of NK10 and NK20 glasses at room temperature.

Table 4.5.7: Grain resistance, dc and ac conductivity at room temperature and other fitting parameters for NK10 and NK20 glasses.

Sample	R_g (Ω) $\times 10^6$	σ_{ac} $\times 10^{-5}$(Scm^{-1})	σ_{dc} $\times 10^{-7}$(Scm^{-1})	B $\times 10^{-16}$	s	R^2	ω_h $\times 10^3$ (Hz)
NK10	3.2	16.6	3.11	7.34	1.96	0.999	6.47
NK20	9.9	2.19	0.86	19.4	1.89	0.999	17.51

The ac conductivities are calculated for both glasses and presented in table 4.5.7. The NK10 glass sample exhibit higher conductivity than NK20. No doubt with the K_2O content, ionic conductivity should increase because as K_2O content increases, it increases the number of non-bridging oxygen in the glass. The non-bridging oxygen generally creates disorderness and increases the ionic conductivity. However, in the present case, as K_2O content increases on the expense of Na_2O from 10 to 20 mol %, it increases the K^+ ions on the expense of Na^+ ions. As we know Na^+ has ionic radii (1.02 Å) and K^+ has ionic radii (1.38 Å) so, overall electrical conductivity decreases from 10 to 20 mol % K_2O because larger size and higher mass restrict the fast movement. In the present glasses, to separate out ac and dc conductivity Johnscher's power law equation (4.8) was used. Equation (4.8) was used to fit the room temperature ac conductivity data and calculated the dc conductivity. While fitting, the values of B and s were varied at the same time to get best fits. The fitted graphs for NK10 and NK20 glasses are shown in the Fig. 4.5.12 (a) and (b). After fitting, dc conductivity, parameter B and the value of exponent s were calculated and are presented in the table 4.5.7. It is observed from table 4.5.7 that NK10 glass exhibits high ionic conductivity than NK20 glass. In addition to this, the value of exponent *s* (1.96) in NK10 glass approaches to the standard value of *s* (2), which designates that NK10 glass are more ionic conductor than NK20 glass. Furthermore, for both glasses, the hopping frequency (ω_h) to crossover dc to ac conductivity is also calculated using equation (4.9). The as obtained values of σ_{dc}, B, and s were taken from table 4.5.7 and with the help of equation (4.9), the hoping frequencies (ω_h) for both glasses were calculated and are presented in the table 4.5.7. It is observed from table 4.5.7 that NK10 glass can easily crossover from dc to

ac at lower frequency. On the other hand, NK20 glass requires high frequency to crossover from dc to ac conductivity. In all the glasses, the maximum electrical conductivity is observed ~ 10^{-4} Scm^{-1} at room temperature in CuS containing glasses. It is well-known phenomenon that the conductivity in the glasses is dominated by the ionic conductivity. However, CuS is known to the electronic conductivity. Unfortunately, the present samples are hygroscopic in nature, so during the conductivity measurement it is difficult to do the conductivity with temperature. The conductivity follows the following trend

$$Li^+ > Na^+ > K^+$$

As the ionic radii decreases with lower charge hopping ions plays very important to increase the overall conductivity.

REFERENCES:

[1] S.S. Berbano, I. Seo, C.M. Bischoff, K.E. Schuller, S.W. Martin, J. Non-Cryst. Solids, **358,** (2012) 93.

[2] K. Minami, A. Hayashi, M. Tatsumisago, Solid State Ionics, **189,** (2008) 1282.

[3] S. Villain, E. Nigrelli, G. Nihoul, Solid State Ionics, **116,** (1999) 73.

[4] V. Raghvan, Materials Science and Engineering. 5th Edition; 2008.

[5] A. Hayashi, K. Noi, A. Sakuda, M. Tatsumisago, Nature Commun., **3,** (2012) 856.

[6] S. Song, Z. Wen, Y. Liu, J. Lin, X. Xu, Q. Zhang, J. Solid State Electrochem., **14,** (2010) 1735.

[7] Sci Glass: Database and Information System, Version 7.0, premium ed., Holland, Michigan: ITC, 2008; http://www.sciglass.info.

[8] Y.K. Startsev, A.A. Pronkin, I.A. Sokolov, I.V. Murin, Glass Phy. Chem., **37,** (2011) 263.

[9] J. Stelling, H. Be*Hr*ens, M. Wilke, J. Gottlicher, E.C. Aljanabi, Geochimica et Cosmochimica Acta, **75,** (2011) 3542.

[10] F.L. Galeener, J.C. Mikkelsen, Solid State Commun., **30,** (1979) 505.

[11] P. Znacik, M. Jamnicky, J. Non-Cryst. Solids, **64,** (1984) 291.

[12] Y.M. Moustafa, K.E. Egili , J. Non-Cryst. Solids, **240,** (2003) 144.

[13] S.L. Neverov, Influence of Transformation in Melts on the Anionic Structure of Glassy Alkali Metal Phosphates, Candidate's Dissertation, Sverdlovsk, 1994.

[14] J.J. Hudgens, R.K. Brow, D.R. Tallant, S.W. Martin, J. Non-Cryst. Solids, **223,** (1998) 21.

[15] J.F. Leroy, G. Kaufmann, A. Müller, H.W. Roesky. C.r. Acad. Sc. Paris, **267,** (1968) 563.

[16] M. Tachez, J.P. Malugani, R. Mercier, G. Robert, Solid State Ionics, **170,** (2004) 173.

[17] R. Mercier, J.P. Malugani, B. Fahys, G. Douglade, J. Robert, J. Solid State Chem., **43,** (1982) 151.

[18] T. Ohtomo, F. Mizuno, A. Hayashi, K. Tadanaga, M. Tatsumisago, Solid State Ionics, **176,** (2005) 2349.

[19] Y.M. Moustafa, K. El-Egili, J. Non-Cryst. Solids, **240,** (1998) 144.

[20] R. Mangio, V. Langer, L.G Johansson, Acta Chemica Scandinavica, **45,** (1991) 572.

[21] D. Larink, H. Eckert, S. W. Martin, J. Phys. Chem. C, **116,** (2012) 22698.

[22] M. Tatsumisago, M. Nagao, A. Hayashi, J. Asian Ceram. Soc., **1,** (2013) 17.

[23] G. Kaur, V. Kumar, O.P. Pandey, K. Singh, J. Electrochem. Soc., **159,** (2012) B277.

[24] B. Kaur, K. Singh, O.P. Pandey, Int. J. Hydrogen Energy, **37,** (2012) 3839.

[25] A. Arora, K. Singh, O.P. Pandey, Int. J. Hydrogen Energy, **36,** (2011) 14948.

[26] A.T. Patel, A. Pratap, J. Therm. Anal. Cal., **110,** (2012) 567.

[27] H.E. Kissinger, J. Res. National Bur. Stand., **57,** (1956) 217.

[28] S. Mahadevan, A. Giridhar, A.K. Singh, J. Non-Cryst. Solids, **88,** (1986) 11.

[29] A. Hruby, Czech. J. Phys.B, **22,** (1972) 1187.

[30] A.K. Jonscher, Nature, **267,** (1977) 673.

[31] A.K. Jonscher, J. Phys. D: Appl. Phys., **32,** (1999) R57.

[32] Q. Xu, B. Huang, Y. Zhao, Y. Yan, R. Noufi, S.H. Wei, Appl. Phys. Lett., **100,** (2012) 061906.

[33] L. Isac, A. Duta, A. Kriza, S. Manolache, M. Nanu, Thin Solid Films, **515,** (2007) 5755.

[34] M. Saad, M. Poulain, Mater Sci Forum, **11, (**1987) 19.

[35] F.H. Elbatal, J. Mat. Sci., **43,** (2008) 1070.

[36] F.H. Elbatal, M.A. Marzouk, A.M. Adbelghany, J. Non-Cryst. Solids, **357,** (2011) 1027.

[37] Y. Tsunawaki, N. Iwamoto, T. Hattori, A. Mitsuishi, J. Non-Cryst. Solids, **44,** (1981) 369.

[38] G.V. Rao, H.D. Shashikala, J. Adv. Ceram., **3,** (2014) 109.

[39] O. Cozar, M. Bako, L. Daraban, I. Ardelean, L. David, Opt. Electron Adv. Mat., **2,** (2008) 249.

[40] J. Koo, B.S. Bae, , H.K. Na, J. Non-Cryst. Solids, **212,** (1997) 173.

[41] L. Koudelka, M. Pisarcik, Solid State Commun., **41,** (1982) 115.

[42] M. Tache, J.P. Malugani, R. Mercier, G. Robert, Solid State Ionics, **14,** (1984) 181.

[43] G. Singla, K. Singh, O.P. Pandey, Appl. Phys. A, **113,** (2013) 237.

[44] N. Forler, F. Vasconcelos, S. Cristol, J.F. Paul, L. Montagne, T. Charpentier, F. Mauric, L. Delevoye, Phys. Chem. Chem. Phys., **12,** (2010) 9053.

[45] N. Lahl, K. Singh, L. Singheiser, K. Hilpert, J. Mat. Sci., **35,** (2000) 3089.

[46] R. Kaur, S. Singh, O.P. Pandey, J. Mol. Struct., **1049,** (2013) 409.

[47] B.V.R. Chowdari, K.I. Tan, W.T. Chia, R. Gopalakrishnam, J. Non-Cryst. Solids, **119,** (1990) 95.

[48] B. Bridge, N.D. Patel, J. Non-Cryst. Solids, **91,** (1987) 27.

[49] A. Chahine, M. Et-tabirou, J.L. Pascal, Mater. Lett., **58,** (2004) 2776.

[50] L.G Saout, P. Simon, F. Fayon, A. Blin, Y. Vaills, J. Raman Spec., **33,** (2002) 740.

[51] A. Shaim, M. Et-tabirou, Mat. Chem. Phys., **80,** (2003) 63.

[52] B. Tiwari, A. Dixit, G.P. Kothiyal, M. Pandey, S.K. Deb, BARC Newsletter, **285,** (2007) 167.

[53] L. Pavic, A.M. Milankovic, P.R. Rao, A. Santic, V.R. Kumar, N. Veeraiah J. Alloys Comp., **604,** (2014) 352.

[54] Y.M. Lai, X.F. Liang, S.Y. Yang, J.X. Wang, B.T. Zhang, J. Mol. Struct., **1013,** (2012) 134.

[55] J. Yifen, J. Dehua, C. Xiangsheng, B. Behya, H Xihuai, J. Non-Cryst. Solids, **80,** (1986) 147.

[56] A.A. Kader, A.A. Higazy, M.M. Elkholy, J. Mater. Sci.: Matter. Electron., **2,** (1991) 157.

[57] R.L. Sammons, A.C. Thackray, H.M. Ledo, P.M. Marquis, I.P. Jones, P. Yong and L.E. Macaskie, J. Phys.: Conference Series, **93,** (2007) 012048.

[58] E.I. Kamitsos, J.A. Kapoutsis, G.D. C*Hr*yssikos, J.M. Hutchinson, A.J. Pappin, M.D. Ingram, J.A. Duffy, Phys. Chem. Glasses, **36,** (1995) 141.

[59] J.V. Granadosa, F.G. Correaa, C.E.B. Díaz, Appl. Surface Sci., **279,** (2013) 97.

[60] R.L. Frost, Y. Xi, R. Scholz, F.M. Belotti, M.C. Filho, Spectr. Lett. **46,** (2013) 415.

[61] R.L. Frost, Y. Xi, A. Lopez, V.A. Moreira, R. Scholz, R.M.F. Lima, A.L. Gandini, Spectr. Lett., **47,** (2014) 214.

[62] Y.M. Lai, X.F. Liang, S.Y. Yang, J.X. Wang, L.H. Cao, B. Dai, J. Mol. Struct., **992,** (2011) 84.

[63] N. Vedeanu, O. Cozar, I. Ardelean, B. Lendl, J. Optoelectr. Adv. Mat., **8,** (2006) 78.

[64] K. Nakamoto, Infrared and Raman Spectra of Inorganic and Coordination Compounds: Part A: Theory and Applications in Inorganic Chemistry, Sixth ed., John Wiley & Sons, 2008.

[65] A. Sakuda, A. Hayashi, M. Tatsumisago, Sci. Repo., **3,** (2013) 2261.

[66] M.K. Halimah, W.M. Daud, H.A.A. Sidek, Chal. Lett., **7,** (2010) 613.

[67] R. Kaur, S. Singh, O.P. Pandey, Solid State Commun., **188,** (2014) 40.

[68] K.B. Modi, S.J. Shah, N.B. Pujara, T.K. Pathak, N.H. Vasoya, I.G. Jhala, J. Mol. Struct., **1049,** (2013) 250.

[69] Manupriya, K.S. Thind, G. Sharma, V. Rajendran, K. Singh , A.V.G. Devi, S. Aravindan, Phys. Stat. Sol. A, **203,** (2006) 2356.

[70] D.P. Mukherjee, S.K. Das, Ceram. Int., **40,** (2014) 4127.

[71] L.C. Huanga, C.C. Lin, P. Shen, Mater. Sci. Eng. A, **452/453,** (2007) 326.

[72] X. Li, X. Yin, L. Zhang, L. Cheng, Y. Qi, Mater. Sci. Eng. A, **500,** (2009) 63.

[73] M. Ghaffari, P. Alizadeh, M.R. Rahimipour, J. Non-Cryst. Solids, **358,** (2012) 3304.

[74] L. Bih, L. Abbas, S. Mohdachi, A. Nadiri, J. Mol. Struct., **891,** (2008) 173.

[75] P.M.V. Teja, C. Rajyasree, P.S. Rao, A.R. Babu, C. Tirupataiah, D.K. Rao, J. Mol. Struc., **1014,** (2012) 119.

[76] S. Rani, S. Sanghi, A. Agarwal, V.P. Seth, Spectrochim. Acta Part A, **74,** (2009) 673.

[77] L.V. Wullen, H. Eckert, G. Schwering, Chem. Mater., **12,** (2000) 1840.

[78] H.J.D. Jager, L.C. Prinsloo, Thermochim. Acta, **376,** (2001) 187.

[79] F.H. ElBatal, M.A. Ouis, R.M.M. Morsi, S.Y. Marzouk, J. Non-Cryst. Solids, **356,** (2010) 46.

[80] R. Hussin, M.A. Salim, N.S. Alias, M.S. Abdullah, S. Abdullah, S.A.A. Fuzi, S. Hamdan, M.N.M. Yusu, J. Fundamental Sci., **5,** (2009) 41.

[81] M. Karabulut, E. Metwalli, D.E. Day, R.K. Brow, J. Non-Cryst. Solids, **328,** (2003) 199.

[82] A.M. Abdelghany, F.H. Elbatal, H.A. Elbatal, F.M. Ezzeldin, J. Mol. Struct., **1074,** (2014) 503.

[83] R. Christensen, G. Olson, S.W. Martin, J. Phys. Chem. B, **117,** (2013) 2169.

[84] L. Koudelka, P. Mosner, M. Zeyer, C. Jager, J. Non-Cryst. Solids, **351,** (2005) 1039.

[85] I. Avramov, C. Russel, N. Kolkovska, I. Georgiev, J. Phys.: Condens. Matter, **20,** (2008) 335203.

[86] A. Kaswan, V. Kumari, D. Patidar, N.S. Saxena, K. Sharma, Proc. Appl. Ceram., **8,** (2014) 25.

[87] M. Lasocka, J. Therm. Anal., **16,** (1979) 197.

[88] A.M. Hu, K.M. Liang, M. Li, D.L. Mao, Mat. Chem. Phys., **98,** (2006) 430.

[89] V.C.S. Reynoso, K. Yukimitu, T. Nagami, C.L. Carvalho, J.C.S. Moraes, E.B. Araujo, J. Phys. Chem. Solids, **64,** (2003) 27.

[90] A.K. Yadav, C.R. Gautam, P. Singh, RSC Adv., **5,** (2015) 2819.

[91] J.A. Augis, J.E. Bennett, J. Therm. Anal., **13,** (1978) 283.

[92] Deepika, K.S. Rathore, N.S. Saxena, J. Phys.: Condens. Matter, **21,** (2009) 335102.

[93] K. Cheng, J. Phys. Chem., **103,** (1999) 8272.

[94] K. Matusita, T. Komatsu, R. Yokota, J. Mat. Sci., **19,** (1984) 291.

[95] E. Wers, H. Oudadesse, B. Lefeuvre, B. Bureau, O.M. Conanec, Thermochim. Acta, **580,** (2014) 79.

[96] T.D. Melnichenko, V.M. Rizak, T.N. Melnichenko, V.I. Fedelesh, Glass Phys. Chem., **30,** (2004) 406.

[97] Y.I. Frenkel, Kinetic Theory of Liquids (Nauka, Leningrad, 1975; Clarendon, Oxford University, Press, 1946).

[98] F. Wang, Q. Liao, G. Xiang, S Pan, J. Mol. Struct., **1060,** (2014) 176.

[99] R.C. Lucacel, A.O. Hulpus, V. Simon, I. Ardelean, J. Non-Cryst. Solids, **355,** (2009) 425.

[100] R. Yang, Y. Wang, X. Hao, J. Zhan, S. Liu, J. Non-Cryst. Solids, **357,** (2011) 2192.

[101] K.V. Shah, M. Goswami, D.K. Aswal, V.K. S*Hr*ikhande, S.K. Gupta, G.P. Kothiyal, J. Therm. Anal. Calorim., **89,** (2007) 153.

[102] A. Arora, A. Goel, E.R. Shaaban, K. Singh, O.P. Pandey, J.M.F. Ferreira, Physica B Condensed Matter, **403,** (2008) 1738.

[103] J.B. Bouche, Investigation of glass-ceramic materials for the sealing in Solid Oxide Fuel Cells, Dissertation, Montereau-Fault-Yonne, (2009).

[104] L. Bala, D. Muresan, M. Baia, J. Popp, S. Simon, Vib. Spetcrosc., **43,** (2007) 313.

Chapter-5

(Conclusions and future scope)

5.1. CONCLUSIONS

Oxysulfide samples are phase separated glasses. Higher Na_2S (60 mol%) prevent the glass formation in the Na_2S-P_2S_5 system. The glass sample N3 ad N5 generated the least amount of H_2S gas than others. Raman spectroscopy also demonstrated that N3 and N5 glass samples exhibited less structural changes with respect to air. Dilatometric study for N1, N2, N4 and N6 samples revealed two-phase transitions that occurred because of water loss and glass transition, respectively. However, in case of N3 and N5 glass samples water loss signature is not observed in DTA study. The above phenomenon indicated that samples N3 and N5 are more stable than others and less prone to environmental moisture. DTA analysis showed that T_g and T_c increased with increasing heating rate. N3 glass sample required high activation energy as compared N5 glass for devitrification. N5 glass samples showed the electrical conductivity one order more than that of N3 glass sample at room temperature. Overall, N5 glass sample showed good thermal stability with better conductivity than other glasses. $45P_2S_5$-$55Na_2S$ was selected for further study due to good thermal and electrical properties.

In CuS series, XRD patterns showed two broad halos with maxima ~ 17º and 31º including one crystalline peak ~ 32.13º for NC5 and NC10 samples The presence of two halos indicated phase separated amorphous nature of both samples. As compared to base glass ($45P_2S_5$-$55Na_2S$), the addition of CuS increases the phase separation tendency. The presence of crystalline peak was indexed with $Cu_{1.8}S$ (ICDD No. 01-085-1693) having rhombohedral crystal structure. The crystalline phase $Cu_{1.8}S$ is a stable p-type compound, which is generally used in solar cells as absorber materials. Thermal analysis depicted that as CuS increases from 5 to 10 mol% in the Na_2S-P_2S_5 system; it increases the chemical durability and overall electrical conductivity. FTIR and Raman analysis confirmed that NC10 glass samples exhibited high stability than NC5 glass sample.

Previously, in the $45P_2S_5$-$55Na_2S$ glass composition, the electrical conductivity was observed ~ 9.45×10^{-7} Scm^{-1} at room temperature. The addition of CuS content in the $45P_2S_5$-$55Na_2S$ glass composition increases the overall conductivity of three orders higher than the base glass.

For Na_2O-P_2O_5 glass-ceramics, the X-ray diffraction pattern exhibited two crystalline phases, i.e., $NaPO_3$ and $Na_2H_2P_2O_7$. The density of glass-ceramics and volume fraction of $NaPO_3$ increases with increasing Na_2O content. FTIR and Raman study demonstrated that the de-polymerization of phosphate group changes from $Q^2 \rightarrow Q^1 \rightarrow Q^0$ with increasing content of Na_2O. The Young's moduli increases from 17.3 GPa to 21.5 GPa as Na_2O content increases from 40 to 55 mol%. The maximum hardness observed is 918 MPa for NP4 glass-ceramic sample. The SEM study revealed that interlocked crystals are dispersed in a glassy matrix. Such morphology provides toughened character to the glass-ceramic composite, which is helpful for its application in Na-ion batteries. The Poisson's ratio clearly indicates that present glass-ceramic samples are less cross-linked than SiO_2 and B_2O_3 based glasses.

In Li_2O series, all synthesized glasses are amorphous as confirmed by X-ray diffraction. The replacement of Na_2O by Li_2O decreases the glass transition temperature (T_g) except for NL15 glass. This glass exhibits highest thermal stability, where both the modifiers are present in the ratio of (1:2); (Li_2O:Na_2O). The FTIR and Raman studies show the highest polymerization for NL15 glass as compared to other glasses. The maximum value of the fluctuation-free volume is observed for NL5 glass. It indicates NL5 glass can easily crystallize due to lower glass network connectivity. The overall electrical conductivity for NL15 glass obtained is ~ 17.4×10^{-5} Scm^{-1} at room temperature.

In K_2O series, all glasses are amorphous in nature as confirmed by XRD patterns. Generally, two modifiers gives signature of phase separation in XRD pattern. However, no phase separation is observed in these glasses. The replacement of Na_2O by K_2O decreases the glass

transition temperature except for NK10 and NK20 glasses. NK10 and NK20 glasses show highest thermal and kinetic stability than other glasses. The FTIR and Raman analysis indicated the highest polymerization for NK10 and NK20 glasses as compared to other glasses. The maximum activation energies for (E_g) and (E_c) in NK10 and NK20 glasses indicated their higher rigidity and higher network connectivity. The overall electrical conductivity of the NK10 and NK20 glasses at room temperature observed are ~ 16.6×10^{-5} Scm^{-1} and 2.19×10^{-5} Scm^{-1}, respectively. These glasses showed slightly less electrical conductivity than NL15 glass. NK10 and NK20 and NL15, glasses can be used as a solid electrolyte for battery application.

5.2. FUTURE SCOPE

The ac conductivity of all glass and glass-ceramics with respect to temperature can be measured in oxidizing and reducing atmosphere to know the pre-dominancy of the conduction mechanism. Additionally, the as prepared samples must be checked for their durability. The e.m.f measurement will be done to know the contribution of electronic and ionic conductivity. The elastic moduli of all glasses can be measured to know about their applicability as solid electrolyte for batteries applications.